INVESTIGATIONS IN
ELECTROMAGNETIC SCATTERING CENTER THEORY

R. A. Ross

A thesis

presented for

The Degree of Doctor of Philosophy

in Electrical Engineering,

in the University of Manitoba,

Winnipeg, Manitoba, Canada

Electrical Engineering Department

University of Manitoba

Winnipeg, Manitoba, Canada

1971

INVESTIGATIONS IN ELECTROMAGNETIC SCATTERING CENTER THEORY

R.A. Ross

ABSTRACT

For practical radar targets the use of approximate scattering the(/ is inevitable. Simplification of high-frequency scattering phe mena in terms of the scattering center concept is advocated in this th is. The major disadvantage of this approach is the limited number of ,cattering centers having known reradiation characteristics. Corner, t and modified edges are three important scattering centers requiring f :ther investigation. This thesis is concerned with the scattering nter formed by a rounded edge.

The field scattered from a perfectly conducting wedge with :ounded edge is calculated by the boundary value approach. These results enable the effects of rounding to be examined as functions of incidence and observation angles, polarization, and wedge angle. The quantitative data are used to evaluate an asymptotic form of physical optics theory which is suited to estimation of scattering center returns. By obtaining empirical relations which accurately fit the boundary value data, scattering center theory is extended to include targets with one or more moderately rounded edges. Specific applications include the modified equilateral triangular prism, the modified square prism, and the modified finite, right-circular cylinder.

The boundary value approach is also specialized to calculate scattering by a cylindrically tipped wedge and a truncated wedge. These results are used to evaluate geometrical diffraction theory when the scattering phenomenon involves creeping waves and strong interaction between scattering centers, respectively.

ABSTRACT

For practical radar targets the use of approximate scattering theory is inevitable. Simplification of high-frequency scattering phenomena in terms of the scattering center concept is advocated in this thesis. The major disadvantage of this approach is the limited number of scattering centers having known reradiation characteristics. Corner, tip and modified edges are three important scattering centers requiring further investigation. This thesis is concerned with the scattering center formed by a rounded edge.

The field scattered from a perfectly conducting wedge with rounded edge is calculated by the boundary value approach. These results enable the effects of rounding to be examined as functions of incidence and observation angles, polarization, and wedge angle. The quantitative data are used to evaluate an asymptotic form of physical optics theory which is suited to estimation of scattering center returns. By obtaining empirical relations which accurately fit the boundary value data, scattering center theory is extended to include targets with one or more moderately rounded edges. Specific applications include the modified equilateral triangular prism, the modified square prism, and the modified finite, right-circular cylinder.

The boundary value approach is also specialized to calculate scattering by a cylindrically tipped wedge and a truncated wedge. These results are used to evaluate geometrical diffraction theory when the scattering phenomenon involves creeping waves and strong interaction between scattering centers, respectively.

ACKNOWLEDGMENTS

During this investigation, the author became indebted to many people for assistance in numerous ways. Among these it is a pleasure to use this means to thank:

Professor M.A.K. Hamid for initial encouragement and continuing technical guidance in all phases of this investigation.

Professor W. Boerner, Professor L. Shafai and A. Mohsen for technical advice and other assistance.

The Cornell Aeronautical Laboratory, CAL personnel, and in particular, Mr. R.E. Kell, Mr. M.E. Bechtel and Mr. G. Sargis for cooperation in many ways.

My wife Eileen for her help and my two sons, Bill and Alex, for their forbearance.

Financial support has been provided by a Sabbatical Leave granted by the Education Committee of Cornell Aeronautical Laboratory and by Graduate Fellowships awarded by the Faculty of Graduate Studies in the University of Manitoba.

TABLE OF CONTENTS

LIST OF PRINCIPAL SYMBOLS

σ	radar cross section of target
ρ	scattering phase of target
σ_i	radar cross section of i^{th} scattering center
ρ_i	scattering phase of i^{th} scattering center
k	wave number (equal to $2\pi/\lambda$, where λ is the wavelength)
a	radius of curvature of rounded edge
α	half-angle of semi-infinite wedge
(r, ϕ, z)	polar coordinate system with origin at virtual apex of wedge
(ρ, θ, z)	polar coordinate system with origin at axis of cylindrical sector
d	separation between origins of two polar coordinate systems
R	radius of circular-cylindrical matching boundary
$r_o, \phi_o; \rho_o, \theta_o$	location of line source excitation
E_z, H_r, H_ϕ	total nonvanishing electric and magnetic field components for TM or vertical-polarization case
H_z, E_r, E_ϕ	total nonvanishing magnetic and electric field components for TE or horizontal-polarization case
Ψ	exterior wedge angle equal to $2\pi - 2\alpha$
γ	exterior wedge angle normalized by π.
$I_o(k_o)$	intensity of electric (magnetic) line source
$J_z(M_z)$	electric (magnetic) current density
ω	angular frequency
ϵ	permittivity of free space
μ	permeability of free space
$J_\nu(k\rho)$	Bessel function of the first kind of argument $k\rho$ and order ν
$H_\nu(k\rho)$	Hankel function of the second kind of argument $k\rho$ and order ν

LIST OF PRINCIPAL SYMBOLS (Cont'd)

$Z_\nu(k\rho)$	Any cylindrical Bessel function of argument $k\rho$ and order ν
$\delta(x)$	Dirac delta function (unit impulse)
ϵ_n	Neumann number
j	$j^2 = -1$
E_z^i (H_z^i)	incident electric (magnetic) field
E_z^s (H_z^s)	scattered electric (magnetic) field
z	coordinate along the line of sight
$g(k)$	physical optics transfer function of target
$g_i(k)$	asymptotic physical optics transfer function of i^{th} scattering center
F_v (F_H)	vertical (horizontal) polarization amplitude of range-independent scattering pattern
F^p, ρ^p	amplitude, phase of range-independent perturbation field
ϕ_o (ϕ)	incidence (observation) angle referenced to plane of symmetry of wedge
φ_o (φ)	incidence (observation) angle referenced to face of wedge (i.e., $\varphi = \phi - \alpha$)
θ	aspect angle referenced to symmetry axis of target

1. INTRODUCTION

This chapter provides background for the body of research performed in the thesis. Section 1.1 contains a brief survey of scattering techniques which indicates the need for high-frequency asymptotic solutions; indeed, for practical radar targets the use of approximate theory is inevitable. Simplification of high-frequency scattering phenomena in terms of the scattering center concept is advocated in Section 1.2. The major disadvantage is the limited number of scattering centers having known reradiation characteristics and three important scattering centers requiring further study are discussed in Section 1.3. This thesis is concerned with the scattering center formed by a rounded edge. Section 1.4 treats methods for calculating the scattering by a rounded edge and a boundary value approach is chosen for edges with moderate rounding.

In Chapter 2, scattering by a semi-infinite, perfectly conducting wedge with rounded edge is formulated for line source excitation using the boundary value approach. Numerical results are presented for the important case of monostatic plane-wave scattering in the far field. These results comprise principal-polarization data plotted as a function of aspect angle for 60°, 90°, and 120° wedges with maximum rounding $ka = 4$, where ka is the electrical radius of curvature of the edge. It is shown that ka as small as 0.8 can double the sharp wedge result in certain cases, although the effect of rounding is markedly dependent upon polarization and wedge angle. Calculations of bistatic scattering lead to investigation of shadow-region fields as a function of rounding. Related studies involving the cylindrically tipped wedge

are included in this chapter since they influence the numerical capability of the boundary value solution for the wedge with rounded edge.

Chapter 3 introduces an asymptotic form of physical optics which is suited to the analysis of scattering centers on an edge with large rounding. Comparison of results of approximate theory with boundary value data shows that the asymptotic method accurately predicts symmetrical-incidence scattering for rounding as small as $ka = 5$. The chapter concludes with comment on the relative utility of asymptotic and conventional physical optics in the present application.

In Chapter 4, the boundary value solution of Chapter 2 is viewed as the sharp wedge result plus a perturbation field. Following identification of the aspect dependence of perturbation fields, a parametric form for the expansion coefficients is sought. The resultant analytical expressions for perturbation fields enable treatment of targets with moderately rounded edges.

Chapter 5 contains applications of analysis performed in Chapter 4 to scattering by targets with one or more rounded edges. The shapes investigated comprise modifications to the triangular prism, square prism, and finite, right-circular cylinder. The accuracy of approximate theory is evaluated by comparison with accurate scattering data obtained by numerical solution of an integral equation.

The generality of the boundary value approach of Chapter 2 is examined in Chapter 6. Following discussion of modified edges suitable for analysis, the problem of scattering by a truncated wedge is chosen for detailed investigation. These boundary value data are then used to

evaluate the capability of theoretical models which describe interactions between edge scattering centers.

Chapter 7 is a summary of findings with recommendations for future work. Appendix A contains detailed derivations associated with the application of asymptotic physical optics reported in Chapter 3. Appendix B presents formulas employed in calculating accurate scattering data based upon the integral equation formulation.

1.1 Review of Scattering Techniques

The study of scattering of electromagnetic waves from obstacles of arbitrary shape is a broad and comprehensive subject: Logan[1] lists 103 references to the literature on scattering by a sphere; Bouwkamp[2] gives approximately 585 references for the period 1940 through 1953; Corriher and Pyron[3] list 1420 references for the period 1957 to 1964. The fundamental problem is the determination of the total field in amplitude, phase and polarization in terms of the geometrical and material constants characteristic of a given configuration of source, receiver, and obstacle.

An important factor which decides the gross scattering characteristics of the target, once the polarization and aspect angle parameters are fixed, is the ratio between the dimensions of the scatterer and the wavelength of the illuminating radar. The three broad regions which have gradually evolved to aid in classifying this gross scattering behavior are called the Rayleigh, resonance and optics regions. Rayleigh scattering occurs where the body is much smaller than the illuminating wavelength, and scattering tends to be independent of both polarization and aspect angle. Radar cross section varies inversely as the fourth power

of wavelength (the well known Rayleigh law) and becomes dependent upon the volume of the scatterer. Resonance region scattering occurs when the body circumference is of the order of the illuminating wavelength. Here the characteristic phenomenon is a strong frequency dependence. This complication is not amenable to simple physical interpretation in general, and the resonance region represents one of the weakest areas of interpretative capability in scattering theory. When the wavelength is appreciably smaller than the scatterer, the target is said to lie in the optics region, and the dependence of radar cross section upon polarization, aspect angle, and frequency is determined by target shape. Most radar targets of interest lie in the optics region, and this is the area chosen for the present research.

Calculation of the electromagnetic scattering properties of any body is difficult, at best. The most satisfying solution is an exact one, and the major mathematical methods are classified as separation of variables, variational, and Wiener-Hopf techniques. Unfortunately, radar targets of interest are not directly amenable to exact analysis: indeed, the use of approximate theory is inevitable.

With the advent of high-speed digital computers, numerical procedures for evaluating differential and integral equations have evolved and the approach offers exciting possibilities. Results may be calculated with great accuracy, and numerical techniques apply for obstacles of arbitrary shape. The most serious disadvantage is that numerical techniques cannot be applied for very large bodies: When the characteristic dimension of the target is greater than a few wavelengths, both the computer storage requirement and the cost of computations become prohibitive.

As the name implies, the earliest approximate theories applicable in the optics region had their historical origin in the study of light. The two basic theories are geometric optics, which is treated by the method of rays, and physical optics, which involves primarily the theory of waves. Geometric optics is a very accurate method for computing the magnitude of specular scattering from surfaces with radii of curvature large compared to a wavelength. Physical optics is one step more advanced in that it takes into account the phasor nature of scattering. Although it is useful for a large number of cases, it can lead to serious errors, mainly because of the assumed current distribution. Because of the importance of physical optics and its widespread use, a more detailed discussion is included with its application in Chapter 3.

Among the most powerful techniques for the calculation of radar scattering from bodies more than a wavelength in size are those based upon one form or another of asymptotic analysis. Here the electromagnetic field is expanded as a series in reciprocal powers of the wave number k. Kline and Kay[4] detail Luneberg's asymptotic expansion of Maxwell's equations. Their book serves as a good source of information on the asymptotic forms of Maxwell's equations and related problems, but does not give many practical applications. By far the most practical application is the geometrical theory of diffraction developed principally by J.B. Keller at New York University. The best general introduction to the geometrical theory of diffraction is given by Keller.[5] As pointed out by Kline and Kay,[4] Keller's method is without rigorous mathematical foundation but gives highly accurate results in many cases. Applications of Keller's theory are discussed in this thesis because of its direct

applicability to many targets of interest and because of the excellent results that have been obtained with it.

1.2 Scattering Center Concept

1.2.1 General

The most important concept that has been applied in recent investigations of short wavelength scattering is that the scattered fields appear to have localized sources (the so-called "scattering centers") on the target. In terms of formal electromagnetic theory, each scattering center is identified with a mathematical discontinuity in the Chu-Stratton radiation integral -- that is to say, with a corresponding physical location on the target at the place where the discontinuity occurs. Simplification of the scattering interaction in terms of scattering centers rests largely upon the cancellation properties of an integral with oscillating integrand and upon preservation of mathematical continuity except at the recognized geometric discontinuities. Thus, although a smooth surface remote from a discontinuity is assumed to produce a net contribution of zero to the total scattered field, truncation of the smooth surface could introduce a pronounced discontinuity and, so, generate a new scattering center. A smooth surface, then, plays a very important, although largely hidden,* role in the description of the scattering interaction in terms of scattering centers.

---

*Cancellation does not occur on a smooth surface at specular aspects. Rather, reinforcement occurs and the scattering centers extend to a scattering line on a surface with one infinite radius of curvature, or scattering area on a surface with two infinite radii of curvature.

According to the scattering center concept, the field reradiated from each center depends primarily upon the local dimensions and the surface conditions of the target. Secondary effects involve interactions between the various scattering centers on the target. The first step in the analysis is to take a body of complex shape and find its individual scattering centers. Next, an analytical theory which accounts for aspect, frequency, polarization, and bistatic dependence is used to estimate the total field (primary and secondary contributions) reradiated from individual scattering centers. Finally, the vector and phasor sum of these contributions allows calculation of radar observables; these are then compared with radar-range measurements for the integrated model to check the validity of the analytical approach.

1.2.2 Formulation

According to the scattering center concept, the radar cross section of the target is given by the square of the absolute value of the complex scattering coefficient $\sqrt{\sigma}\, e^{j\rho}$ which in turn is given by

$$\sqrt{\sigma}\, e^{j\rho} = \sum_{i=1}^{N} \sqrt{\sigma_i}\; e^{j\rho_i} \tag{1.1}$$

where $\sqrt{\sigma_i}\, e^{j\rho_i}$ is the complex contribution from the i^{th} scattering center, and where there are N important scattering centers on the target. The radar cross section σ is given by

$$\sigma = \left| \sum_{i=1}^{N} \sqrt{\sigma_i}\; e^{j\rho_i} \right|^2 \tag{1.2}$$

and the scattering phase ρ is given by

$$\rho = \tan^{-1}\left\{\frac{\sum_{i=1}^{N}\sqrt{\sigma_i}\,\sin\rho_i}{\sum_{i=1}^{N}\sqrt{\sigma_i}\,\cos\rho_i}\right\} \tag{1.3}$$

Scattering is expressed as an explicit function of radar polarization when the scattering matrix is introduced.[6] It is easily demonstrated[7] that the scattering matrix of a body containing a horizontal plane of symmetry (this includes bodies of revolution) is known when we solve for the principal polarization values of $\sqrt{\sigma_i}$ and ρ_i. Then scattering can be calculated for arbitrary combinations of transmitting- and receiving-antenna polarizations.

1.2.3 Utility of the Scattering Center Concept

The scattering center concept can be shown experimentally to be justified by employing a radar which transmits pulses which are short compared to target dimensions.[8,9] The validity of the approach can also be demonstrated by comparing predictions based upon the scattering center concept with conventional measurement data.

The scattering center concept is inherent in one high-frequency asymptotic theory, namely, the geometrical theory of diffraction. Specifically, the geometrical theory of diffraction allows estimation of the complex contribution $\sqrt{\sigma_i}\,e^{j\rho_i}$ reradiated from scattering centers associated with creeping wave phenomena and diffraction by sharp edges. Previous studies reported by the author have established the utility of geometrical diffraction theory in predicting high-frequency scattering by finite, conducting targets (e.g., rectangular flat plate,[10,11] dihedral

corner reflector,[12] right-circular cone,[13] rectangular and right-circular cylinders,[14,15,16,17] frustum,[18] and combinations of the latter two shapes[12]). Closely related studies which compare theory and measurement have also been reported by Keller,[19] Bechtel,[20,21] Rudduck and Yu,[22] Yu,[23], Ryan and Peters,[24] and by Senior and Uslenghi.[25] More general discussions which aid in the application of scattering center theory are contained in Keller,[5,26] Helstrom,[27] Ross,[28,29] Ryan,[30] and Bechtel and Ross.[31] Much of the above material has been collected by Ruck, Barrick, Stuart and Krichbaum[32] and the author's results appear in a recent book edited by Skolnik.[33] Finally, all of the above results attest the validity of the scattering center concept and only the salient points revealed there are discussed below.

By virtue of the asymptotic relationship between scattering center theory and exact theory, approximate formulas for radar cross section and scattering phase show explicit dependence upon all radar parameters (wavelength, polarization, bistatic angle) and all target parameters (size, shape, aspect angle). Although the method has shown instances of utility extending to the low end of the resonance region, its major advantages are realized in high-frequency applications where a realistic analytical alternative does not exist. Further, prediction accuracy increases with increase in target size-to-wavelength ratio, with time required for computation being related only to target shape. The scattering center concept provides a powerful tool for synthesis. Successful treatment of one type of center allows prediction of re-radiation from the same center located on an otherwise different target. This building block characteristic enables a unified analysis of high-frequency scattering.

The above advantages apply specifically in the prediction of radar observables. The scattering center concept has also proved useful as a guide to analysis. Kell[34] derived a bistatic-monostatic equivalence theorem based upon it rather than upon physical optics as was an earlier more approximate relationship that has been frequency cited.[35] Ross and Bechtel[36] applied the scattering center concept to obtain a realistic analysis of glint. Kell and Ross[37] used the scattering center concept as the basis of an approximate solution to the inverse scattering problem (i.e., given the electromagnetic field reradiated by an unknown target, find its size and shape).

1.3 Major Research Areas

With all the advantages attendant with the scattering center simplification, and not withstanding the fact that it is the only practical approach to high-frequency scattering prediction, the small number of centers having known reradiation characteristics has placed the approach in jeopardy. To date, predictions have been founded upon the known reradiation characteristics of but two centers. One center gives rise to creeping waves and the other center is the sharp edge. It is necessary to enlarge the class of scattering centers having known reradiation characteristics to provide generality. Here we review the status of previous investigations of corner, tip, and modified edge scattering centers. While other centers may occur to the reader, these three types represent the most important "building blocks" now missing.

1.3.1 Corner

The scattering center formed by a planar corner has received some attention. Kraus[38] examined the canonical problem of a quarter

plane but found the solution intractable for asymptotic evaluation. More recently, Satterwhite[39] treated the general planar corner as a limiting form of the solution for an elliptic cone. Hopefully, this latter approach will provide an analytical approximation of the reradiation process. The only available formulas for a plane corner are given by Keller, Lewis, and Seckler;[40] however, they were derived from physical optics, whose validity here is extremely suspect.

As an example of the application of the unknown corner scattering center, consider scattering by a rectangular flat plate at aspects other than those confined to the principal planes. Then diffraction arises at the four plate corners. Thus, the reradiation characteristics of the corner scattering center are necessary in removing present aspect limitations.

1.3.2 Tip

The three-dimensional tip is another scattering center whose reradiation characteristics have been investigated. Felsen[41] obtained a solution for the canonical problem of a semi-infinite cone and reported an asymptotic expression for tip scattering for narrow angle cones. Unfortunately, his result is only valid for angles near the axial aspect where the tip return is usually negligible. For a conical tip with radiation incident along the axis, the backscattering has been calculated by Siegel, et al.[42] in the limiting cases of cones with small and large apex angles. It is surprising that, although the result is based upon physical optics, it agrees with the first term in the asymptotic expansion of the exact solution.

Knowledge of the diffraction by a conical tip is necessary prior to obtaining good agreement between theory and measurement for a finite cone.

1.3.3 Modified Edge

The sharp edge is characterized by a discontinuous normal. Consider modifications to a sharp edge such that various degrees of smoothing are involved. The modified edge will exhibit a continuous normal with discontinuity in higher derivatives of the normal at the junctions. For example, a circular-cylindrical sector joined smoothly to a wedge gives rise to a continuous normal and a discontinuity in the first derivative of the normal. An elliptical-cylindrical sector faired to the wedge gives rise to a continuous normal and first derivative, but a discontinuity in the second derivative of the normal at the join. Increasing the degree of smoothness places the discontinuity in higher derivatives of the normal.

The amount of diffraction arising at the discontinuity in the n^{th} derivative of the normal decreases as n increases. Thus, a logical approach to enlarging the catalogue of edge scattering centers requires initial consideration of an edge modified so that a discontinuity exists in the first derivative of the normal. We uniformly refer to this shape as the rounded edge. Ross[28] suggested an application of numerical integration techniques to predict scattering by a rounded edge. However, no satisfactory method for truncating the integral equation calculation in a region local to the rounded edge could be developed.

Once the rounded edge has been satisfactorily treated, scattering center theory can be extended to include targets which exhibit rounded

as well as sharp edges. This extension is necessitated by practical considerations. Aerospace vehicles comprise an important class of radar targets having rounded rather than sharp edges. Here rounding is introduced for aerodynamic reasons as well as the minimization of nonspecular radar returns.

In summary, both the corner and the tip require further research prior to inclusion in the catalogue of scattering centers having known reradiation characteristics. The rounded edge is chosen for study in this thesis since little is presently known about this center despite its importance in practical applications.

1.4 Rounded Edge

1.4.1 Scattering Center Model for a Rounded Edge

The monostatic scattering center model for a rounded edge is a function of the degree of rounding. For small rounding, the edge will reradiate as a single center. For large rounding, returns arise from a maximum of three regions on the edge so that a model comprising three scattering centers is required.

A general monostatic model for the rounded edge consists of the three centers labelled in Fig. 1.1. The obstacle is formed by mating a cylindrical sector to the tip of a semi-infinite wedge so that the tangent is continuous at the joins. α is the half angle of the wedge, and a is the radius of the cylinder. A monostatic aspect angle θ is referenced to the axis of symmetry. Center S_s is located on the cylindrical sector and gives rise to a specular return for $-(\pi/2-\alpha) \leq \theta \leq (\pi/2-\alpha)$. Centers S_{j1} and S_{j2} are identical; both are located at the join and support diffraction from the discontinuity in the first derivative of the normal at

these points. S_{j1} contributes directly to the backscattering for $-\alpha \leq \theta \leq (\pi-\alpha)$; a corresponding return from S_{j2} exists for $-(\pi-\alpha) \leq \theta \leq \alpha$. Where the electrical radius of curvature is large $(ka >> 1)$, the three scattering centers will reradiate independently. As the rounding is decreased to moderate value $(ka \sim 2)$, the return from S_S will decrease and interactions between centers S_{j1} and S_{j2} will become appreciable. For rounding less than moderate (say $ka < 2$), strong interactions between centers will considerably complicate the three scattering center description. In the limit of vanishing curvature, the return from S_S diminishes to zero, and the direct and interaction terms associated with S_{j1} and S_{j2} will reduce to the sharp wedge result.

The complexity of the above model for scattering by a wedge with rounded edge is a function of the degree of rounding. This situation reflects in a natural division of further discussion depending upon small or large rounding.

(1) Large Rounding $(ka > 2)$

Presently, there exists a description of the specular return from the center S_S based upon geometric optics. The formula is valid for $ka \geq 2$. This, and the desire for negligible interactions, accounts for the otherwise arbitrary choice of lower limit on ka being discussed. Knowledge of the direct reradiation characteristics of the join scattering center would thus complete the model for large rounding.

Diffraction by a join scattering center is best studied by asymptotic evaluation of the corresponding canonical problem; that is, the isolated geometry of exterior space bounded by a circular arc joined tangentially to a plane. This isolated geometry has been analyzed by

Hong and Weston,[43] using an integral formulation. Their research was directed toward evaluation of the creeping waves launched at the second order join discontinuity. It was later expanded by Stone and Sleator[44] to determine reradiation from the join in the forward direction (more specifically, in the deep shadow region). What is required here is the manipulation of the asymptotic solution of the integral to apply for monostatic scattering by the join. The similar problem of the smooth join formed by two parabolic cylinders has been treated by Weston.[45] Because the surface fields for the rounded edge are known, the difficulty involves proper approximation to the Green's function and evaluation of the resulting integral expressions. It may take several different expressions for the Green's function in the various regions, but this is a detail. With enough patience and ingenuity, Weston's approach should provide an asymptotic description of reradiation by the join scattering center.

(2) Moderate Rounding ($ka \sim 2$)

For very small rounding, the modified edge reradiates essentially the same as the sharp edge. Even for roundings such that the modified edge ceases to act like a sharp edge, the modified edge will reradiate as an individual scattering center because the separation between all three centers is a small fraction of a wavelength. Due to complications attendant with the three center model, it is worthwhile to examine whether an effective single center description can be maintained for moderate roundings. However, the answer to this question requires the determination of the scattering by a rounded edge as a function of ka.

1.4.2 Reradiation Characteristics of a Rounded Edge

The reradiation characteristics of a rounded edge may be determined by solving the problem of a semi-infinite wedge with rounded edge. The solution can be found using either an integral equation formulation or a boundary value approach. We choose the boundary value approach because it is simpler for this problem. What we require is the amplitude and phase of the far fields scattered by a wedge with rounded edge for plane wave excitation. Here phase information is necessary in the scattering center formulation (see (1.1) through (1.3)). Of course, findings in the two-dimensional case may be generalized to three-dimensional edges by applying the divergence factor of geometrical diffraction theory.[31]

Following the completion of research, but prior to the compilation of this thesis, a solution for the wedge with rounded edge was reported in Hunter's[46] thesis*. Our approach entails an independent solution to the same problem as one step in the application of results for predicting scattering by finite targets. Because of common areas of investigation, parallels between Hunter's work and ours are drawn where appropriate in this thesis.

---

* Hunter's calculations of the magnitude of the scattered field constitute one illustration of the application of the surface current density replacement technique. This technique enables the scattering from any size body to be determined to a given accuracy after the inversion of one finite matrix, provided that the shape of the body can be derived by inwardly deforming a finite part of a body from which the scattering is known explicitly.

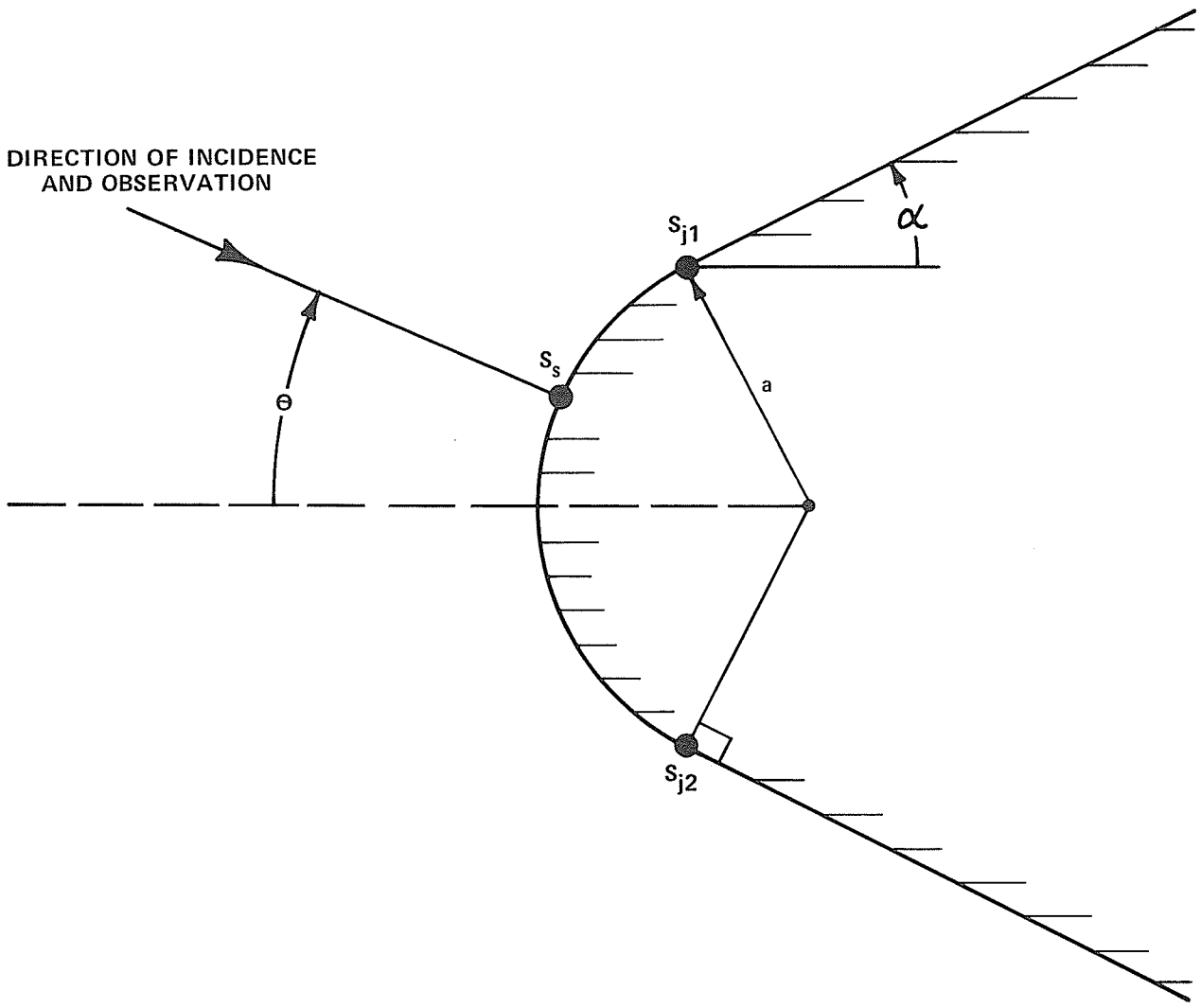

Figure 1.1 SCATTERING CENTERS ON A ROUNDED EDGE

2. BOUNDARY VALUE SOLUTION FOR THE ROUNDED EDGE

In this chapter, boundary value theory is applied to the wedge with rounded edge and the behavior of the scattered field under plane wave excitation is examined for both principal polarizations. Of special importance is the dependence of the scattered field on the electrical radius of the tip (ka) and the degree of curvature beyond which the rounded edge ceases to be satisfactorily described by the known diffraction coefficient for the sharp edge (i.e., as $ka \to 0$).

The vertical polarization boundary value problem (TM case) is formulated in Section 2.1 by an eigenfunction expansion for the fields such that the boundary and radiation conditions are satisfied. In Section 2.2 the continuity of field components required across the circular cylindrical matching boundary determines an infinite set of simultaneous equations in the unknown expansion coefficients. Section 2.3 contains the derivation of vertical-polarization formulas specialized to scattering due to plane wave incidence. Since most of the TE solution is similar in detail, Section 2.4 treats only those departures peculiar to construction of corresponding horizontal-polarization formulas.

Effects of truncating the infinite set of simultaneous equations for expansion coefficients is discussed in Section 2.5; in particular, one can anticipate ill-conditioning of the system for large ka and narrow wedge angles. Upon choice of convenient values for these two parameters, typical data are presented which indicate numerically the degree of satisfaction of boundary conditions, continuity of fields across the matching boundary, and stability of monostatic scattering predictions with respect to truncation limits.

Calculations of principal-polarization backscattered fields are presented in Section 2.6 in the form of plots of range-independent magnitude and phase vs. aspect angle as a function of ka for 60°, 90° and 120° wedge angles. The gross dependence of magnitude upon ka is compared with expectations based upon simple scattering arguments. Calculations of bistatic scattering are discussed in Section 2.7 where the relative strengths of shadow-region fields associated with sharp and rounded wedges are compared.

In Section 2.8 we examine scattering by a cylindrically tipped wedge to the extent that it affects the accuracy of our solution for the wedge with rounded edge. The capability of approximate theory for predicting symmetrical-incidence backscattering from a cylindrically tipped wedge is evaluated. Comments on the analysis in Chapter 2 are presented in Section 2.9.

Related boundary value solutions include those for a wedge, a cylinder, and a wedge with cylindrical tip.[47] The cone with rounded tip is the three-dimensional equivalent of the problem under investigation; of course, the details of the analysis employed by Weiner and Borison[48] differ markedly.

2.1 Formulation of the Problem

Consider a two-dimensional, semi-infinite, perfectly conducting wedge with a rounded edge, as shown in Fig. 2.1. The two surfaces of the wedge are tangential to the tip so that the cylinder and wedge sections form a continuous profile. For the sake of convenience we locate the axis of the cylindrical section and the virtual apex of the wedge section along the z axis of the polar coordinate systems (ρ, θ) and (r, ϕ), respectively. Once the wedge half-angle α and tip radius a are chosen, the distance d

separating the origins of the two coordinate systems is given by

$$d = a \csc \alpha \tag{2.1}$$

while the circular cylindrical matching boundary (R,ϕ) is determined by

$$R = d \cos \alpha = a \cot \alpha ; \quad \alpha \leq \phi \leq 2\pi - \alpha . \tag{2.2}$$

It is convenient to subdivide exterior space into the three regions indicated in Fig. 2.1. Region I is confined by the matching boundary and the rounded edge

$$0 \leq r \leq R ; \ \alpha \leq \phi \leq 2\pi - \alpha$$

$$0 \leq r \leq R \sec \alpha \left[\cos \phi - (\cos^2 \phi - \cos^2 \alpha)^{1/2}\right] ; \ -\alpha \leq \phi \leq \alpha .$$

Region II extends from region I to the cylindrical surface passing through the line source excitation at $(r_o, \phi_o$ or $\rho_o , \theta_o)$ and is bounded by the wedge sector

$$R \leq r \leq r_o ; \ \alpha \leq \phi \leq 2\pi - \alpha .$$

Region III extends from region II to infinity excluding the wedge,

$$r_o \leq r \leq \infty ; \ \alpha \leq \phi \leq 2\pi - \alpha .$$

Our procedure is to choose a series expansion of $E_z(H_z)$ in each region, subject to boundary conditions and the radiation condition. Integration across the appropriate line source and application of continuity of fields across the matching boundary leads, with the aid of orthogonality conditions, to the unknown expansion coefficients associated with the fields in region II. By extending the locations of the source and observation point to infinity, the desired expression for the far scattered field $E_z(H_z)$ produced by an incident plane wave is obtained. We may assume that

all vectors are independent of z and have time dependence $e^{j\omega t}$ (suppressed). Then all Hankel functions are of the second kind and the superscript (2) is implied throughout.

For an electric line source (TM or vertical polarization case), the non-vanishing field components are E_z, H_r and H_ϕ where the latter two fields are obtained from E_z via Maxwell's equations. Thus the expressions for the total electric field in regions II and III which satisfy the boundary condition $E_{tan} = 0$ on the wedge and the radiation condition are given by

$$E_z^{III}(r,\phi) = \sum_{n=1}^{\infty} a_n H_{\frac{n}{\gamma}}(kr) \sin\left[\frac{n}{\gamma}(\phi - \alpha)\right] \tag{2.3}$$

$$E_z^{II}(r,\phi) = \sum_{n=1}^{\infty} \left[b_n J_{\frac{n}{\gamma}}(kr) + c_n H_{\frac{n}{\gamma}}(kr)\right] \sin\left[\frac{n}{\gamma}(\phi - \alpha)\right] \tag{2.4}$$

where a_n, b_n, c_n are the unknown expansion coefficients, $k = 2\pi/\lambda$, $\gamma = \psi/\pi$ where ψ is the exterior wedge angle $2\pi - 2\alpha$, and the superscripts on the field denote the region of validity.

In region I the total electric field must satisfy the boundary condition $E_{tan} = 0$ on the cylindrical sector and must be free from singularities. Initially we choose a form of the cylinder solution in the ρ, θ, z coordinate system valid for an exterior line source ($\rho_o > \rho$) of intensity I_o [49]

$$E_z^I(\rho,\theta) = -\frac{k^2 I_o}{4\omega\epsilon} \sum_{p=0}^{\infty} H_p(k\rho_o)\left[J_p(k\rho) - \frac{J_p(ka)}{H_p(ka)} H_p(k\rho)\right] d_p \cos p\theta; \quad \rho \geq a \tag{2.5}$$

Since (2.5) exhibits even angular dependence, whereas the general form for the field in region I must contain even and odd angular dependence, we rewrite it in the form

$$E_z^I(\rho,\theta) = -\frac{k^2 I_0}{4\omega\epsilon}\sum_{p=0}^{\infty} H_p(k\rho_0)\left[J_p(k\rho)-\frac{J_p(ka)}{H_p(ka)}H_p(k\rho)\right]\left[d_p\cos p\theta + f_p \sin p\theta\right] \tag{2.6}$$

where the coefficient f_0 is recognized to be zero. Next we express (2.6) in terms of the polar coordinates (r,ϕ) using the usual addition theorem for the cylindrical functions,

$$Z_p(k\rho)\begin{Bmatrix}\cos\\ \sin\end{Bmatrix} p\theta = \sum_{q=-\infty}^{\infty} Z_{p+q}(kd)\, J_q(kr)\begin{Bmatrix}\cos\\ \sin\end{Bmatrix} q\phi \tag{2.7}$$

In (2.7), when Z represents a Bessel function of the first kind, there are no restrictions since p is an integer. When Z represents a Hankel function the condition d > r must be observed; however, this condition is satisfied for all points in region I. It is to be noted that (2.7) does not introduce fictitious singularities at the origin of the (r,ϕ) coordinate system. Hence applying (2.7) to the observation coordinates of (2.6) we have

$$E_z^I(r,\phi) = -\frac{k^2 I_0}{4\omega\epsilon}\sum_{p=0}^{\infty} H_p(k\rho_0)\sum_{q=-\infty}^{\infty} J_q(kr)\left[J_{p+q}(kd)-\frac{J_p(ka)}{H_p(ka)}H_{p+q}(kd)\right] \times \left[d_p\cos q\phi + f_p \sin q\phi\right] \tag{2.8}$$

The nonvanishing components of the magnetic field are

$$H_r(r,\phi) = \frac{-1}{j\omega\mu r}\frac{\partial E_z}{\partial \phi} \tag{2.9}$$

$$H_\phi(r,\phi) = \frac{1}{j\omega\mu}\frac{\partial E_z}{\partial r} \tag{2.10}$$

which are given in regions I and II by the relations

$$H_r^I(r,\phi) = \frac{I_0}{4jr}\sum_{p=0}^{\infty} H_p(k\rho_0)\sum_{q=-\infty}^{\infty} J_q(kr)\left[J_{p+q}(kd)-\frac{J_p(ka)}{H_p(ka)}H_{p+q}(kd)\right] \times \left[-q\, d_p \sin q\phi + q f_p \cos q\phi\right] \tag{2.11}$$

$$H_\phi^I(r,\phi) = \frac{-I_o k}{4j}\sum_{p=0}^{\infty} H_p(k\rho_o)\sum_{q=-\infty}^{\infty} J_q'(kr)\left[J_{p+q}(kd) - \frac{J_p(ka)}{H_p(ka)}\,H_{p+q}(kd)\right] \times \left[d_p \cos q\phi + f_p \sin q\phi\right] \tag{2.12}$$

$$H_r^{II}(r,\phi) = -\frac{1}{j\omega\mu r}\sum_{n=1}^{\infty} \frac{n}{\gamma}\left[b_n J_{\frac{n}{\gamma}}(kr) + c_n H_{\frac{n}{\gamma}}(kr)\right]\cos\left[\frac{n}{\gamma}(\phi-\alpha)\right] \tag{2.13}$$

$$H_\phi^{II}(r,\phi) = \frac{k}{j\omega\mu}\sum_{n=1}^{\infty}\left[b_n J_{\frac{n}{\gamma}}'(kr) + c_n H_{\frac{n}{\gamma}}'(kr)\right]\sin\left[\frac{n}{\gamma}(\phi-\alpha)\right] \tag{2.14}$$

where the prime notation denotes differentiation with respect to the total argument kr.

2.2 Determination of the Expansion Coefficients

In this section we apply the continuity conditions on the tangential fields in the three regions to determine the unknown expansion coefficients b_n, c_n, d_p, and f_p.

To evaluate b_n, we view the current element as an impulse of current on the sheet $r = r_o$. The boundary condition to be satisfied at a current sheet is[29]

$$J_z = H_\phi(r_o+) - H_\phi(r_o-) = H_\phi^{III}(r_o) - H_\phi^{II}(r_o) \tag{2.15}$$

Employing (2.14) and substituting (2.3) into (2.10) we obtain

$$J_z = \frac{k}{j\omega\mu}\sum_{n=1}^{\infty}\left[a_n H_{\frac{n}{\gamma}}'(kr_o) - b_n J_{\frac{n}{\gamma}}'(kr_o) - c_n H_{\frac{n}{\gamma}}'(kr_o)\right]\sin\left[\frac{n}{\gamma}(\phi-\alpha)\right] \tag{2.16}$$

From the continuity of E_z at $r = r_o$ it follows that

$$a_n H_{\frac{n}{\gamma}}(kr_o) = b_n J_{\frac{n}{\gamma}}(kr_o) + c_n H_{\frac{n}{\gamma}}(kr_o) \tag{2.17}$$

which may be inserted into (2.16), and simplified using the Wronskian relation for the Bessel and Hankel functions. This approach leads to

$$J_z = \frac{-2}{\pi r_o \omega \mu} \sum_{n=1}^{\infty} b_n \frac{\sin\left[\frac{n}{\gamma}(\phi - \alpha)\right]}{H_{\frac{n}{\gamma}}(k r_o)} \tag{2.18}$$

Since the current sheet for a line source is simply an impulse current of strength I_o at $r = r_o$, $\phi = \phi_o$, we have

$$J_z = I_o \frac{\delta(\phi - \phi_o)}{r_o} \tag{2.19}$$

so that

$$\delta(\phi - \phi_o) = \frac{-2}{I_o \pi \omega \mu} \sum_{n=1}^{\infty} b_n \frac{\sin\left[\frac{n}{\gamma}(\phi - \alpha)\right]}{H_{\frac{n}{\gamma}}(k r_o)} \tag{2.20}$$

Multiplying both sides of (2.20) by $\sin\left[\frac{m}{\gamma}(\phi - \alpha)\right]$, integrating over the range $\alpha \leq \phi \leq 2\pi - \alpha$, and using the orthogonality relation for the sine functions leads to

$$b_n = \frac{-\omega \mu \pi I_o}{\psi} H_{\frac{n}{\gamma}}(k r_o) \sin\left[\frac{n}{\gamma}(\phi_o - \alpha)\right] \tag{2.21}$$

Next we impose continuity of the tangential fields E_z and H_ϕ across the matching boundary ($r = R$, $\alpha \leq \phi \leq 2\pi - \alpha$) between regions I and II to obtain c_n as a function of d_p and f_p, and sets of simultaneous equations allowing the determination of d_p and f_p. Thus equating (2.8), (2.12), to (2.4), (2.14) we have from the continuity of E_z

$$\sum_{n=1}^{\infty} \left[b_n J_{\frac{n}{\gamma}}(kR) + c_n H_{\frac{n}{\gamma}}(kR)\right] \sin\left[\frac{n}{\gamma}(\phi - \alpha)\right] = -\frac{k^2 I_o}{4\omega\epsilon} \sum_{p=0}^{\infty} H_p(k\rho_o) \times \tag{2.22}$$

$$\sum_{q=-\infty}^{\infty} J_q(kR)\left[J_{p+q}(ka) - \frac{J_p(ka)}{H_p(ka)} H_{p+q}(ka)\right]\left[d_p \cos q\phi + f_p \sin q\phi\right]$$

and from the continuity of H_ϕ

$$\sum_{n=1}^{\infty}\left[b_n J'_{\frac{n}{\gamma}}(kR)+c_n H'_{\frac{n}{\gamma}}(kR)\right]\sin\left[\frac{n}{\gamma}(\phi-\alpha)\right]=\frac{-k^2 I_o}{4\omega\epsilon}\sum_{p=0}^{\infty}H_p(k\rho_o)\sum_{q=-\infty}^{\infty}J'_q(kR)\times \tag{2.23}$$

$$\left[J_{p+q}(kd)-\frac{J_p(ka)}{H_p(ka)}H_{p+q}(kd)\right]\left[d_p\cos q\phi+f_p\sin q\phi\right]$$

Equations (2.22) and (2.23) relate four sets of expansion coefficients, three of which are unknown. In fact, we have four equations and four unknowns since both equations exhibit dependence upon even and odd functions of ϕ along the matching boundary. For n odd, $\sin\left[\frac{n}{\gamma}(\phi-\alpha)\right]$ generates even functions of ϕ with magnitudes having one maximum occuring at $\phi=\pi$. For n even, on the other hand, this function is odd and vanishes for $\phi=\pi$. Thus due to the orthogonality of even and odd functions, (2.22) and (2.23) may be satisfied independently for both types. The coefficients d_p may hence be determined in terms of odd c_n which corresponds to matching even angular functions. Similarly, the coefficients f_p are related to even c_n in the matching of odd angular functions. Bearing this in mind, we multiply (2.22) and (2.23) by $\sin\left[\frac{m}{\gamma}(\phi-\alpha)\right]$ where q and m are integers, and integrate over ϕ in the range $\alpha\le\phi\le 2\pi-\alpha$. Since on the left hand side the angular functions are complete over this range, the orthogonality condition applies and we obtain

$$\frac{\psi}{2}\left[b_m J_{\frac{m}{\gamma}}(kR)+c_m H_{\frac{m}{\gamma}}(kR)\right]=\frac{-k^2 I_o}{4\omega\epsilon}\sum_{p=0}^{\infty}H_p(k\rho_o)\sum_{q=-\infty}^{\infty}J_q(kR)\times$$

$$\left[J_{p+q}(kd)-\frac{J_p(ka)}{H_p(ka)}H_{p+q}(kd)\right]\left[d_p I_1+f_p I_2\right] \tag{2.24}$$

$$\frac{\psi}{2}\left[b_m J'_{\frac{m}{\gamma}}(kR)+c_m H'_{\frac{m}{\gamma}}(kR)\right]=\frac{-k^2 I_o}{4\omega\epsilon}\sum_{p=0}^{\infty}H_p(k\rho_o)\sum_{q=-\infty}^{\infty}J'_q(kR)$$

$$\left[J_{p+q}(kd)-\frac{J_p(ka)}{H_p(ka)}H_{p+q}(kd)\right]\left[d_p I_1+f_p I_2\right] \tag{2.25}$$

where

$$I_1 = \int_{\alpha}^{2\pi-\alpha} \sin\left[\frac{m}{\gamma}(\phi-\alpha)\right]\cos q\phi \, d\phi$$

$$= \frac{\frac{m}{\gamma}}{\left(\frac{m}{\gamma}\right)^2-(q)^2}\left[1-(-1)^m\right]\cos q\alpha \; ; \qquad \frac{m}{\gamma} \neq |q| \tag{2.26}$$

$$= \pm \sin q\alpha\left[\frac{\psi}{2} - \frac{\sin 2q\alpha}{2q}\right]; \qquad \frac{m}{\gamma} = \mp q$$

and

$$I_2 = \int_{\alpha}^{2\pi-\alpha} \sin\left[\frac{m}{\gamma}(\phi-\alpha)\right]\sin q\phi \, d\phi$$

$$= \frac{\frac{m}{\gamma}}{\left(\frac{m}{\gamma}\right)^2-(q)^2}\left[1+(-1)^m\right]\sin q\alpha \; ; \qquad \frac{m}{\gamma} \neq |q| \tag{2.27}$$

$$= \pm \cos q\alpha\left[\frac{\psi}{2} + \frac{\sin 2q\alpha}{2q}\right]; \qquad \frac{m}{\gamma} = \pm q$$

At this point the closed form solutions for integrals I_1 and I_2 bear out the independence of even and odd angular functions on the boundary. From (2.26) it is apparent that the solution for d_p depends upon odd m, since I_2 is zero for all odd m. Similarly, even values of m determine the relationship between c_m and f_p.

To solve (2.24) and (2.25), we eliminate c_m on the left hand sides, substitute for b_n from (2.21) and employ the Wronskian relation for the Bessel and Hankel functions to obtain

$$\sum_{p=0}^{\infty} H_p(k\rho_o) \sum_{q=-\infty}^{\infty}\left[J_q(kR)\, H'_{\frac{m}{\gamma}}(kR) - J'_q(kR)\, H_{\frac{m}{\gamma}}(kR)\right] \times$$

$$\left[J_{p+q}(kd) - \frac{J_p(ka)}{H_p(ka)}\, H_{p+q}(kd)\right]\left[d_p I_1 + f_p I_2\right]$$

$$= \frac{-4j}{kR}\, H_{\frac{m}{\gamma}}(kr_o)\sin\left[\frac{m}{\gamma}(\phi_o-\alpha)\right] \tag{2.28}$$

Again, (2.28) represents a solution for d_p when m is odd, and for f_p when m is even, and leads to two independent sets of simultaneous equations. Solution of these equations completes the determination of all the expansion coefficients.

Substituting for b_n from (2.21) and for c_n from (2.24) into (2.4) we obtain

$$E_z^{II}(r,\phi) = \sum_{n=1}^{\infty} \left\{ \frac{-\omega\mu\pi I_o}{\Psi} H_{\frac{n}{\gamma}}(kr_o) \left[J_{\frac{n}{\gamma}}(kr) - \frac{J_{\frac{n}{\gamma}}(kR)}{H_{\frac{n}{\gamma}}(kR)} H_{\frac{n}{\gamma}}(kr) \right] \times \right.$$
$$\left[\sin\tfrac{n}{\gamma}(\phi-\alpha) \sin\tfrac{n}{\gamma}(\phi_o-\alpha) \right]$$
$$- \frac{k^2 I_o}{2\omega\epsilon\Psi} \frac{H_{\frac{n}{\gamma}}(kr)}{H_{\frac{n}{\gamma}}(kR)} \sum_{p=0}^{\infty} H_p(k\rho_o) \sum_{q=-\infty}^{\infty} J_q(kR) \times$$
$$\left. \left[J_{p+q}(kd) - \frac{J_p(ka)}{H_p(ka)} H_{p+q}(kd) \right] \left[d_p I_1 + f_p I_2 \right] \left[\sin\tfrac{n}{\gamma}(\phi-\alpha) \right] \right\} \tag{2.29}$$

which, in conjunction with (2.28), constitutes the solution of our problem.

2.3 Far Field Expansions for Plane Wave Incidence

Since the analysis of the previous section applies for $r_o > r$ ($\rho_o > \rho$), (2.28) and (2.29) may be specialized for plane wave illumination by letting the line source recede to infinity, i.e., r_o (ρ_o) $\to\infty$. Then approximate relations between ρ_o, r_o and θ_o, ϕ_o are given by

$$\theta_o \sim \pi - \phi_o \tag{2.30a}$$

$$\rho_o \sim r_o - d\cos\phi_o \tag{2.30b}$$

while the asymptotic expansion of the Hankel function of the second kind for fixed order ν and large argument x is given by[51]

$$H_\nu(x) \sim \left(\frac{2}{\pi x}\right)^{1/2} e^{-j(x-\pi/4-\nu\pi/2)} \tag{2.31}$$

Hence (2.28) reduces to

$$\sum_{p=0}^{\infty}\sum_{q=-\infty}^{\infty}\left[J_q(kR)\,H'_{\frac{m}{\gamma}}(kR) - J'_q(kR)\,H_{\frac{m}{\gamma}}(kR)\right] \quad X$$

$$\left[J_{p+q}(kd) - \frac{J_p(ka)}{H_p(ka)}\,H_{p+q}(kd)\right]\left[\alpha_p I_1 + f_p I_2\right] \tag{2.32}$$

$$= -\frac{4j}{kR}\,\sin\left[\frac{m}{\gamma}(\phi_o-\alpha)\right]\; e^{-j(kd\cos\phi_o - m\pi/2\gamma)}$$

while (2.29), together with (2.31) and the expansion for the incident field intensity[29]

$$E_z^i = -\frac{\omega\mu I_o}{4}\left(\frac{2}{\pi k r_o}\right)^{1/2} e^{-j(kr_o-\pi/4)} \tag{2.33}$$

reduces to the normalized relation

$$\frac{E_z^{II}(r,\phi)}{E_z^i} = \frac{4}{\gamma}\sum_{n=1}^{\infty}\left[J_{\frac{n}{\gamma}}(kr) - \frac{J_{\frac{n}{\gamma}}(kR)}{H_{\frac{n}{\gamma}}(kR)}\,H_{\frac{n}{\gamma}}(kr)\right] e^{jn\pi/2\gamma}\sin\left[\frac{n}{\gamma}(\phi-\alpha)\right]\sin\left[\frac{n}{\gamma}(\phi_o-\alpha)\right]$$

$$+\frac{2}{\psi}\,e^{jkd\cos\phi_o}\sum_{n=1}^{\infty}\frac{H_{\frac{n}{\gamma}}(kr)}{H_{\frac{n}{\gamma}}(kR)}\,\sin\left[\frac{n}{\gamma}(\phi-\alpha)\right] \quad X$$

$$\sum_{p=0}^{\infty}\sum_{q=-\infty}^{\infty} J_q(kR)\left[J_{p+q}(kd) - \frac{J_p(ka)}{H_p(ka)}\,H_{p+q}(kd)\right]\left[\alpha_p I_1 + f_p I_2\right] \tag{2.34}$$

where the factor $e^{jp\pi/2}$ in (2.32) and (2.34), due to the asymptotic relation (2.31), has been absorbed in the coefficients α_p and f_p. Examination of (2.34) shows that the term under the first summation on n is the solution for a plane wave incident on a wedge with cylindrical tip of radius R [47]. The second summation on n represents a modification to this solution due to the fact that the electric field in region I is not zero for a wedge with rounded edge.

To obtain the far scattered field $E_z^s(r,\phi)$ from (2.34), we use (2.31) and we employ the well known approximation for the field diffracted by a sharp wedge[52]. Further, extension of a soft scalar solution to the corresponding TM electromagnetic problem requires that we multiply the right hand side of (2.34) by minus one.[27] This assures that the Poynting vector points in the direction of the scattered wave. Thus we have

$$\frac{E_z^s(r,\phi)}{E_z^i} \sim \frac{e^{-j(kr+\frac{\pi}{4})}}{(2\pi kr)^{1/2}}\left\{\frac{\sin\frac{\pi}{\gamma}}{\gamma}\left[\frac{1}{\cos\frac{\pi}{\gamma}-\cos\left(\frac{\phi+\phi_o-2\alpha}{\gamma}\right)}-\frac{1}{\cos\frac{\pi}{\gamma}-\cos\left(\frac{\phi-\phi_o}{\gamma}\right)}\right]\right.$$

$$+\frac{8j}{\gamma}\sum_{n=1}^{\infty} e^{j\frac{n\pi}{\gamma}}\frac{J_{\frac{n}{\gamma}}(kR)}{H_{\frac{n}{\gamma}}(kR)}\sin\left[\frac{n}{\gamma}(\phi-\alpha)\right]\sin\left[\frac{n}{\gamma}(\phi_o-\alpha)\right] \qquad (2.35)$$

$$-\frac{4je^{j(k\alpha\cos\phi_o)}}{\psi}\sum_{n=1}^{\infty} e^{j\frac{n\pi}{2\gamma}}\frac{\sin\left[\frac{n}{\gamma}(\phi-\alpha)\right]}{H_{\frac{n}{\gamma}}(kR)}\times$$

$$\left.\sum_{p=0}^{\infty}\sum_{q=-\infty}^{\infty} J_q(kR)\left[J_{p+q}(k\alpha)-\frac{J_p(ka)}{H_p(ka)}H_{p+q}(k\alpha)\right]\left[d_p I_1+f_p I_2\right]\right\}$$

and the desired solution is given by (2.32) and (2.35).

2.4 Horizontal Polarization-(TE Case)

When the line source of Fig. 2.1 is a magnetic filament of intensity k_0 the problem is dual to the electric filament case. Since most of the analysis is similar in detail to that presented in Sections 2.1, 2.2, and 2.3, only those departures peculiar to the construction of the horizontal polarization solution are presented in this section.

The expansions for the magnetic fields in regions I, II and III are

$$H_z^{III}(r,\phi) = \sum_{n=0}^{\infty} A_n \, H_{\frac{n}{\gamma}}(kr) \, \cos\left[\frac{n}{\gamma}(\phi-\alpha)\right] \tag{2.36}$$

$$H_z^{II}(r,\phi) = \sum_{n=0}^{\infty} \left[B_n \, J_{\frac{n}{\gamma}}(kr) + C_n \, H_{\frac{n}{\gamma}}(kr)\right] \, \cos\left[\frac{n}{\gamma}(\phi-\alpha)\right] \tag{2.37}$$

$$H_z^{I}(r,\phi) = -\frac{k^2 k_0}{4\omega\mu} \sum_{p=0}^{\infty} H_p(k\rho_0) \sum_{q=-\infty}^{\infty} J_q(kr)$$

$$\left[J_{p+q}(ka) - \frac{J_p'(ka)}{H_p'(ka)} \, H_{p+q}(ka)\right]\left[D_p \cos q\phi + F_p \sin q\phi\right] \tag{2.38}$$

which are dual to (2.31), (2.41) and (208), respectively. The only other nonvanishing fields are the radial and angular components of the electric field which are given by

$$E_r(r,\phi) = -\frac{1}{j\omega\epsilon r} \, \frac{\partial H_z}{\partial \phi} \tag{2.39}$$

$$E_\phi(r,\phi) = \frac{1}{j\omega\epsilon} \, \frac{\partial H_z}{\partial r} \tag{2.40}$$

Equations (2.36) to (2.40) satisfy the boundary conditions on the obstacle and, where appropriate, the radiation condition at infinity.

To evaluate the unknown expansion coefficient B_n from (2.36), (2.37) and (2.38), we enforce continuity of H_z across the boundary $r = r_o$, $\alpha \leq \phi \leq 2\pi - \alpha$ and the boundary condition for the jump discontinuity at a magnetic current sheet, i.e.

$$M_z = E_\phi^{III}(r_o) - E_\phi^{II}(r_o) = \frac{K_o \delta(\phi - \phi_o)}{r_o} \tag{2.41}$$

where M_z is the magnetic analog of J_z. Applying orthogonality and simplifying the results using the Wronskian relation as before, we obtain

$$B_n = -\frac{\pi \omega \epsilon K_o \epsilon_n}{2\psi} H_{\frac{n}{\gamma}}(kr_o) \cos\left[\frac{n}{\gamma}(\phi_o - \alpha)\right] \tag{2.42}$$

where ϵ_n is the Neumann number, i.e.

$$\epsilon_n = \begin{array}{l} 1 \text{ for } n = 0 \\ 2 \text{ for } n \geq 1 \end{array} \tag{2.43}$$

The expansion coefficients D_p and F_p are evaluated by enforcing continuity of H_z and E_ϕ across the matching boundary $r = R$, $\alpha \leq \phi \leq 2\pi - \alpha$. Applying orthogonality to the matching equations and eliminating the coefficient C_n, we obtain the following sets of simultaneous equations

$$\sum_{p=0}^{\infty} H_p(kR_o) \sum_{q=-\infty}^{\infty} \left[J_q(kR) H'_{\frac{m}{\gamma}}(kR) - J'_q(kR) H_{\frac{m}{\gamma}}(kR) \right] \tag{2.44}$$

$$\left[J_{p+q}(kd) - \frac{J'_p(ka)}{H'_p(ka)} H_{p+q}(kd) \right] \left[D_p I_3 + F_p I_4 \right] = -\frac{4j}{kR} H_{\frac{m}{\gamma}}(kr_o) \cos\left[\frac{m}{\gamma}(\phi_o - \alpha)\right]$$

where

$$I_3 = \int_{\alpha}^{2\pi-\alpha} \cos\frac{m}{\gamma}(\phi-\alpha)\cos q\phi\, d\phi$$

$$= \frac{q}{\left(\frac{m}{\gamma}\right)^2-(q)^2}\left[1+(-1)^m\right]\sin q\alpha\,; \qquad \frac{m}{\gamma} \neq |q|$$

$$= \cos q\alpha\left[\frac{\psi}{2} - \frac{\sin 2q}{2q}\right]\,; \qquad \frac{m}{\gamma} = \pm q \tag{2.45}$$

$$= \psi\,; \qquad m = q = 0$$

and

$$I_4 = \int_{\alpha}^{2\pi-\alpha} \cos\frac{m}{\gamma}(\phi-\alpha)\sin q\phi\, d\phi$$

$$= \frac{-q}{\left(\frac{m}{\gamma}\right)^2-(q)^2}\left[1-(-1)^m\right]\cos q\alpha\,; \qquad \frac{m}{\gamma} \neq |q|$$

$$= \sin q\alpha\left[\frac{\psi}{2} + \frac{\sin 2q\alpha}{2q}\right]\,; \qquad \frac{m}{\gamma} = \pm q \tag{2.46}$$

$$= 0\,; \qquad m = q = 0$$

In the solution of the simultaneous equations for D_p and F_p, we notice that $I_3(I_4)$ vanishes for odd (even) m. Thus we again see that the even angular functions are matched across the matching boundary by the expansion coefficients D_p while, conversely, F_p match the odd angular functions. Furthermore the coefficient F_0, assigned for $p=0$, is identically zero.

The magnetic field in region II may be evaluated by eliminating C_n from (2.37), i.e.,

$$H_z^{II}(r,\phi) = \sum_{n=0}^{\infty}\left[J_{\frac{n}{\gamma}}(kr) - \frac{J'_{\frac{n}{\gamma}}(kR)}{H'_{\frac{n}{\gamma}}(kR)}H_{\frac{n}{\gamma}}(kr)\right]\left[-\frac{\pi\omega\epsilon\epsilon_n K_0}{2\psi}H_{\frac{n}{\gamma}}(kr_0)\right]\times$$

$$\left[\cos\frac{n}{\gamma}(\phi-\alpha)\cos\frac{n}{\gamma}(\phi_0-\alpha)\right] \tag{2.47}$$

$$-\frac{k^2K_0}{4\omega\mu\psi}\sum_{n=0}^{\infty}\epsilon_n\frac{H_{\frac{n}{\gamma}}(kr)}{H'_{\frac{n}{\gamma}}(kR)}\sum_{p=0}^{\infty}H_p(k\rho_0)\sum_{q=-\infty}^{\infty}J'_q(kR)\left[J_{p+q}(ka) - \frac{J'_p(ka)}{H'_p(ka)}H_{p+q}(ka)\right]$$

$$\left[D_pI_3 + F_pI_4\right]\cos\left[\frac{n}{\gamma}(\phi-\alpha)\right]$$

One finds the effective intensity of the incident plane wave to be

$$H_z^i = -\frac{\omega \epsilon K_o}{4} \left(\frac{2}{\pi k r_o}\right)^{1/2} e^{-j(kr_o - \frac{\pi}{4})} \tag{2.48}$$

Interpreting (2.47) for plane wave incidence, using (2.48) and the asymptotic expansion for the Hankel functions of the second kind for fixed order and argument approaching infinity, we have

$$\frac{H_z^{II}(r,\phi)}{H_z^i} = \frac{2}{\gamma} \sum_{n=0}^{\infty} \epsilon_n e^{jn\pi/2\gamma} \left[J_{\frac{n}{\gamma}}(kr) - \frac{J'_{\frac{n}{\gamma}}(kR)}{H'_{\frac{n}{\gamma}}(kR)} H_{\frac{n}{\gamma}}(kr) \right] \times$$

$$\left[\cos\frac{n}{\gamma}(\phi - \alpha) \cos\frac{n}{\gamma}(\phi_o - \alpha) \right] + \frac{e^{jkd\cos\phi_o}}{\psi} \sum_{n=0}^{\infty} \epsilon_n \times \tag{2.49}$$

$$\frac{H_{\frac{n}{\gamma}}(kr)}{H'_{\frac{n}{\gamma}}(kR)} \sum_{p=0}^{\infty} \sum_{q=-\infty}^{\infty} J'_q(kR) \left[J_{p+q}(kd) - \frac{J'_p(ka)}{H'_p(ka)} H_{p+q}(kd) \right] \times$$

$$\left[D_p I_3 + F_p I_4 \right] \cos\left[\frac{n}{\gamma}(\phi - \alpha)\right]$$

Again, the first sum over n in (2.49) is the solution for a plane wave incident on a wedge with cylindrical tip of radius R[47]. The second sum over n is that modification necessary to the solution for a wedge with rounded edge of radius a.

Finally, the expression for the far scattered field is given by

$$\frac{H_z^s(r,\phi)}{H_z^i} \sim \frac{e^{-j(kr+\frac{\pi}{4})}}{(2\pi kr)^{1/2}} \left\{ \frac{\sin\frac{\pi}{\gamma}}{\gamma} \left[\frac{1}{\cos\frac{\pi}{\gamma} - \cos\left(\frac{\phi+\phi_o-2\alpha}{\gamma}\right)} + \frac{1}{\cos\frac{\pi}{\gamma} - \cos\left(\frac{\phi-\phi_o}{\gamma}\right)} \right] \right.$$

$$- \frac{4j}{\gamma} \sum_{n=0}^{\infty} \epsilon_n e^{j\frac{n\pi}{\gamma}} \frac{J'_{\frac{n}{\gamma}}(kR)}{H'_{\frac{n}{\gamma}}(kR)} \left[\cos\frac{n}{\gamma}(\phi-\alpha) \cos\frac{n}{\gamma}(\phi_o-\alpha) \right] \qquad (2.50)$$

$$+ \frac{2je^{j(kd\cos\phi_o)}}{\psi} \sum_{n=0}^{\infty} \epsilon_n e^{j\frac{n\pi}{2\gamma}} \frac{\cos\left[\frac{n}{\gamma}(\phi-\alpha)\right]}{H'_{\frac{n}{\gamma}}(kR)} \times$$

$$\left. \sum_{p=0}^{\infty} \sum_{q=-\infty}^{\infty} J'_q(kR) \left[J_{p+q}(kd) - \frac{J'_p(ka)}{H'_p(ka)} H_{p+q}(kd) \right] \left[D_p I_3 + F_p I_4 \right] \right\}$$

with the expansion coefficients D_p and F_p determined by the two sets of simultaneous equations generated by

$$\sum_{p=0}^{\infty} \sum_{q=-\infty}^{\infty} \left[J_q(kR) H'_{\frac{m}{\gamma}}(kR) - J'_q(kR) H_{\frac{m}{\gamma}}(kR) \right] \left[J_{p+q}(kd) - \frac{J'_p(ka)}{H'_p(ka)} H_{p+q}(kd) \right] \times \qquad (2.51)$$

$$\left[D_p I_3 + F_p I_4 \right] = \frac{-4j}{kR} \cos\left[\frac{m}{\gamma}(\phi_o-\alpha)\right] e^{-j(kd\cos\phi_o - m\pi/2\gamma)}$$

Notice that the hard scalar solution applies directly to the corresponding TE electromagnetic problem.

2.5 Numerical Solution of the Infinite System of Equations

The infinite systems (2.34) and (2.49) have no closed form solution except in the near field for the limiting cases of the cylindrically tipped wedge ($kd = 0$) and the sharp wedge ($kd = ka = 0$). Unfortunately, the corresponding systems for the far-scattered field (2.35) and (2.50) do

not constitute closed form solutions because of slow convergence of the wedge series. The following discussion of truncation effect relates findings for the TM case; they are representative of dual parameters in the TE case as well.

For a wedge with rounded edge, region I expansion coefficients (d_p, f_p) are evaluated following truncation of the infinite series in m, p, and q in (2.32). When ka and kR are small, little error is introduced by truncating the independent sets of simultaneous equations to two $M \times M$ systems: small ka causes rapid decrease in row elements, whereas small kR causes similar decrease in column elements. When kd is small, rapid convergence of the q summation in each element is assured. Of course kR and kd are fixed once ka and the half-angle of the wedge α are chosen. Then one can expect little truncation error when ka is small and α is large. As ka increases or α decreases (and hence M increases), the coefficients of the unknown expansion coefficients also increase, and progressively more ill-conditioned systems result. At the outset then, one can anticipate failure of the method for large ka and small α.

A numerical investigation of the internal consistency of the boundary value solution was performed and representative results are presented in Tables 2.1 through 2.4 which are discussed in detail below. All data in these tables apply for plane wave incidence on a 90° wedge with rounding $ka = 1$. Equation (2.32) was truncated on m, p and q and solved by Gauss elimination, where matrix elements are complex valued functions as are the expansion coefficients dp and fp. The number of terms in each summation in (2.32) is denoted by M, $P(=M)$ and Q respectively. Field calculations will involve the same number of terms P and Q,

with a total number of modes $N=M$. Unless otherwise specified, we have chosen $M=5$ and $Q=65$ for the following study of internal consistency.

2.5.1 Satisfaction of Boundary Condition $E_{tan} = 0$

The boundary conditions require that the tangential component of the electric field (E_{tan}) be zero on the conductor. In region II, the conducting boundary is defined by $\phi_B = \pm\alpha$, $r_B \geq R$. Calculations were based upon $E_z^{II}(r_B, \phi_B)/E_z^i$ given by (2.34) since this quantity is directly proportional to E_{tan} in region II. In region I, points on the boundary of the cylindrical sector are given by the coordinates

$$r_B = R \sec\alpha \left[\cos\phi_B - \sqrt{\cos^2\phi_B - \cos^2\alpha}\right]$$

$$-\alpha \leq \phi_B \leq \alpha$$

and $E_z^I(r_B, \phi_B)/E_z^i$ was calculated using (2.8) following specialization of this equation for plane wave incidence.

Table 2.1 presents numerical results for $\phi_0 = \pi/2$ at 10° increments in ϕ_B. The tangential electric field on the conducting boundary vanishes to order 10^{-15} on the wedge section and to order 10^{-7} on the cylindrical sector, except at the joins where order 10^{-4} was calculated. The latter two estimates are higher since a mix of radial and angular functions is required to satisfy the boundary conditions. It is also required that the boundary condition be satisfied for each mode. Here it was found that each mode satisfied the boundary condition to the same order of magnitude as data presented in Table 2.1.

Table 2.1

TANGENTIAL COMPONENT OF ELECTRIC FIELD EVALUATED ON THE CONDUCTING BOUNDARY.

$\alpha = \pi/4$, ka = 1, $\phi_o = \pi/2$, M = 5, Q = 65

$\frac{E_z^I(r_B, \phi_B)}{E_z^i}$		
ϕ_B°	REAL PART	IMAGINARY PART
45	-0.4×10^{-4}	-0.5×10^{-4}
35	-0.8×10^{-6}	-0.7×10^{-6}
25	-0.1×10^{-6}	-0.4×10^{-6}
15	-0.2×10^{-6}	-0.1×10^{-6}
5	-0.6×10^{-6}	0.5×10^{-6}
-5	-0.6×10^{-6}	0.5×10^{-6}
-15	-0.6×10^{-6}	-0.2×10^{-6}
-25	-0.5×10^{-6}	0.2×10^{-6}
-35	-0.5×10^{-6}	-0.9×10^{-6}
-45	-0.6×10^{-4}	0.2×10^{-4}

$\frac{E_z^{II}(r_B, \phi_B)}{E_z^i}$		
ϕ_B°	REAL PART	IMAGINARY PART
+45	-0.2×10^{-15}	0.3×10^{-15}
-45	-0.4×10^{-15}	-0.7×10^{-15}

2.5.2 Continuity of Fields Across the Matching Boundary

Next we examine the degree of numerical satisfaction of continuity of fields across the matching boundary $r=R$; $\alpha \leq \phi_M \leq 2\pi-\alpha$.* The electric field in regions I and II may be evaluated on the boundary using (2.8) and (2.4). Table 2.2 presents calculations for plane wave incidence with $\phi_o = \pi/2$ and 10° steps in ϕ_M. Continuity between real parts and between imaginary parts of the electric field is good to at least 3 decimal places. Discrepancies are least when ϕ_M approaches ϕ_o where the error occurs in the 5th significant figure. Investigation of the continuity of magnetic field components H_ϕ and H_r revealed the same behavior; although the continuity of H_r degrades slightly, the order of magnitude of agreement shown in Table 2.2 is maintained.

2.5.3 Stability of Far Field Calculations

It remains to examine the stability of far field calculations in terms of the truncation limits Q and $M=N$. Using (2.32) and (2.35), we fixed the matrix size to 5x5 and varied the number of terms in the summation to obtain the monostatic far field data given in Table 2.3. These data comprise the magnitude and phase of $E_z^s(r;\phi)/E_z^i$ following normalization to remove range dependence. Table 2.3 shows that the stability of far field calculations increases with increase in the number

---

*Of course, the analytic continuity of the transverse components E_z and H_ϕ is implicit in (2.22) and (2.23) respectively; an explicit proof is obtained by multiplying each equation by $\sin\left[\frac{m}{\nu}(\phi-\alpha)\right]$ and integrating over ϕ from α to $2\pi-\alpha$ to obtain an identity. Similar treatment of the radial component H_r does not result in an identity; rather, one obtains a restatement of the fact that the tangential electric field at the join $(r=R, \phi=\alpha)$ is zero!

Table 2.2

CONTINUITY OF ELECTRIC FIELD ACROSS THE MATCHING BOUNDARY. $\alpha = \pi/4$, ka = 1, $\phi_o = \pi/2$, M = 5, Q = 65

ϕ_M^o	REAL $\left(\frac{E_z^I(R,\phi_M)}{E_z^i}\right)$	REAL $\left(\frac{E_z^{II}(R,\phi_M)}{E_z^i}\right)$	IMAGINARY $\left(\frac{E_z^I(R,\phi_M)}{E_z^i}\right)$	IMAGINARY $\left(\frac{E_z^{II}(R,\phi_M)}{E_z^i}\right)$
45	-0.0001908	0.0005345	0.0000000	0.000000
55	-0.1271333	-0.1264093	0.2889495	0.28831743
65	-0.2485921	-0.2489946	0.5429400	0.5431864
75	-0.3729855	-0.3736034	0.7593767	0.7587016
85	-0.5017511	-0.5021581	0.9324324	0.9328842
95	-0.6317953	-0.6319129	1.054209	1.054240
105	-0.7578067	-0.7570847	1.124976	1.124710
115	-0.8740709	-0.8743460	1.151982	1.151686
125	-0.9754530	-0.9751712	1.145676	1.145926
135	-1.058188	-1.058444	1.116831	1.116928
145	-1.120884	-1.120523	1.076364	1.076588
155	-1.164701	-1.164268	1.035405	1.035737
165	-1.192122	-1.192104	1.003509	1.003530
175	-1.205305	-1.205690	0.9864700	0.9864849

Table 2.3

STABILITY OF SCATTERED ELECTRIC FIELD AS A FUNCTION OF TRUNCATION LIMIT ON q SUMMATION.

$\alpha = \pi/4$, ka = 1, M = 5

		$\frac{E_z^s(r,\phi)}{E_z^i}$ normalized	
$\phi_o = \phi^o$	Q	AMPLITUDE	PHASE (radians)
75	25	0.04165533	0.3268
	35	0.04620371	0.2647
	45	0.04529889	0.2720
	55	0.04527489	0.2721
	65	0.04527684	0.2719
110	25	0.5254542	-0.3244
	35	0.5282959	-0.3146
	45	0.5255324	-0.3242
	55	0.5253510	-0.3237
	65	0.5254143	-0.3236
145	25	3.748533	2.2042
	35	3.754935	2.2041
	45	3.755965	2.2046
	55	3.756283	2.2045
	65	3.756194	2.2045
180	25	1.890126	1.9513
	35	1.892192	1.9526
	45	1.891032	1.9523
	55	1.890820	1.9523
	65	1.890914	1.9522

Table 2.4

STABILITY OF SCATTERED ELECTRIC FIELD AS A FUNCTION OF MATRIX SIZE M. $\alpha = \pi/4$, ka = 1, Q = 65

		$\frac{E_z^s(r,\phi)}{E_z^i}$ normalized	
$\phi_o = \phi^o$	M	CONDITION OF MATRIX	AMPLITUDE
75	3	10	0.04543635
	4	10^2	0.04527514
	5	10^3	0.04527684
	6	10^4	0.04525094
	7	10^5	0.04517362
110	3	10	0.5252016
	4	10^2	0.5253805
	5	10^3	0.5254143
	6	10^4	0.5252478
	7	10^5	0.5251775
145	3	10	3.756515
	4	10^2	3.756207
	5	10^3	3.756194
	6	10^4	3.756253
	7	10^5	3.756422
180	3	10	1.890504
	4	10^2	1.890908
	5	10^3	1.890914
	6	10^4	1.890994
	7	10^5	1.891326

of terms in the q summation, with discrepancies on the order of 10^{-5} or less for the larger of Q. The residual oscillations in calculated data can be traced to the oscillatory nature of the weighting functions I_1 and I_2 (see (2.26) and (2.27)). Finally, we choose $Q = 65$ terms and investigate the effect of varying the matrix size M. Referring to Table 2.4, a matrix size $M = 3$ (which correspond to six terms in the model description) appears to be too small for an accurate description of the scattering. On the other hand, a matrix size $M = 7$ introduces errors due to ill-conditioning of the system. Notice that results for $M = 4$, 5 and 6 show good correspondence; the scattering data are stable to at least the fourth decimal place, independent of aspect angle. From Tables 2.4 and 2.5 we see that the combination $Q = 65$, $M = 5$ appears optimum for the stated ka and α. Other combinations of wedge rounding ka and half-angle α led to maximum values $M = 10$ and $Q = 105$.

All the data presented in Tables 2.1 through 2.4 verify the internal consistency of calculations based upon the boundary value solution. Additional comments on the accuracy of calculations are presented in Section 2.8 and Chapter 4. External checks on computational accuracy are provided in Chapter 5.

2.6 Calculation of Backscattering

Although the analysis presented in Sections 2.3 and 2.4 allows calculation of fields for arbitrary angles of incidence and observation, in this section we confine results to the particularly important situation in which the transmitter and receiver occupy the same position. It is convenient to express (2.35) and (2.50) in the form

$$\frac{E^s(r,\varphi)}{E^i} \sim \frac{e^{-jkr+j\rho_V}}{\sqrt{2\pi kr}} F_V(ka,\varphi) \tag{2.52}$$

$$\frac{H^s(r,\varphi)}{H^i} \sim \frac{e^{-jkr+j\rho_H}}{\sqrt{2\pi kr}} F_H(ka,\varphi) \tag{2.53}$$

where ρ is the range-independent phase of the scattered field, $F(ka,\varphi)$ is the range-independent scattering pattern, and φ is the azimuth aspect angle referenced to a wedge face (i.e. $\varphi = \phi - \alpha$). The corresponding two-dimensional radar cross section is given by $F^2(ka,\varphi)/k$.

In Figs. 2.2 through 2.4 we present plots of principal polarization values of ρ and $F(ka,\varphi)$ vs. φ as a function of ka for 2α = 60°, 90° and 120°. Independent of polarization and wedge angle, increase in ka causes a decrease in pattern amplitude at aspects less than the specular value $0 \leq \varphi < \pi/2$, followed by an increase in pattern amplitude at aspects greater than the specular value ($\pi/2 < \varphi \leq \pi - \alpha$). This behaviour conforms with simple scattering arguments; in the former angular region, decrease is associated with replacing a discontinuous normal with a discontinuity in the derivative of the normal; in the latter interval increase results from a specular contribution. Phase data presented in radians are continuous except for a step of π radians occurring at $\varphi = \pi/2$ which originates in the singular behaviour of the asymptotic result for the sharp wedge.

For a given rounding, the extent of change in the sharp wedge result is dependent upon aspect angle, polarization and wedge angle. We examine the latter two dependencies at symmetrical incidence in terms of

that rounding required to double the sharp wedge magnitude, corresponding to a substantial 6dB enhancement in radar cross section.

Table 2.5
SYMMETRICAL INCIDENCE DATA

WEDGE ANGLE	ka for Doubling	
	VERTICAL POL.	HORIZONTAL POL.
60^o	2	0.8
90^o	3	1.5
120^o	> 4	4

Table 2.5 indicates higher sensitivity for horizontal polarization scattering with sensitivity for both polarizations increasing with decreasing wedge angle. Finally, we remark that the upper limits on ka in Figs. 2.2 through 2.4 represent a bound on present capability of aspect-dependent calculations. This bound signifies a cylindrical sector of arc length about 0.7 wavelengths. However, symmetrical incidence results can be obtained for ka as large as 7. From Fig. 2.3, the symmetrical incidence data for $ka = 3.0$ show minor polarization dependence, and the boundary value calculations thus extend into that region in which physical optics theory can have application.

2.7 Calculation of Bistatic Scattering

By allowing the transmitter and receiver to occupy different positions ($\phi_o \neq \phi$ in (2.35) and (2.36)) we may observe the bistatic dependence of the scattering pattern for a wedge with rounded edge. The bulk of the bistatic calculations are reported in Chapter 4 and we simply note here that all data satisfy reciprocity. Of present interest is the behaviour of fields propagated in the shadow region as a function of wedge rounding.

Fig. 2.5 depicts the shadow region when incidence is 30° from one wedge face. Incident energy is diffracted into the shadow region ($\varphi \geq 210°$) by a sharp wedge. When the wedge is rounded, creeping waves provide the coupling mechanism. According to results shown in Fig. 2.5, the strength of the shadow region pattern decreases with rounding independent of polarization and observation angle. While these data apply for a single incidence angle and rounding ka = 0, 1, the behaviour noted holds in all cases observed. We conclude that diffraction is the more efficient mechanism of coupling energy into the shadow region.

2.8 Scattering by a Cylindrically Tipped Wedge

In Sections 2.3 and 2.4, the first two terms in our solution for scattering by the wedge with rounded edge have been identified to be Karp's solution for the cylindrically tipped wedge[47] (see discussions following (2.34) and (2.49)). We now examine the latter solution to the extent that it affects the former analysis.

By designating region I to be conducting, Fig. 2.1 describes a wedge with cylindrical tip of radius R. Similarly, fields scattered by the cylindrically tipped wedge can be calculated from (2.35) and (2.50) upon setting $f_p = \alpha_p = F_p = D_p = 0$. Fig. 2.6 presents principal polarization magnitude data for a cylindrically tipped 90° wedge with $0 \leq kR \leq 4$. These data illustrate the extreme complexity of the scattering pattern as functions of monostatic aspect angle φ and tip radius R. Of specific interest is the appreciable enhancement over the sharp wedge result for large kR where $\varphi \sim 50°$ for vertical polarization, and when $\varphi \sim 0°$ for horizontal polarization. Due to the fact that the wedge with rounded edge causes reduction in the sharp wedge result at these angles (see Fig. 2.3),

appreciable cancellation occurs between the first two and third terms in (2.35) and (2.50). On the basis of magnitude alone, the numerical estimate of region I fields can suffer loss of more than one significant figure when $ka = 4$. Of course the cancellation process is complex so that loss of several significant figures is possible, and this situation is compounded as kR increases. Conversely, cancellation does not occur at the symmetrical aspect: here principal - polarization magnitudes are enhanced for both the cylindrically tipped and rounded wedges. This latter behaviour explains the extended numerical capability (ka as large as 7) demonstrated in Chapter 3 when boundary value calculations are limited to the symmetrical aspect.

Finally, we present analyses which will facilitate the comparison, in Chapter 3, of cylindrically tipped and rounded wedges with respect to the capability of approximate theory. According to the scattering center concept, the high-frequency description of scattering by a cylindrically tipped wedge consists of a specular return and creeping wave contributions. Fig. 2.7 depicts this approximation to the scattering phenomenon. In scattering pattern notation, we have the symmetrical incidence result

$$F(kR, \pi-\alpha) = \left| \sqrt{\pi kR}\left[1 + \frac{j}{2kR}\left(\frac{3}{8} \mp 1\right)\right] e^{-j\left(\frac{\pi}{4} - 2kR\right)} + 2\sqrt{\pi}(kR)^{1/3} e^{-j\frac{\pi}{4}} \sum_{m=0}^{4} C_m' \left\{ \hat{k} e^{-(\alpha m + jk)(\pi - 2\alpha)R} + \hat{k}^2 e^{-(\alpha_m + jk)(3\pi - 4\alpha)R} \right\} \right| \tag{2.54}$$

The first term in (2.54) in Imai's[53] asymptotic expansion of the exact solution for specular scattering by a cylinder where the upper and lower signs denote vertical and horizontal polarizations, respectively. The

second term in (2.54), which describes creeping waves, is obtained by appropriate modification of Kouyoumjian and Burnside's[54] analysis of bistatic scattering by a cylindrically tipped half plane. Here the coefficients C_m' and α_m are polarization dependent quantities specified by 2 m-dependent contants given in Ref. 54. Referring to Fig. 2.7, the first term is the contribution of that creeping wave which is launched at A, travels to the wedge face to undergo total reflection ($\mathcal{R} = \mp 1$), and then travels back to A where a portion of the wave is launched in the direction of the receiver. The second term in the series describes the contribution of that portion of the above creeping wave which travels past A to the opposite wedge face, is reflected again, and launched at B towards the source. The multiplier 2 in the second term accounts for the symmetrical pair of above creeping wave contributions.

Fig. 2.8 compares boundary value data with approximate results obtained by (2.54). Because of the oscillatory behaviour of F_H with change in kR, the symmetrical incidence return from the cylindrically tipped wedge remains sensitive to polarization over the complete range being investigated. Even so, excellent prediction capability is observed for both polarizations when $kR > 3$.

2.9 Comments

Calculations based upon the boundary value solution for the wedge with rounded edge are employed throughout the succeeding chapters, and the approach is specialized for a truncated wedge in Chapter 6.

The upper limit on the numerical capability for aspect-dependent calculations corresponds to an arc length of $0.75\ \lambda$. Investigation of the cylindrically tipped wedge leads us to suspect that this upper limit

is due to cancellation associated with the use of the circular-cylindrical matching boundary. It should be possible to increase numerical capability using a different approach which allows collapsing of the matching boundary to the virtual apex of the wedge.

Next consider Hunter's[46] application of the surface current replacement technique to the wedge with rounded edge. First, he uses a special modal representation of the surface current density which accelerates the convergence of numerical computations. Second, the size of only the cylindrical sector is limited by computational facilities. These features enable Hunter to extend his aspect-dependent calculations (which comprise investigation of scattering by a 94° wedge with rounded edge) to a maximum arc length of 1.1 λ.

In conclusion, we note that Hunter's results (see Chapter 4 of Ref. 46) involve the magnitude of the field scattered by a wedge with rounded edge. His data substantiate our findings in the case of the 90° wedge with rounded edge (see Fig. 2.3). Because our calculations are to be applied within the context of scattering center theory, we retain phase information as well.

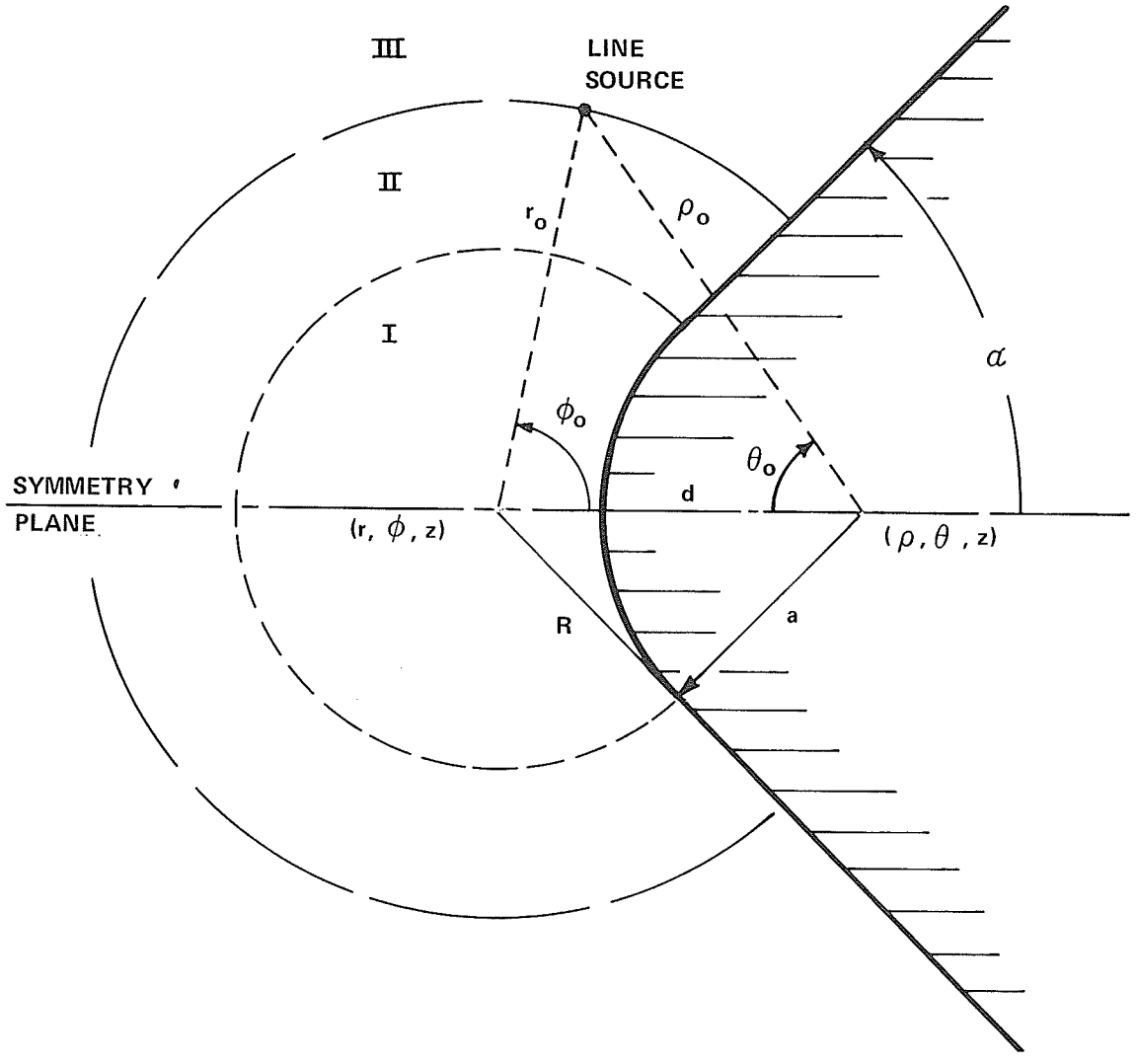

Figure 2.1 SCHEMATIC DIAGRAM OF WEDGE WITH ROUNDED EDGE UNDER LINE SOURCE EXCITATION

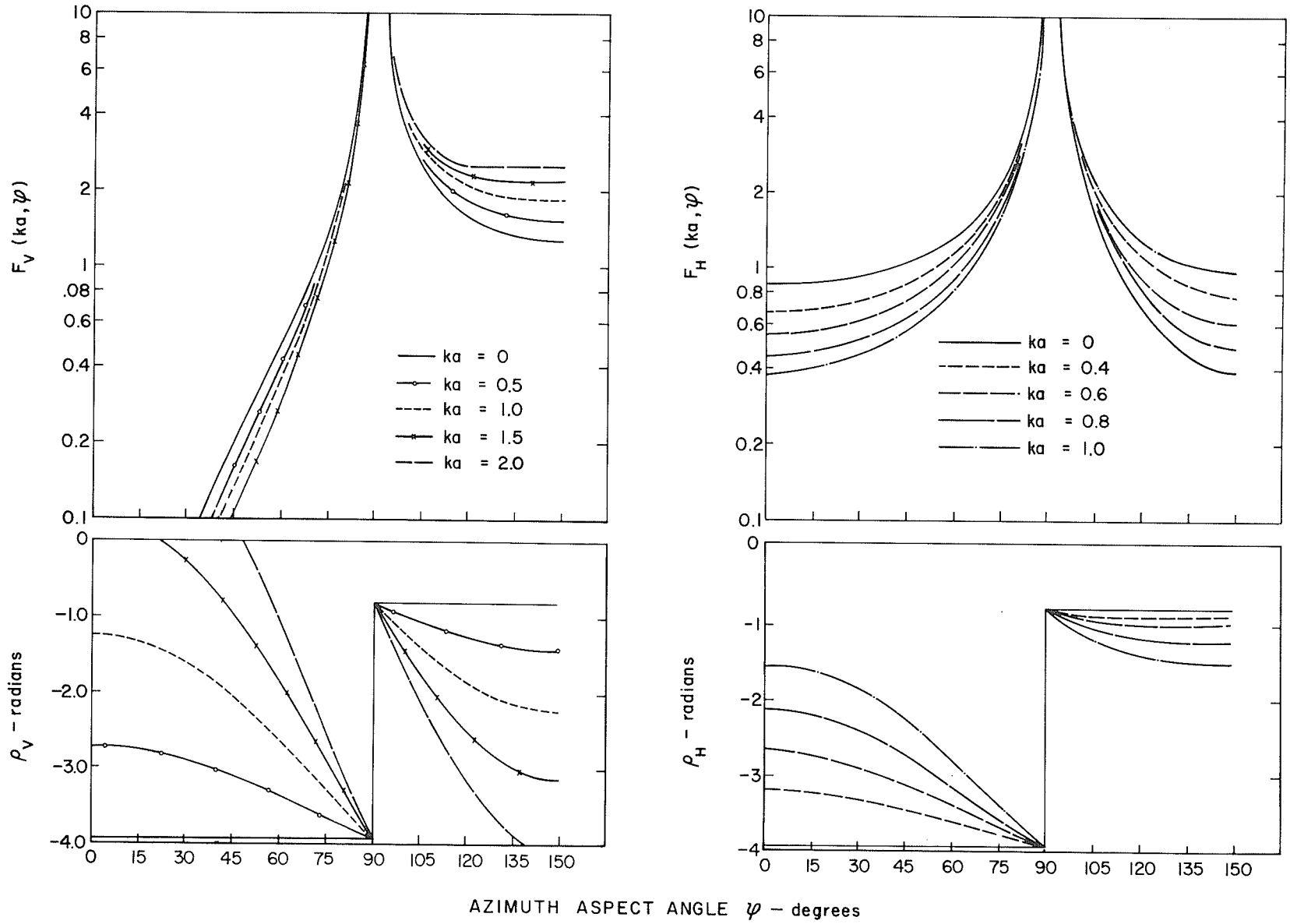

Figure 2.2 SCATTERING DATA FOR 60° WEDGE WITH ROUNDED EDGE. $0 \leqslant ka \leqslant 2.0$

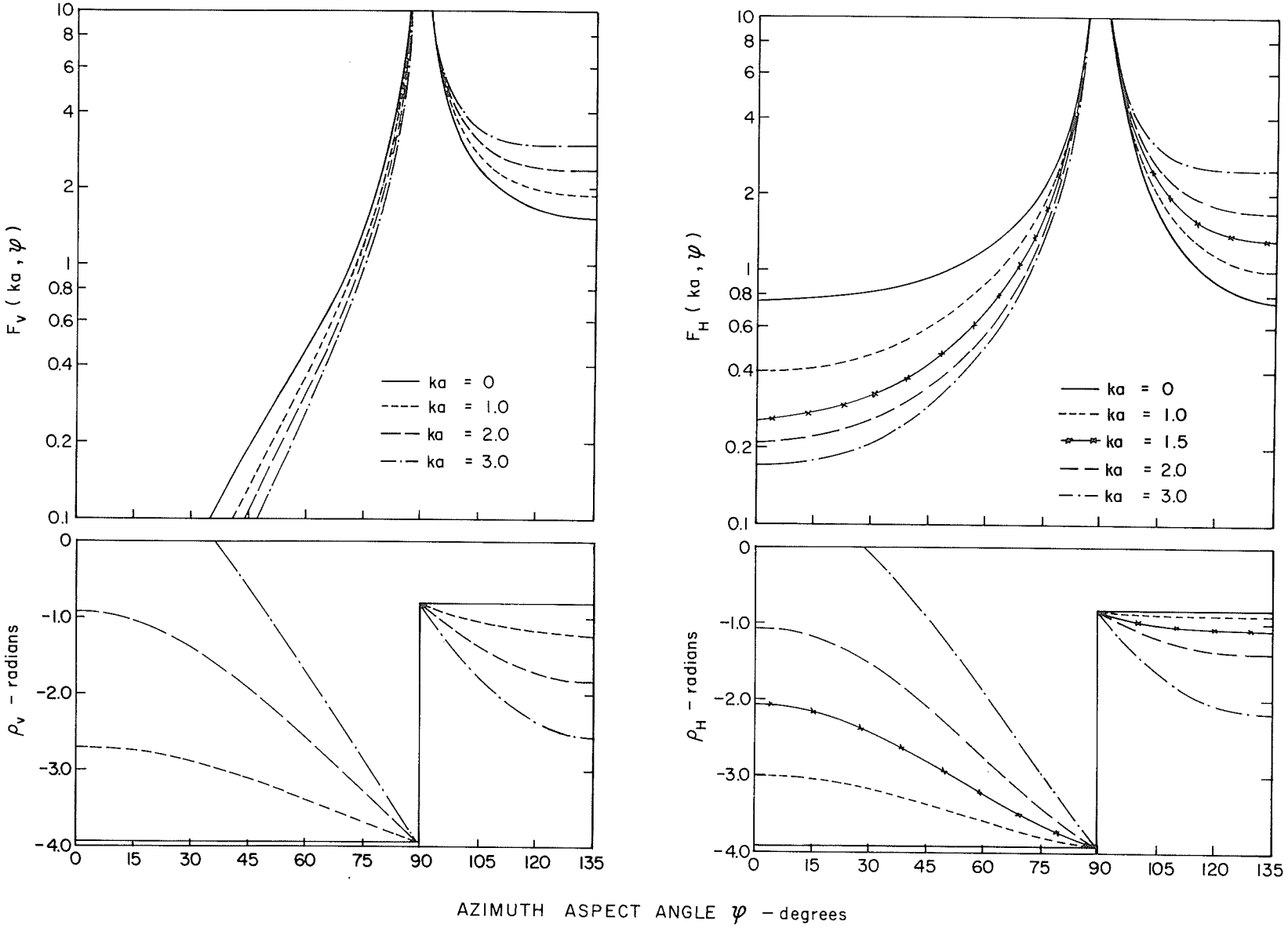

Figure 2.3 SCATTERING DATA FOR 90° WEDGE WITH ROUNDED EDGE. $0 \leqslant ka \leqslant 3.0$

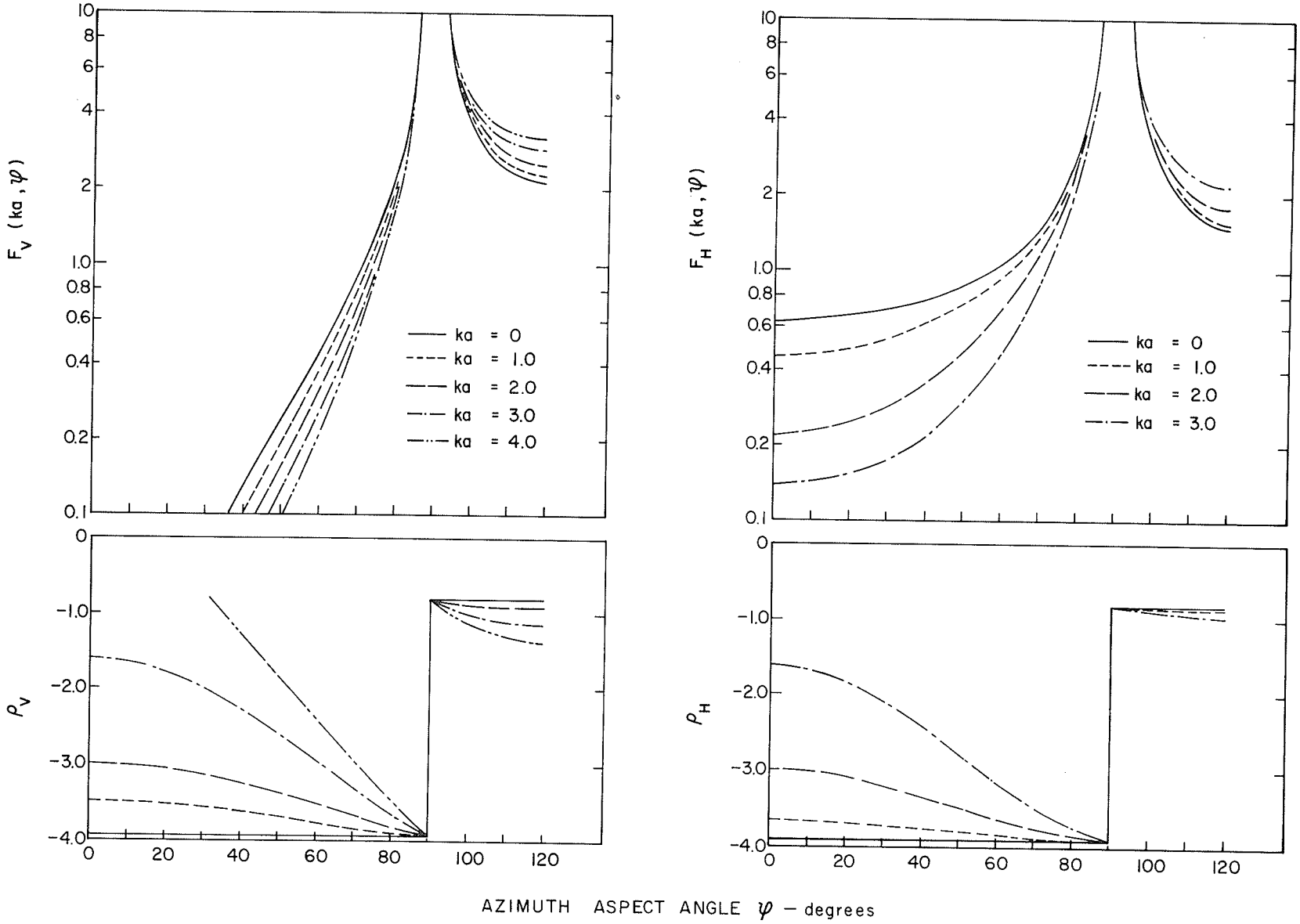

Figure 2.4 SCATTERING DATA FOR 120° WEDGE WITH ROUNDED EDGE. $0 \leqslant ka \leqslant 4.0$

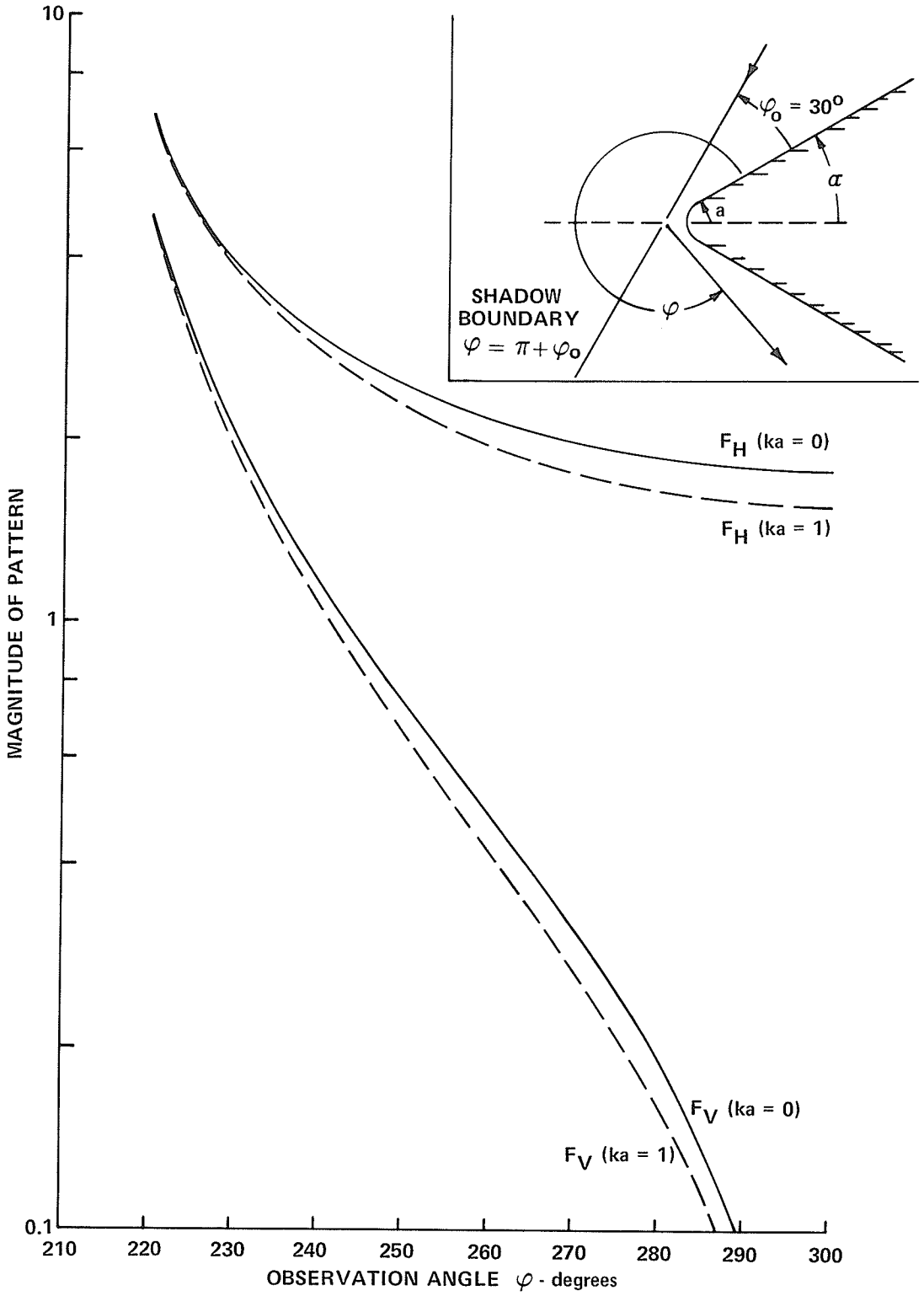

Figure 2.5 BISTATIC SCATTERING IN THE SHADOW REGION. $\varphi_o = 30^o$, $2\alpha = 60^o$, ka = 0, 1.

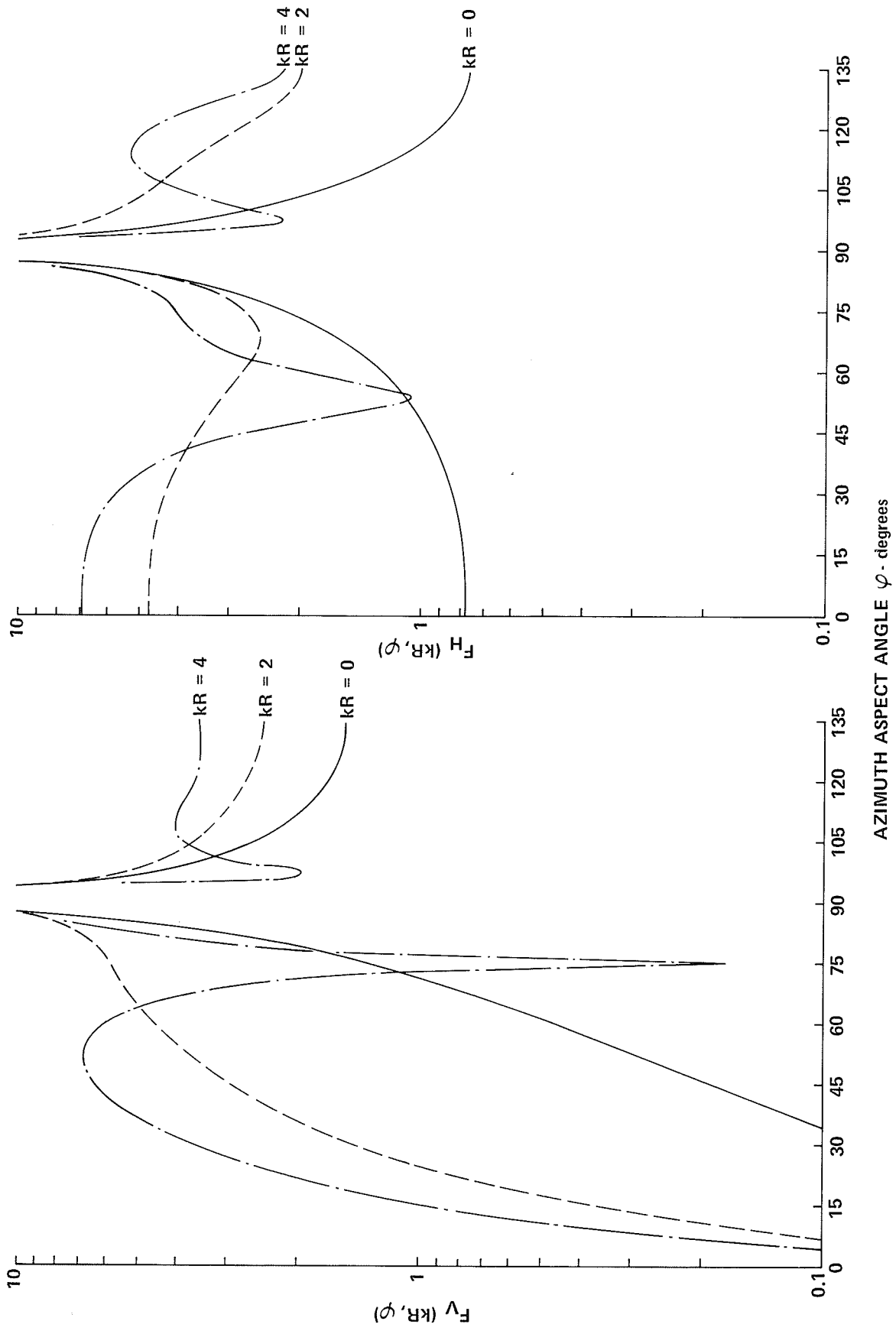

Figure 2.6 SCATTERING DATA FOR CYLINDRICALLY TIPPED 90° WEDGE. $0 \leqslant kR \leqslant 4$.

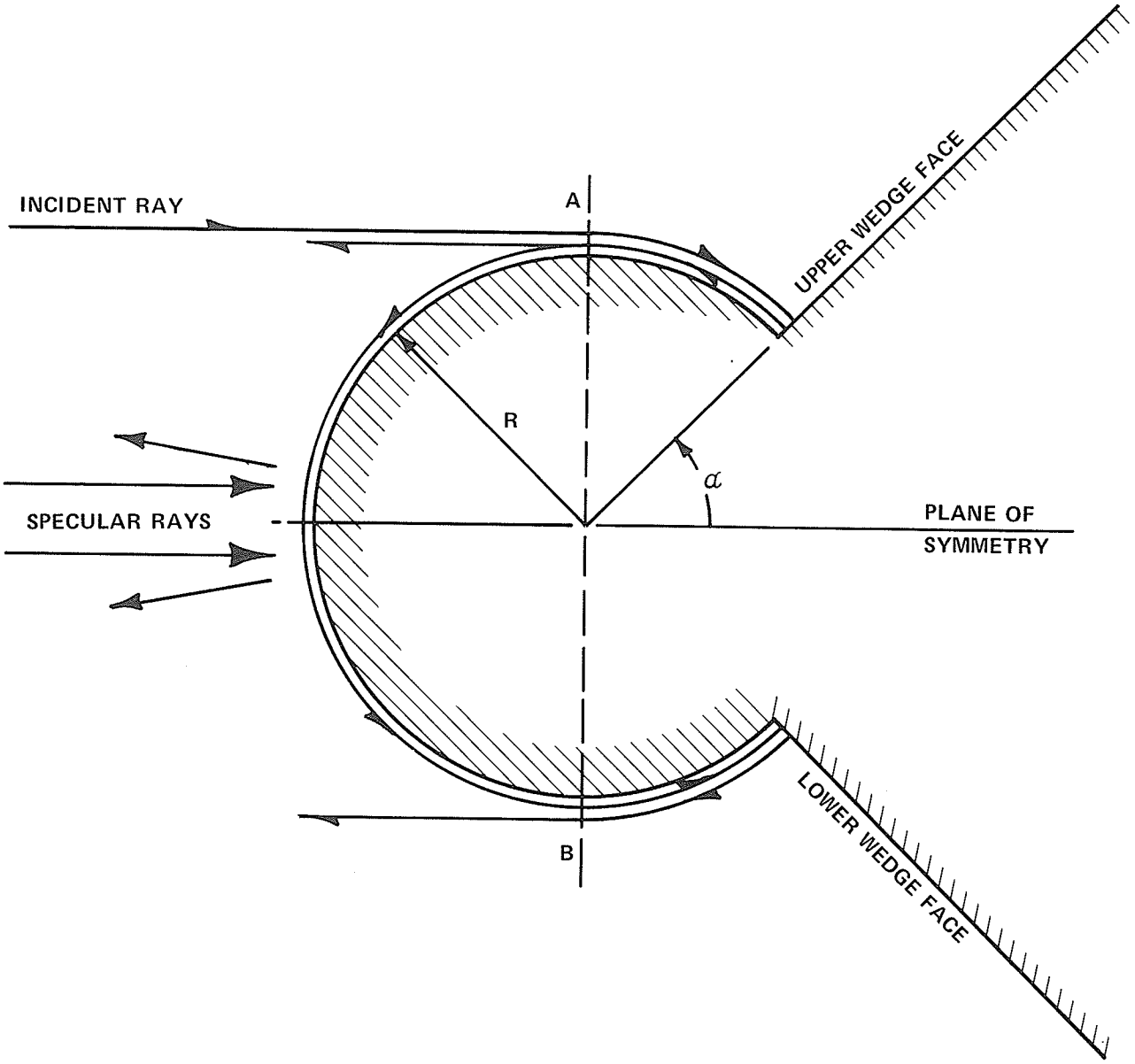

Figure 2.7 ONE SET OF RAYS SCATTERED BY A CYLINDRICALLY TIPPED WEDGE

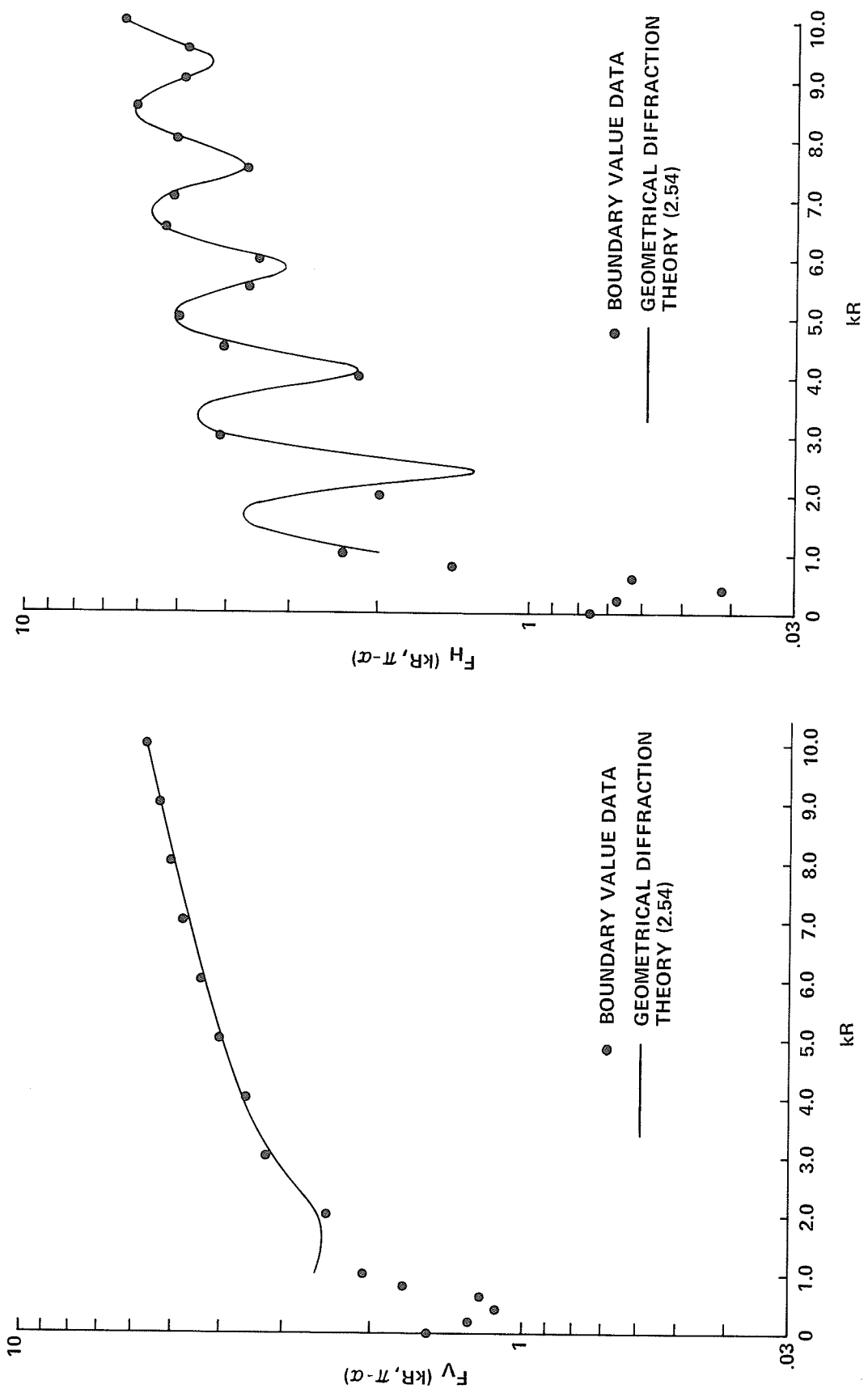

Figure 2.8 SYMMETRICAL-INCIDENCE SCATTERING BY A CYLINDRICALLY TIPPED 90^o WEDGE. $0 \ll kR \ll 10$.

3. ASYMPTOTIC PHYSICAL OPTICS

Undoubtedly the most common method for predicting scattering from conducting bodies is that based upon the physical optics approximation. In this chapter physical optics is applied to the wedge with rounded edge, a scatterer for which the method can have utility for large radii of curvature.

Certain fundamental limitations are inherent in the physical-optics method and these will be discussed in Section 3.1 where the two-dimensional formulation of conventional physical optics is presented. Section 3.2 introduces a simplification to physical optics which is ideally suited to the present investigation. Here the general physical optics integral, which requires numerical evaluation in conventional applications, is approximated at the outset by an asymptotic expansion. Because this simplification has not received prior exposure in the literature, asymptotic formulas are derived from conventional physical optics in this section. Asymptotic physical optics is applied to the wedge with rounded edge in Section 3.3. The major advantage in the present application lies in individual estimates of reradiation by all three scattering centers used in modeling the edge with large rounding (see Section 1.4). In fact, asymptotic physical optics is the only approximate theory which isolates a nonzero contribution from the join. Prediction capability is evaluated in Section 3.4 in comparison with boundary value calculations of Chapter 2. The chapter includes comment on the comparative utility of asymptotic and conventional physical optics in the present application.

3.1 Conventional Physical Optics

Physical optics arises from the radiation integral when one assumes that the surface current is the same at any point as it would be on an infinite plane tangent to the body at that point and assumes further the existence of a sharp shadow boundary, beyond which the surface current is identically zero. To the extent that the true current is well approximated by such an assumed current, the method is valid.

Certain fundamental limitations are inherent in the physical optics method. First, it must be recognized that physical optics, when applied to the backscattering case, always yields a scattered wave having the same polarization as the incident wave; no depolarization effects can be predicted, and the cross-polarization backscattering cross section computed by physical optics always vanishes. At best, physical optics seems to give a rough average of the vertical- and horizontal-polarization radar cross section. This polarization limitation on monostatic prediction is inherent in the "tangent plane" assumption for surface currents.

A further limitation of physical optics, when applied to bistatic situations, is that results do not conform to reciprocity (see, for example, Kouyoumjian[55]). Although the theory now exhibits polarization dependence, reciprocity is known to hold; therefore, the physical optics result must be incorrect.* For the special case of specular scattering, physical optics satisfies reciprocity and can be assumed to give reasonable results.

---

*Consequently, results such as those given by Siegel, et al[56], and by Weiner and Borison[48] must be regarded with considerable suspicion.

The above polarization and bistatic restrictions determine the scope of the present application of physical optics: our investigation concerns monostatic scattering by a wedge with large rounding for aspects which produce polarization-independent returns.

There are additional limitations on the theory which do not affect the present investigation. Physical optics fails to account for effects occurring in the geometrical shadow region: recall that the body is assumed to consist of the actual body plus its geometrical shadow. Experimental studies have shown a 10 dB change in radar cross section due to placing small obstacles deep in the shadow region (for the right-circular cone, see Olte and Silver;[57] for the sphere-capped cone, see Knott and Senior[58]). Physical optics cannot predict the effects of such obstacles. Finally, the physical optics approximation is poorest at just those parts of the surface (sharp discontinuities) that are most important in determining the scattering characteristics of finite, edgy targets.

In view of the limitations that must lead to very large inaccuracies when the radar cross sections of some bodies are computed, one might ask why physical optics is used at all. In fact, physical optics produces excellent results in some cases in which the actual surface currents are not much different from the assumed currents. Furthermore, it is generally possible to tell in advance for which cases these excellent results can be obtained. The major advantage of physical optics is that the method is relatively easy to formulate. The derivation of basic physical optics formulas for arbitrarily shaped perfectly conducting, three-dimensional bodies is given in several references.[35,59,60] For the two-dimensional case, it can be shown that physical optics gives

$$\sigma_{2K} \underset{\lim r \to \infty}{=} 2\pi r \left| \frac{e^{-j2kr}}{\sqrt{2\pi kr}} g(k) \right|^2 \tag{3.1}$$

$$g(k) = k e^{-j\frac{3\pi}{4}} \int_{\mathcal{C}} e^{-j2kz} \frac{d\ell}{dz} dz \tag{3.2}$$

where z = coordinate along the radar line of sight

ℓ = chord of intercept of target with plane perpendicular to the line of sight at point z (i.e., $\ell = \ell(z)$).

In the definition of radar cross section by (3.1), the subscript $2K$ denotes two-dimensional or length-dependent cross section, estimated according to the physical optics or Kirchhoff approximation. The function $g(k)$ is a partial transfer function between the scattered and incident magnetic field and it is written to show explicit dependence on the wave number k . In (3.2), $\mathcal{C}$ denotes a contour integration to be carried out over the (geometrically) illuminated portion of the body profile. Notice that $d\ell/dz$ represents the change in body chord as projected on a plane perpendicular to the radar line of sight: this quantity is the assumed distribution of current on the body. Finally, (3.1) and (3.2) represent the familiar physical optics estimate for monostatic scattering by a two-dimensional body where $e^{j\omega t}$ time dependence has been suppressed.

It is seldom that the integral in (3.2) can be evaluated in closed form. Then numerical evaluation is facilitated by performing the integration in piecewise fashion over the illuminated portion of the body. We define a new function:

$$g(k) = k e^{-j\frac{3\pi}{4}} \sum_{m=1}^{M} \int_{z_m}^{z_{m+1}} e^{-j2kz} \frac{dL_m}{dz}\, dz \qquad (3.3)$$

where the factor $\frac{dL_m}{dz}$ represents the function $\frac{dL}{dz}$ in the m^{th} region of integration. The validity of (3.3) follows from the definition of an integral. By breaking up the range of integration, we are frequently enabled to perform the integration over a complex profile as the sum of integrals over more simple surfaces. When each of these profiles is analytic, the exact physical optics transfer function is obtained.

3.2 Asymptotic Physical Optics

To gain further insight into the physical optics approximation as well as to see how best to apply it to the wedge with rounded edge, let us now consider the asymptotic-physical-optics approximation. This technique was originated by Geller[61] in 1954. It fell into disuse until 1960, when Bechtel[62] extended it to include phase information and applied it to three-dimensional targets. The latter analysis is followed below in developing the corresponding two-dimensional formulation.

Consider the integrals in (3.3) above. For physical optics to apply, the wavelength must be short, so that the wave number k is large. The integrals are then Fourier integrals of the form

$$\int_{t_1}^{t_2} e^{+jxt}\, \bar{\phi}(t)\, dt \qquad (3.4)$$

with x a large real parameter (equal to $-2k$) and t_1, t_2 a real interval. The function $\bar{\phi}(t)$ is assumed to be an integrable function so that the integral exists. If $\bar{\phi}(t)$ is N times continuously differentiable for $t_1 \le t \le t_2$ the integral can be expressed in an asymptotic form:

$$\int_{t_1}^{t_2} e^{jxt}\, \phi(t)\, dt = B_N(x) - A_N(x) + O(x^{-N}) \;; \quad x \to \infty \tag{3.5}$$

where

$$A_N = \sum_{n=0}^{N-1} j^{n-1}\, \phi^{(n)}(t_1)\, x^{-n-1}\, e^{jxt_1} \tag{3.6}$$

$$B_N = \sum_{n=0}^{N-1} j^{n-1}\, \phi^{(n)}(t_2)\, x^{-n-1}\, e^{jxt_2} \tag{3.7}$$

Here we have used the notation $\phi^{(n)}(t_1)$ for the n^{th} derivative of $\phi(t)$ with respect to t, evaluated at $t = t_1$. The expansion is a result of repeated integration by parts of the original integral; if $\phi^{(n)}(t_1)$ and $\phi^{(n)}(t_2)$ are zero for all $n > N$, the asymptotic series terminates and gives the exact result for any value of x, large or small. Interpreting physical optics in this manner, we see that backscattering arises at the end points: the phase angles that appear correspond to the location of the end points of the interval of integration. Other phase angles appear due to the term j^{n-1}, and they will produce a phase shift that depends upon the nature of the discontinuity (i.e., upon the real function $\phi(t)$).

Finally, we must consider a very important class of surface discontinuities: for these cases, there is a singularity of a particularly simple type at one end (or both ends) of the interval of integration. We have

$$\int_{t_1}^{t_2} e^{jxt}\, (t_2 - t)^{w-1}\, \phi(t)\, dt = B_N(x) + O(x^{-N}) \;, \quad x \to \infty \tag{3.8}$$

where

$$B_N = \sum_{n=0}^{N-1} \frac{\Gamma(n+u)}{n!} e^{j\frac{\pi}{2}(n-u)} \phi^{(n)}(t_2)\, x^{-n-u} e^{jxt_2} \tag{3.9}$$

provided that $\phi^{(n)}(t_1) = 0$ for $n = 0, 1, 2 \cdots N-1$ and $0 < u < 1$. Similarly, we have

$$\int_{t_1}^{t_2} e^{jxt} (t-t_1)^{v-1} \phi(t)\, dt = + A_N(x) + O(x^{-N}), \quad x \to \infty \tag{3.10}$$

where

$$A_N = -\sum_{n=0}^{N-1} \frac{\Gamma(n+v)}{n!} e^{j\frac{\pi}{2}(n+v-2)} \phi^{(n)}(t_1)\, x^{-n-v} e^{jxt_1} \tag{3.11}$$

provided that $\phi^{(n)}(t_2) = 0$ for $n = 0, 1, 2 \cdots N-1$ and $0 < v < 1$. Proofs of (3.9) and (3.11) are given by Erdelyi.[63] Although more general types of functions can be handled by similar techniques (for example, Erdelyi also considers singularities at both ends of the interval as well as singularities in the exponential factor), the formulas given above are sufficient for application of asymptotic physical optics to a wedge with rounded edge.

3.3 Asymptotic Physical Optics Applied to Wedge with Large Rounding

The application of asymptotic physical optics leads to expressions for the monostatic contributions from the three scattering centers required to model reradiation by a wedge with large rounding as shown in Appendix A. For convenience, we expand the physical optics transfer function as

$$g(k) = g(k)_s + g(k)_1 + g(k)_2 \tag{3.12}$$

where

$g(k)_s$ corresponds to the specular contribution from center S_s

$g(k)_1$ corresponds to the diffraction contribution due to the near join center S_{j_1}

$g(k)_2$ corresponds to the similar diffraction contribution due to the far join center S_{j2}

For a description of the scattering center model and the location of each center, see Fig. 1.1. Individual transfer functions are discussed below prior to their inclusion in the total formulation (3.12).

Specular Transfer Function

The contribution $g(k)_s$ is obtained from (3.8) and (3.9) where a singularity occurs at the lower end of the integration interval. From (A.12) we have the following two-term expansion

$$g(k)_s = \underset{0 \le \theta < \alpha}{\sqrt{\pi ka}} \left\{ 1 + \frac{j}{2ka} \left[3/8 \right] \cdots \right\} e^{j2ka\left(1 - \frac{\cos\theta}{\sin\alpha}\right)} \tag{3.13}$$

where θ is the monostatic aspect angle referenced to the symmetrical aspect and the phase center is chosen as the virtual apex of the wedge. The angular constraint on (3.13) implies that θ is small enough so that the location of the specular scattering center is sufficiently removed from the join.

It is interesting to compare the above result with Imai's[53] expansion of the exact solution for the large circular cylinder. In our notation, the specular term is

$$\sqrt{\pi ka} \left\{ 1 + \frac{j}{2ka} \left[3/8 \mp j \right] \cdots \right\} e^{j2ka\left(1 - \frac{\cos\theta}{\sin\alpha}\right)} \tag{3.14}$$

where the upper and lower signs denote the vertical and horizontal polarizations, respectively. It is evident that asymptotic physical optics provides the polarization independent portion of the first two terms in the series, which is the arithmetic mean of the principal polarization results.

Join Transfer Functions $g(k)_1$ and $g(k)_2$

The contribution $g(k)_1$ is obtained using (3.7). Since the normal is continuous at the join, $\phi^{(0)} = 0$, and diffraction arises due to $\phi^{(n)} \neq 0$; $n \geq 1$. From (A.21), the first two nonzero terms in the asymptotic series are

$$g(k)_1 = \left\{ \frac{1}{2} + \frac{3j \sin(\theta+\alpha)\cos(\theta+\alpha)}{4ka\cos^3(\theta+\alpha)} - - \right\} \frac{e^{-j\left[3\pi/4 + 2ka\left(\frac{\cos\theta}{\sin\alpha} - \sin(\theta+\alpha)\right)\right]}}{2ka\cos^3(\theta+\alpha)} \tag{3.15}$$

The corresponding join contribution from center S_2 is obtained from (3.15) by changing the sign of θ, i.e.,

$$g(k)_2 = \left\{ \frac{1}{2} + \frac{3j \sin(\alpha-\theta)\cos(\alpha-\theta)}{4ka\cos^3(\alpha-\theta)} - - \right\} \frac{e^{-j\left[3\pi/4 + 2ka\left(\frac{\cos\theta}{\sin\alpha} - \sin(\alpha-\theta)\right)\right]}}{2ka\cos^3(\alpha-\theta)}$$

$$; \ \theta < \alpha \tag{3.16}$$

$$= 0; \ \theta \geq \alpha$$

Join transfer functions have angular constraints which neglect interactions between scattering centers. Notice that the asymptotic series is in reciprocal powers of $ka\cos^3(\alpha \mp \theta)$. Such a product of dimensional and angular terms is common in high-frequency expansions. When it occurs, the region of validity of the series is determined by aspect angle as well as ka. To insure that additional terms in the series are negligible for appreciable rounding, we restrict investigations of validity to the

symmetrical incidence case($\theta=0$). Then $g(k)_1$ and $g(k)_2$ are equal and the total transfer function given by (3.12) becomes

$$g(k) = \sqrt{\pi ka}\left\{1 + \frac{j}{2ka}\left[\frac{3}{8}\right] - -\right\} e^{j2ka\left(1-\frac{1}{\sin\alpha}\right)} + \left\{1 + \frac{3j\sin\alpha\cos\alpha}{2ka\cos^3\alpha} - -\right\} \frac{e^{-j\left[3\pi/4 + 2ka\left(\frac{1}{\sin\alpha} - \sin\alpha\right)\right]}}{2ka\cos^3\alpha} \quad (3.17)$$

Using (3.17) in (3.1), we calculate the symmetrical incidence value of the two-dimensional radar cross section of a wedge with large rounding based upon asymptotic physical optics. The phase of the scattered signal ρ_K can be obtained directly from (3.17).

3.4 Evaluation of Asymptotic Physical Optics

Calculations based upon the analysis of Section 3.3 are compared with numerical results of the boundary value solution of Chapter 2. The format chosen for these latter data involves range-independent magnitude $F(ka,\varphi)$ and phase ρ of the scattered field for both principal polarizations, i.e.,

$$\frac{E^s(r,\varphi)}{E^i} = \frac{e^{-j2kr}}{\sqrt{2\pi kr}} F_V(ka,\varphi)\, e^{j\rho_V} \quad (3.18)$$

$$\frac{H^s(r,\varphi)}{H^i} = \frac{e^{-j2kr}}{\sqrt{2\pi kr}} F_H(ka,\varphi)\, e^{j\rho_H} \quad (3.19)$$

To compare data, we define a corresponding polarization-independent magnitude $G_K(ka,\theta)$ and phase ρ_K for asymptotic physical optics

$$g(k) = G_K(ka,\theta)\, e^{j\rho_K} \quad (3.20)$$

Then $G(ka, 0)$ is the symmetrical incidence prediction corresponding to $F_V(ka, \pi-\alpha)$, $F_H(ka, \pi-\alpha)$ and ρ_K is our estimate of ρ_V , ρ_H , respectively. Notice that evaluation of the prediction capability of asymptotic physical optics requires investigation of the magnitude and phase of the scattered field as both are necessary to any application of findings within the context of scattering center theory.

Fig. 3.1 compares approximate prediction with accurate data for a 90° wedge when the join contribution is neglected. Some correspondence between the magnitude of the specular component of asymptotic physical optics and the vertical-polarization boundary value result is observed for $1 < ka < 5$. However, polarization dependence of accurate data vanishes for $ka > 6$, and then $F_V = F_H \neq G_K$ (specular). It appears that the neglected join contribution must be approximately

i) polarization dependent for $ka < 5$

ii) polarization independent for $ka > 5$

Of course the specular representation of G_K will agree with F_V or F_H for very large rounding, but Fig. 3.1 shows that a nonzero joint return is necessary for $ka < 9$. Fig. 3.1 also shows that ρ_K (specular) accurately describes the ka dependence of ρ_V or ρ_H for $ka > 6$.

Fig. 3.2 allows evaluation of asymptotic theory, i.e., G_K , ρ_K are now calculated on the basis of both specular and join contributions. The magnitudes G_K and $F_V = F_H$ show excellent agreement for $ka \geq 5$, confirming that the asymptotic theory provides the proper polarization-independent join return for large ka . Prediction capability extends down to $ka = 3$ for the horizontal polarization case. For lower ka , the singularity in G_K associated with the asymptotic description of the join

return predominates. Phase data contained in Fig. 3.2 indicate that ρ_K is the mean of ρ_V and ρ_H for $ka \geq 3$. Specifically, approximate phase is accurate to within 12 degrees for $ka = 3$ and to within 6 degrees for $ka = 5$. As ka increases, ρ_K approaches ρ_V and ρ_H asymptotically.

The expression for $G_K \; e^{j\rho_K}$ includes a series in reciprocal powers of $ka \cos^3 \alpha$. For a given rounding, one can expect the accuracy of asymptotic physical optics to increase with decrease in wedge angle. Symmetrical incidence backscattering results for a 60° wedge are given in Fig. 3.3. Here G_K shows excellent agreement with F_H for $1 \leq ka \leq 2$; unfortunately, the limitation on numerical capability does not permit evaluation of approximate theory for larger rounding. Again, the predicted phase ρ_K is an average of ρ_V and ρ_H for $ka > 1.5$. Fig. 3.4 contains data corresponding to a 120° wedge. Here prediction capability requires roundings in excess of $ka = 8$.

It is of interest to examine modification of asymptotic physical optics to seek improvement upon the prediction capability demonstrated above. One obvious substitution is the asymptotic expansion of the exact solution for specular scattering (3.14) for the corresponding physical optics result (3.31). Imai's polarization-dependent result is compared with boundary value data for a 90° wedge in Fig. 3.5. However, no improvement upon the asymptotic physical optics specular result demonstrated in Fig. 3.1 is obtained. To complete the evaluation of modified physical optics, Imai's specular return is combined with the join return: Substituting (3.14) for (3.13) in (3.17), the results shown in Fig. 3.6 and 3.7 are obtained. Fig. 3.6 shows that the magnitude F_V is still poorly estimated when ka is so small the wedge return is polarization dependent, but that a better estimate of ρ_V now results (see Fig. 3.3).

Fig. 3.7 shows degraded prediction capability for F_H , but that phase estimation is considerably improved. One must conclude that, although phase predictions are more accurate, the overall utility of the modified expansion is not improved. Thus the inclusion of a polarization-dependent specular contribution will be warranted when a join contribution which is also sensitive to polarization is available.

3.5 Comments on Related Analysis

Hunter has investigated scattering by a wedge with rounded edge (see Chapter 4 of Ref. 46). His Figs. 4.7 through 4.18 show principal polarization magnitudes based upon the integral equation technique, conventional physical optics, and what is termed geometrical diffraction theory. As noted in Chapter 2, Hunter's predictions based upon exact electromagnetic theory confirm our results to within the accuracy of his data presentation. We now discuss his findings concerning conventional physical optics and geometrical diffraction theory.

Derivation of conventional physical optics formulas for both principal polarizations (see Sections 4.3(C) and 4.4(C) of Ref. 46) leads to integrals requiring numerical evaluation. Figs. 4.7 through 4.11 of Ref. 46 indicate that conventional physical optics has prediction capability in the gross sense for bistatic situations. This bears out our reticence to apply physical optics to the bistatic case. Hunter's use of conventional physical optics for symmetrical incidence backscattering is better founded. Figs. 4.12 through 4.17 of Ref. 46 show that the approximate theory underestimates the vertical polarization return, but overestimates the horizontal polarization return. Of course, the present accuracy of physical optics is within the asymptotic approximation, so

that Hunter's data confirm our findings for large rounding. This asymptotic relationship to conventional physical optics is illustrated in Fig. 3.8; for a right-angle wedge, little difference between physical optics and its asymptotic approximation exist for $ka > 5$. Notice that although conventional physical optics is finite for $ka = 0$, the prediction is only a rough average of the polarization-dependent boundary value calculations.

Figs. 4.7 through 4.18 of Ref. 46 also contain calculations based upon what is incorrectly called geometrical diffraction theory. Here Hunter has ignored the diffraction arising at the joins. Thus all of these data for the illuminated region are actually based upon geometric optics rather than geometrical diffraction theory. Only for data confined to the shadow region does his use of the term geometrical diffraction theory truly apply, and then the diffraction phenomenon involves only creeping wave contributions.

3.6 Conclusions

Asymptotic physical optics provides a straightforward technique for obtaining simple expressions which describe scattering by a wedge with rounded edge. Because the approach derives from conventional physical optics, its utility is limited by lack of polarization dependence. At the outset then, the theory can be expected to fail when obstacle scattering is known to be polarization dependent: This situation arises for a wedge with rounded edge when incidence is asymmetric; it also arises for symmetric incidence provided ka is not large.

In excess of expectations, asymptotic physical optics does provide prediction capability down to moderate roundings when wedge angle is not

extreme. For vertical polarization, the specular term alone shows reasonable agreement with boundary value calculations for $ka > 1$. For horizontal polarization, specular and join returns provide accurate estimates for $ka > 2$. For such large rounding that scattering becomes polarization-independent, the specular plus join formulation is in excellent agreement with boundary value calculations. When agreement between approximate and boundary value magnitudes exists, scattering phase is also accurately estimated. Thus asymptotic physical optics gives the necessary (but limited) analytical description of reradiation by the scattering center formed by a rounded edge. Unfortunately, the limitations (large rounding unless wedge angle is narrow and polarization is horizontal, symmetrical incidence only) limit practical application. Finally, modification of asymptotic physical optics in the light of known improved expressions does not allevaiate the above situation.

On the basis of the above findings, certain characteristics of the true join contribution are evident. The asymptotic estimate proportional to $(ka \cos^3\alpha)^{-1}$ is valid in the limit. For horizontal polarization, the first two terms in the asymptotic series are given by (3.15). For vertical polarization, asymptotic physical optics overestimates the true join return when rounding is moderate. These expressions represent the first evaluation of join returns performed to date.

Comparing boundary value calculations shown in Figs. 2.8 and 3.1, it is evident that the scattering mechanism for the cylindrically tipped wedge is a more complicated function of the modification radius. Also, applications of approximate scattering theory show better capability for the cylindrically tipped wedge. This situation illustrates an all too

frequent shortcoming in practical applications (i.e., the complexity of the scattering phenomena does not necessarily indicate the capability of existing approximate theory).

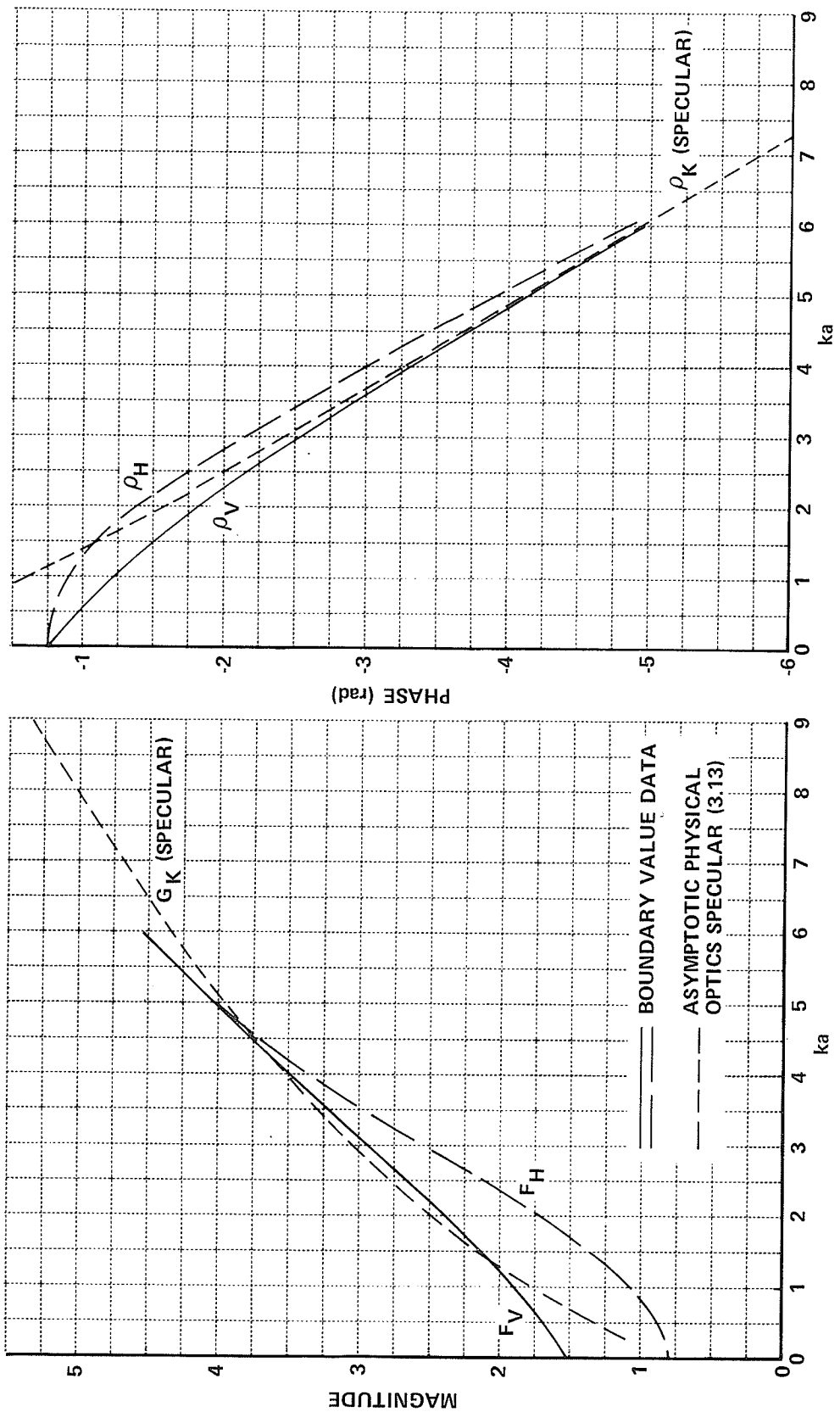

Figure 3.1 SYMMETRICAL-INCIDENCE BACKSCATTERING FROM A 90° WEDGE WITH ROUNDED EDGE. Specular Return.

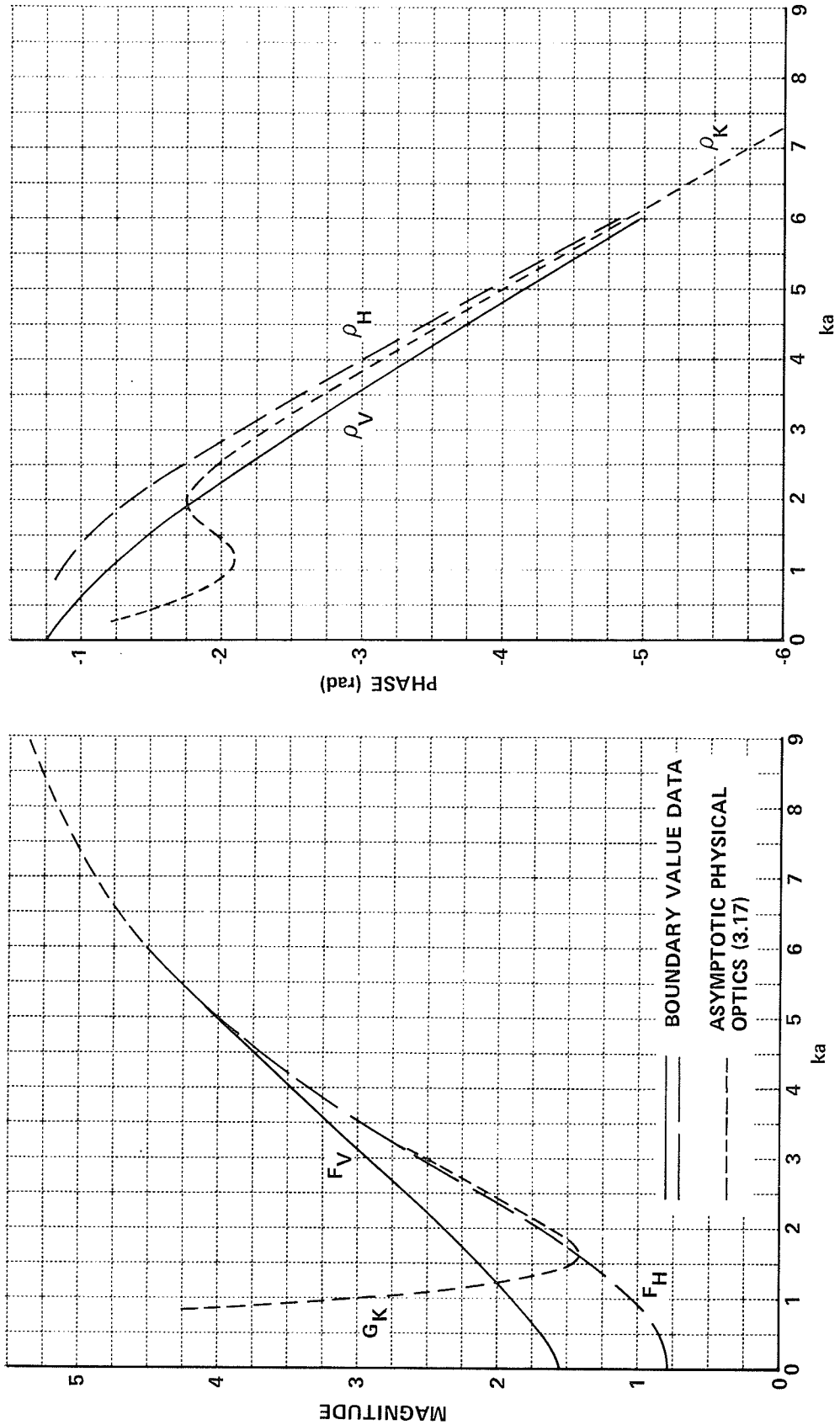

Figure 3.2 SYMMETRICAL-INCIDENCE BACKSCATTERING FROM A 90° WEDGE WITH ROUNDED EDGE. Specular Plus Join Returns.

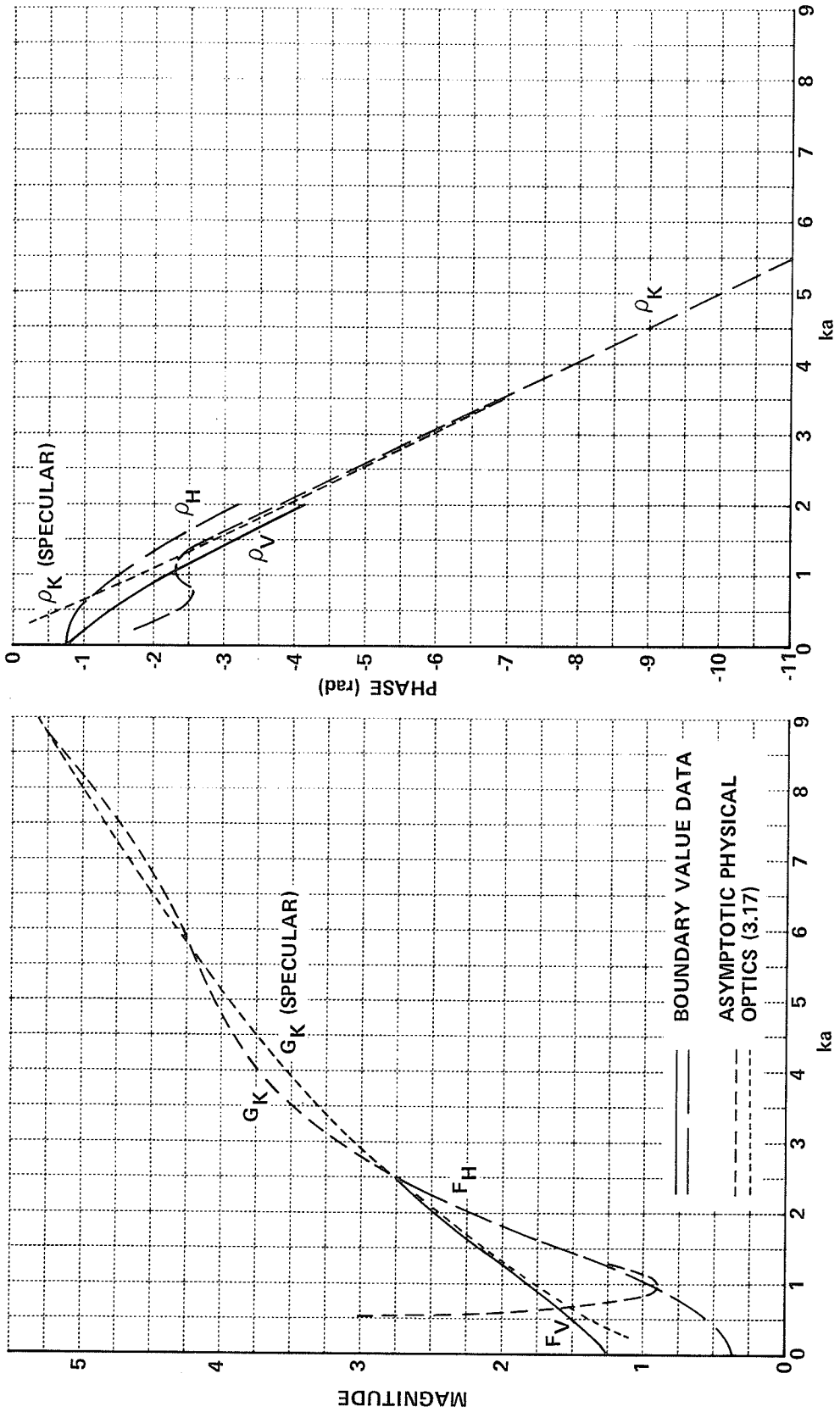

Figure 3.3 SYMMETRICAL-INCIDENCE BACKSCATTERING FROM A 60^o WEDGE WITH ROUNDED EDGE. Specular Plus Join Returns.

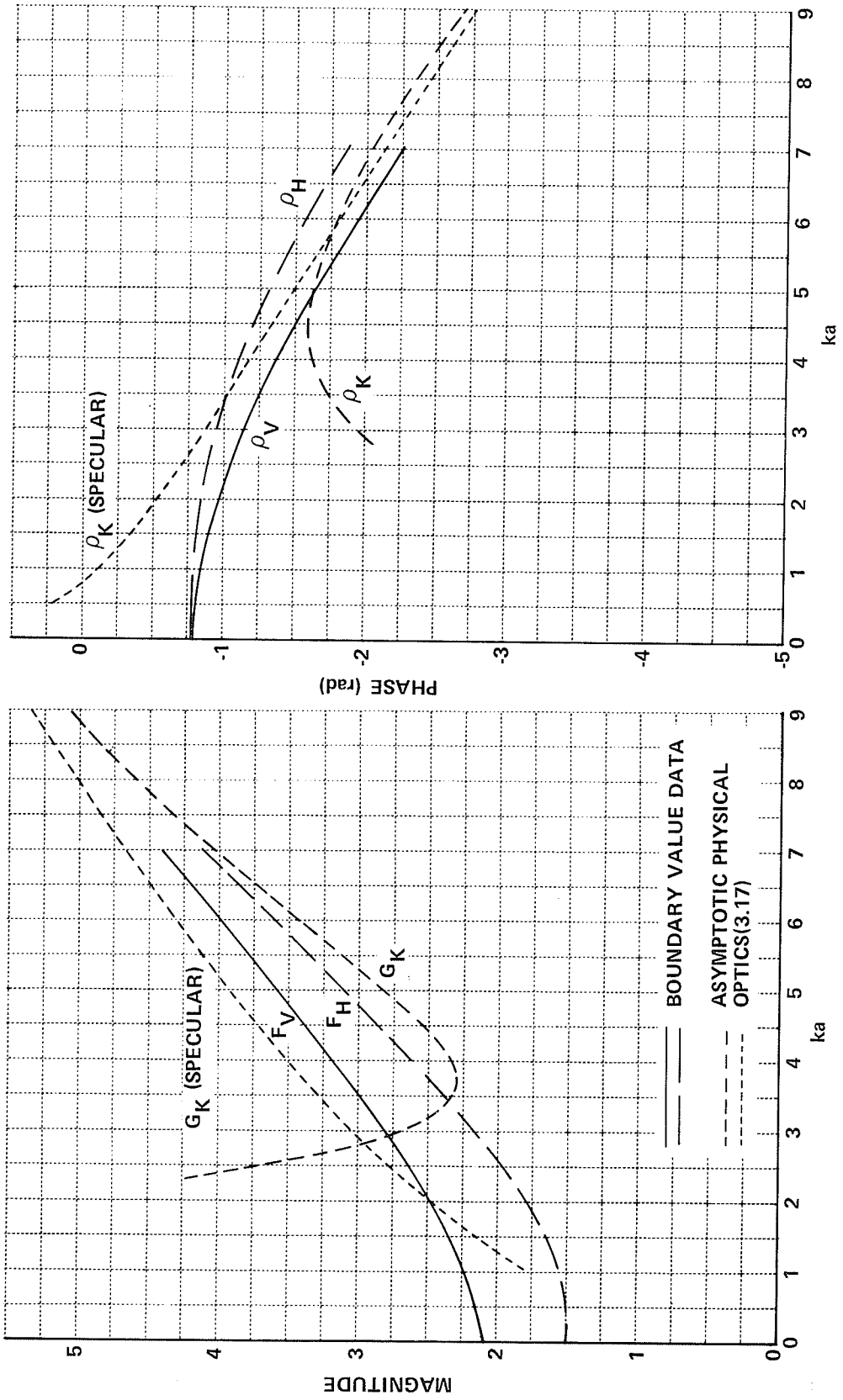

Figure 3.4 SYMMETRICAL-INCIDENCE BACKSCATTERING FROM A 120° WEDGE WITH ROUNDED EDGE. Specular Plus Join Returns.

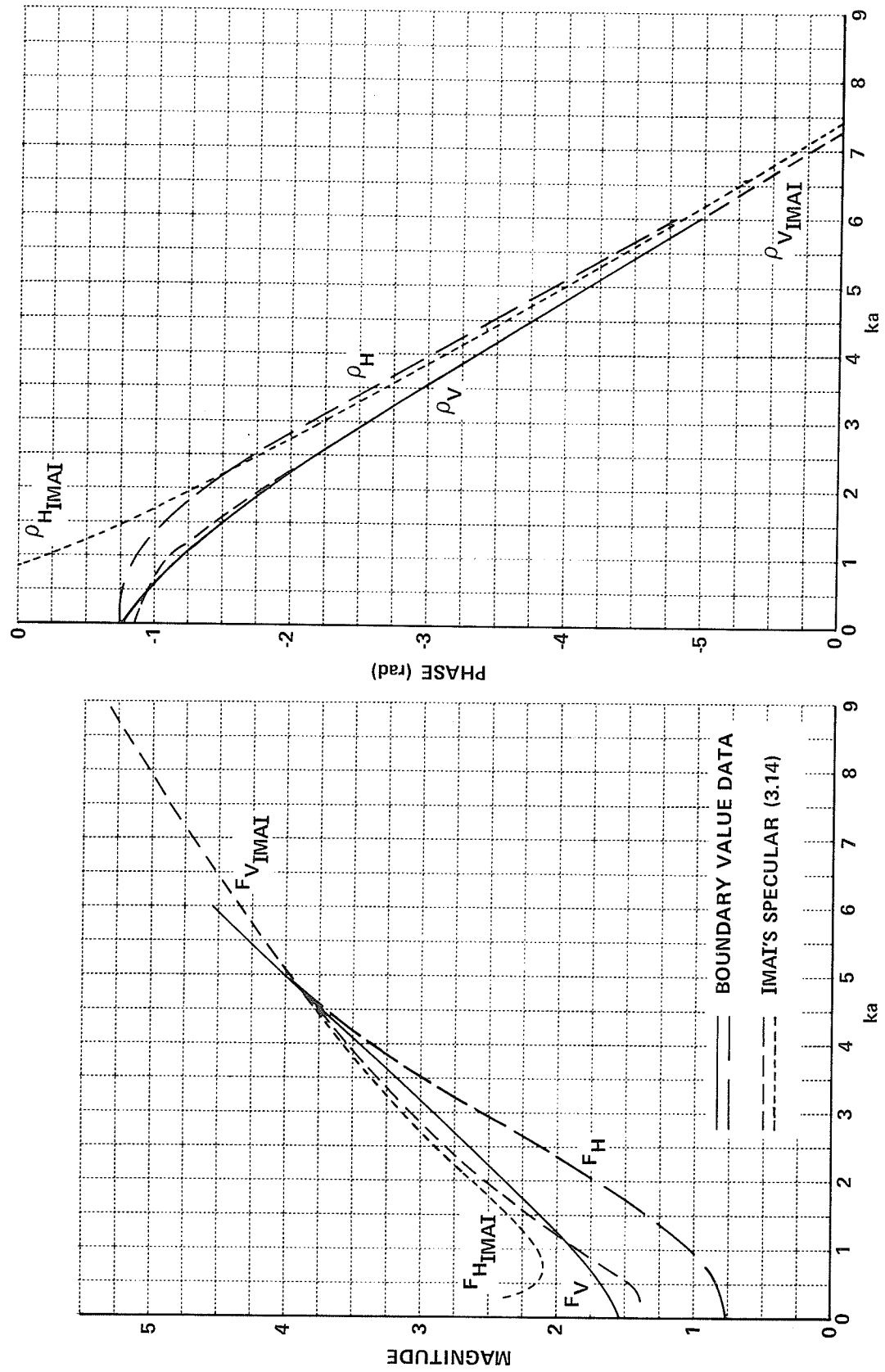

Figure 3.5 SYMMETRICAL-INCIDENCE BACKSCATTERING FROM A 90° WEDGE WITH ROUNDED EDGE. IMAI'S Specular Return.

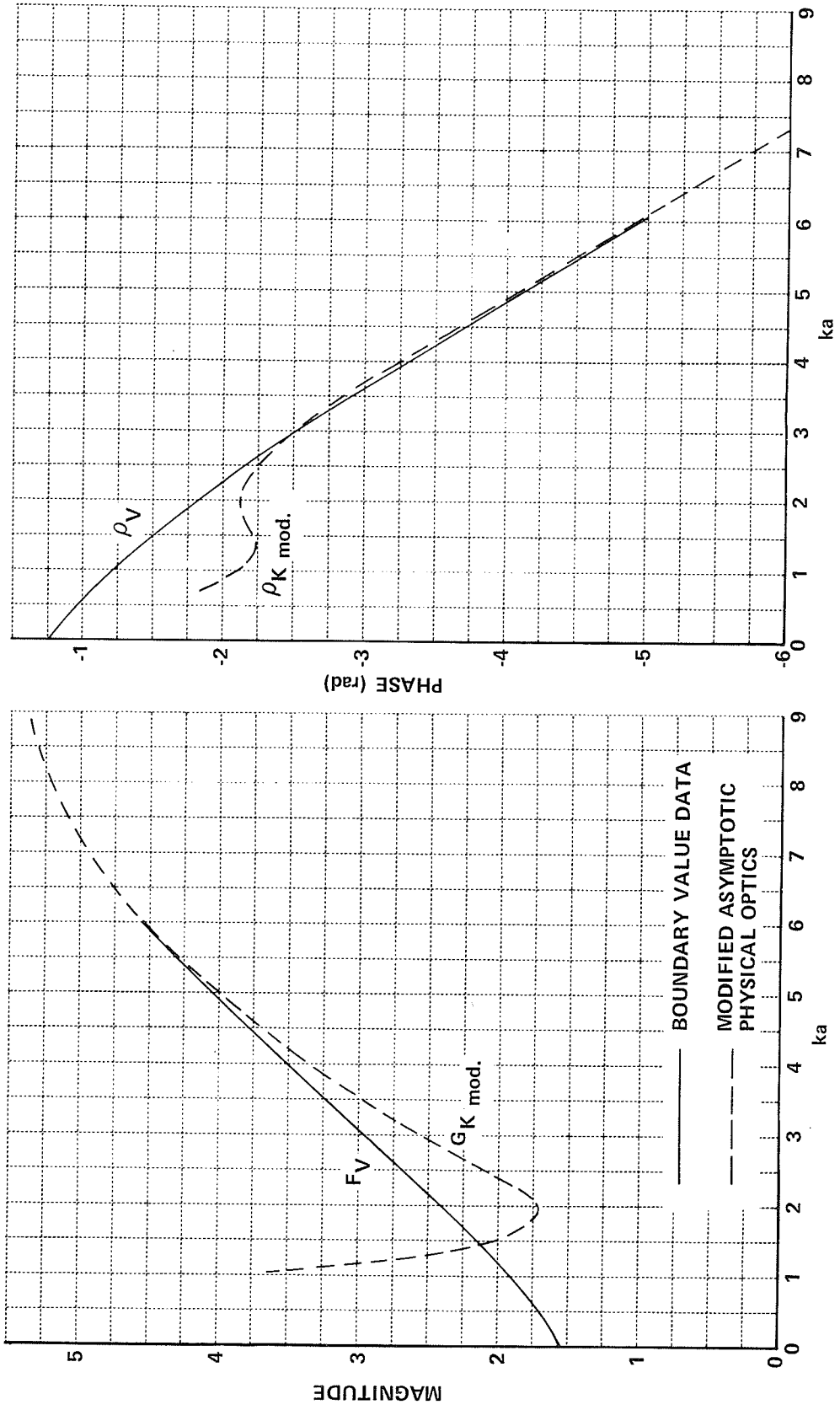

Figure 3.6 SYMMETRICAL-INCIDENCE BACKSCATTERING FROM A 90° WEDGE WITH ROUNDED EDGE AT VERTICAL POLARIZATION. IMAI'S Specular Plus Join Return.

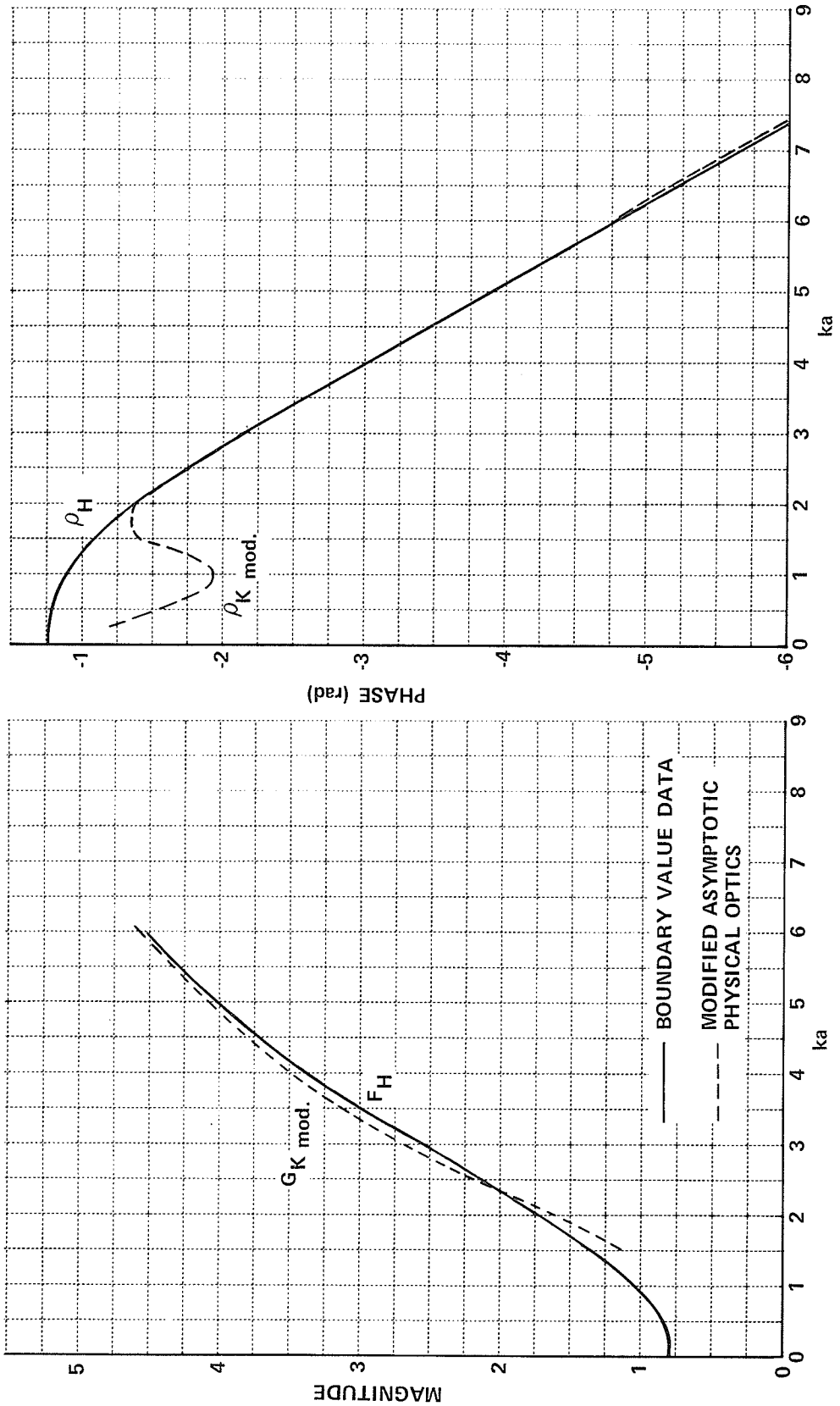

Figure 3.7 SYMMETRICAL-INCIDENCE BACKSCATTERING FROM A 90° WEDGE WITH ROUNDED EDGE AT HORIZONTAL POLARIZATION. IMAI'S Specular Plus Join Return.

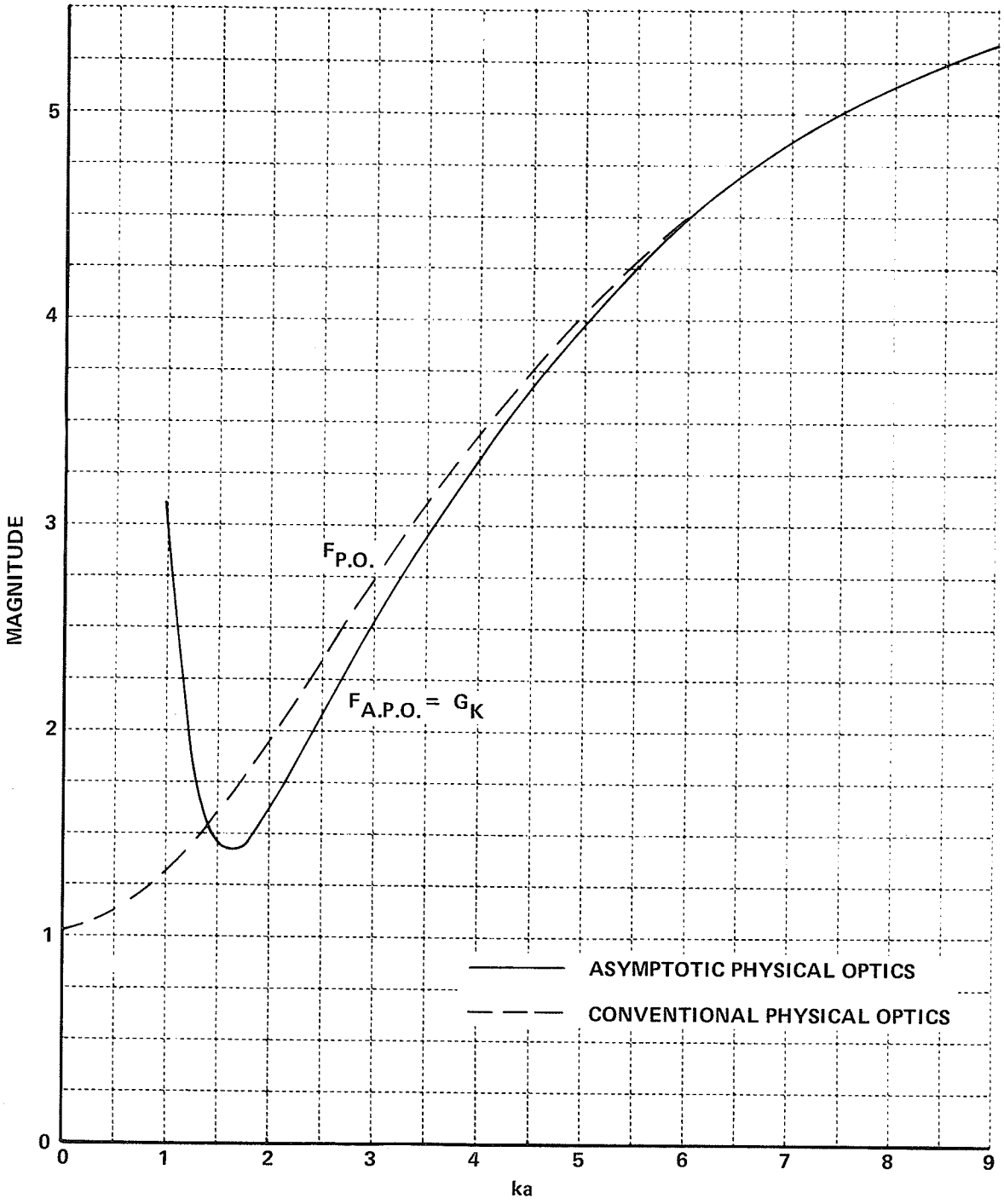

Figure 3.8 MAGNITUDE OF SYMMETRICAL-INCIDENCE BACKSCATTERING FROM A 90^{o} WEDGE WITH ROUNDED EDGE. Conventional and Asymptotic Physical Optics.

4. ANALYSIS OF PERTURBATION FIELDS

In this chapter the boundary value solution of Chapter 2 is viewed as the sharp wedge result plus a perturbation field which is due to rounding. Expressions are developed which accurately describe the monostatic and symmetrical-incidence bistatic angular dependence of perturbation fields, and these results are used in Chapter 5 to calculate scattering by targets with one or more rounded edges.

Plots of monostatic and bistatic perturbation patterns are presented in Section 4.1 for $ka \leq 1.0$. These perturbation data reveal simple angular dependence and compact expansions are empirically fit to both magnitude and phase in Section 4.2. Parametric dependencies of expansion coefficients are sought in Section 4.3. Section 4.4 contains comments on findings.

4.1 Perturbation Fields

For moderate values of ka, we view the solutions (2.35) and (2.51) as the sharp wedge result plus a perturbation, i.e.,

$$\frac{E^s(r,\varphi)}{E^i} \sim \frac{e^{-jkr}}{\sqrt{2\pi kr}} \left\{ \frac{\sin\frac{\pi}{\gamma}}{\gamma} \left[\frac{1}{\cos\frac{\pi}{\gamma} - \cos\left(\frac{\varphi+\varphi_o}{\gamma}\right)} - \frac{1}{\cos\frac{\pi}{\gamma} - \cos\left(\frac{\varphi-\varphi_o}{\gamma}\right)} \right] e^{-j\frac{\pi}{4}} + F_V^p e^{j\rho_V^p} \right\} \tag{4.1}$$

$$\frac{H^s(r,\varphi)}{H^i} \sim \frac{e^{-jkr}}{\sqrt{2\pi kr}} \left\{ \frac{\sin\frac{\pi}{\gamma}}{\gamma} \left[\frac{1}{\cos\frac{\pi}{\gamma} - \cos\left(\frac{\varphi+\varphi_o}{\gamma}\right)} + \frac{1}{\cos\frac{\pi}{\gamma} - \cos\left(\frac{\varphi-\varphi_o}{\gamma}\right)} \right] e^{-j\frac{\pi}{4}} + F_H^p e^{j\rho_H^p} \right\} \tag{4.2}$$

The first quantity in (4.1) and (4.2) is the leading term in the asymptotic series for the sharp wedge; this term alone accounts for the approximation indicated. Thus the expressions employed to calculate the magnitude F^p and phase ρ^p of the perturbation are exact.

Figs. 4.1 through 4.3 contain principal polarization plots of

perturbation patterns versus monostatic aspect angle for 60°, 90° and 120° wedges as a function of rounding in the range $0.2 \leq ka \leq 1.0$. Uniformly, the principal-polarization magnitudes F^{p} increase with increasing ka and decreasing wedge angle. With rounding fixed, halving the 120° wedge causes an order of magnitude increase in F_V^p and F_H^p. It is significant that the respective angular dependencies of F_V^p and F_H^p exhibit a definite character independent of wedge angle and ka (except in the horizontal polarization case when $ka > 0.8$ for the 60° wedge; these data are excluded from the following discussion). Specifically, F_V^p increases monotonically from zero at grazing to maximum value at the symmetrical aspect; F_H^p decreases from maximum at grazing to a (nonzero) minimum at symmetrical incidence. The often close correspondence between maxima in F_V^p and F_H^p is intriguing. Prior to discussing perturbation phase, we recall that the phase reference remains the virtual apex of the wedge. This partially accounts for increased variation in ρ_V^p with increasing ka and decreasing wedge angle. Although ρ_V^p has a characteristic angular dependence, no significance is attached to a common phase determined by wedge angle. Plots of ρ_H^p are limited to $ka = 0.2$, 0.6 and 1.0 for clarity: they indicate both relatively complex aspect dependence and instances when the variation in ρ_H^p increases with decreasing ka.

Figs. 4.4 through 4.6 present bistatic perturbation data when the rounded wedge is illuminated symmetrically ($\varphi_o = \pi - \alpha$). Results for 60° 90° and 120° wedges preserve the simple parametric behaviour noted with the monostatic perturbation data.

Next we examine corresponding perturbation results for a cylindrically tipped 90° wedge. Fig. 4.7 presents pattern amplitudes as a function of monostatic aspect angle for $0 \leq kR \leq 1$. Comparison of these data

with the rounded-wedge data in Fig. 4.2 shows that both the kR and aspect dependencies are more complicated while perturbation amplitude is increased by a factor greater than 4.

In summary, both monostatic and symmetrical-incidence bistatic perturbation fields for the rounded wedge exhibit relatively simple variation with change in aspect angle, wedge angle and rounding.

4.2 Empirical Fit to Perturbation Data

Both the monostatic and bistatic perturbation data presented in Figs. 4.1 through 4.6 suggest simple angular dependence. A form of aspect dependence can be inferred from periodicity and reciprocity considerations ions. In the far field, perturbation data can be assigned the aspect periodicity of fields scattered by a sharp wedge, i.e., $\frac{\varphi}{\gamma}$. Let us consider the (arbitrary) choice of expanding perturbation data in a power series in sin $(\frac{\varphi}{\gamma})$. Then reciprocity requires that the monostatic expansion include even powers of sin $(\frac{\varphi}{\gamma})$; similarly, the symmetrical-incidence bistatic expansion involves both even and odd powers of sin $(\frac{\varphi}{\gamma})$.

The aspect dependence of the monostatic perturbation data was assumed to be of the form

$$F^{p}(ka, \varphi=\varphi_0) = M_0 + M_1 \sin^2\left(\frac{\varphi}{\gamma}\right) + M_2 \sin^4\left(\frac{\varphi}{\gamma}\right) + M_3 \sin^6\left(\frac{\varphi}{\gamma}\right) + \text{-----} \qquad (4.3)$$

$$\rho^{p}(ka, \varphi=\varphi_0) = P_0 + P_1 \sin^2\left(\frac{\varphi}{\gamma}\right) + P_2 \sin^4\left(\frac{\varphi}{\gamma}\right) + P_3 \sin^6\left(\frac{\varphi}{\gamma}\right) + \text{-----} \qquad (4.4)$$

Estimates of the expansion coefficients M_i and P_i could be obtained by the method of least squares. When perturbation data have wide dynamic range, application of this technique artifically favors the higher-valued data

unless suitable weighting is introduced as compensation. A simple alternative, that of solving i simultaneous equations, was chosen which allowed uniform processing and provided an excellent fit to all perturbation data. Briefly, predictions based upon the empirical relations (4.3) and (4.4) are most in error when $2\alpha = 60°$ and $ka = 1$, but even then magnitudes are accurate to less than five percent and phase angles are correct to within one degree.

Tables 4.1 and 4.2 present the significant-amplitude coefficients M_i and P_i obtained by fitting vertical-polarization perturbation data with expansions truncated to three terms. Tables 4.3 and 4.4 apply for horizontal polarization; because these perturbation data are relatively complex, four-term expansions are necessary. Use of these tabulated coefficients in (4.1) and (4.2) facilitates aspect-dependent calculation of monostatic, principal-polarization scattering by 60°, 70°, 80°, 90° 100°, 110° and 120° wedges with ka = 0.2, 0.4, 0.6, 0.8 and 1.0.

In the symmetrical-incidence bistatic case, $\varphi_o = \pi - \alpha$ and $\sin(\frac{\varphi_o}{\gamma}) = 1$ so that the empirical relations corresponding to (4.3) and (4.4) become

$$F^p(ka, \phi_o = \pi-\alpha) = M_o + M_1 \sin\left(\frac{\varphi}{\gamma}\right) + M_2 \sin^2\left(\frac{\varphi}{\gamma}\right) + \cdots\cdots \tag{4.5}$$

$$\rho^p(ka, \varphi_o = \pi-\alpha) = P_o + P_1 \sin\left(\frac{\varphi}{\gamma}\right) + P_2 \sin^2\left(\frac{\varphi}{\gamma}\right) + \cdots\cdots \tag{4.6}$$

Tables 4.5 and 4.6 present the nonnegligible coefficients when the above bistatic expansions describe the vertical-polarization perturbation fields. Using (4.5) and (4.6) with Tables 4.5 and 4.6, we obtain bistatic predictions that are accurate to about two percent in magnitude and one degree in phase.

Table 4.1
EMPIRICAL FIT TO MAGNITUDE OF MONOSTATIC PERTURBATION FIELD. VERTICAL POLARIZATION

$$F_V^P = M_1 \sin^2\left(\frac{\varphi}{\gamma}\right) + M_2 \sin^4\left(\frac{\varphi}{\gamma}\right) + M_3 \sin^6\left(\frac{\varphi}{\gamma}\right)$$

	M_1	M_2	M_3		M_1	M_2	M_3
ka	60^o WEDGE				70^o WEDGE		
0.2	0.261	0.0276	-0.00128		0.174	0.0336	-0.0151
0.4	0.543	0.164	-0.0254		0.367	0.189	-0.0868
0.6	0.771	0.481	-0.125		0.521	0.527	-0.251
0.8	0.906	1.08	-0.358		0.614	1.084	-0.533
1.0	0.906	2.07	-0.847		0.623	1.978	-0.978
	80^o WEDGE				90^o WEDGE		
0.2	0.120	0.00609	0.00128		0.0782	0.00400	0.0
0.4	0.279	0.0395	0.0045		0.189	0.0230	0.00426
0.6	0.427	0.117	0.0070		0.303	0.0616	0.06746
0.8	0.563	0.245	0.00942		0.415	0.128	0.0160
1.0	0.672	0.439	0.00260		0.505	0.248	0.0160
	100^o WEDGE				110^o WEDGE		
0.2	0.0528	-0.0112	0.00978		0.0299	0.0	0.0
0.4	0.133	-0.0239	0.0274		0.0786	0.00524	0.000213
0.6	0.223	-0.0322	0.0527		0.136	0.0164	0.00112
0.8	0.316	-0.0311	0.0857		0.196	0.0366	0.00309
1.0	0.406	-0.0208	0.1292		0.255	0.0660	0.00786
	120^o WEDGE						
0.2	0.0167	0.0	0.0				
0.4	0.0464	0.00213	0.0				
0.6	0.0829	0.00728	0.00159				
0.8	0.1237	0.0147	0.00234				
1.0	0.165	0.0288	0.00437				

Table 4.2

EMPIRICAL FIT TO PHASE OF MONOSTATIC PERTURBATION FIELD. VERTICAL POLARIZATION

$$\rho_V^P = P_0 + P_1 \sin^2\left(\frac{\varphi}{\gamma}\right) + P_2 \sin^4\left(\frac{\varphi}{\gamma}\right)$$

	P_0	P_1	P_2		P_0	P_1	P_2
ka	60° WEDGE				70° WEDGE		
0.2	-1.865	-0.186	-0.008		-1.854	-0.196	-0.00218
0.4	-1.641	-0.631	-0.042		-1.692	-0.452	-0.0128
0.6	-1.410	-0.966	-0.112		-1.512	-0.720	-0.0445
0.8	-1.173	-1.555	-0.386		-1.319	-1.000	-0.0901
1.0	-0.944	-1.555	-0.386		-1.125	-1.271	-0.1555
	80° WEDGE				90° WEDGE		
0.2	-1.826	-0.126	-0.004		-1.779	-0.082	-0.002
0,4	-1.712	-0.292	-0.022		-1.698	-0.206	-0.005
0.6	-1.579	-0.490	-0.039		-1.603	-0.341	-0.020
0.8	-1.439	-0.679	-0.0817		-1.500	-0.487	-0.039
1.0	-1.294	-0.857	-0.148		-1.390	-0.630	-0.075
	100° WEDGE				110° WEDGE		
0.2	-1.720	-0.044	-0.006		-1.644	-0.031	0.0
0.4	-1.670	-0.106	-0.024		-1.612	-0.078	-0.003
0.6	-1.608	-0.188	-0.039		-1.569	-0.140	-0.005
0.8	-1.542	-0.262	-0.072		-1.527	-0.214	-0.010
1.0	-1.468	-0.345	-0.109		-1.463	-0.292	-0.015
	120° WEDGE						
0.2	-1.560	-0.017	0.0				
0.4	-1.541	-0.046	0.0				
0.6	-1.515	-0.087	0.0				
0.8	-1.437	-0.132	0.0				
1.0	-1.448	-0.176	-0.008				

Table 4.3

EMPIRICAL FIT TO MAGNITUDE OF MONOSTATIC PERTURBATION FIELD. HORIZONTAL POLARIZATION

$$F_H^P = M_0 + M_1 \sin^2\left(\frac{\varphi}{\gamma}\right) + M_2 \sin^4\left(\frac{\varphi}{\gamma}\right) + M_3 \sin^6\left(\frac{\varphi}{\gamma}\right)$$

	M_0	M_1	M_2	M_3	M_0	M_1	M_2	M_3
ka	60° WEDGE				70° WEDGE			
0.2	0.259	-0.206	-0.074	0.049	0.184	-0.146	-0.090	0.069
0.4	0.580	-0.339	-0.364	0.236	0.424	-0.258	-0.371	0.279
0.6	0.865	-0.251	-0.850	0.492	0.643	-0.197	-0.926	0.665
0.8	1.066	0.1609	-1.498	0.754	0.841	0.042	-1.540	1.082
1.0	1.175	0.920	-1.341	1.000	0.9953	0.191	-1.934	1.302
	80° WEDGE				90° WEDGE			
0.2	0.126	-0.107	-0.043	0.035	0.083	-0.072	-0.020	+0.017
0.4	0.297	-0.207	-0.149	0.110	0.206	-0.154	-0.070	+0.053
0.6	0.475	-0.252	-0.306	0.206	0.344	-0.216	-0.137	0.092
0.8	0.648	-0.214	-0.525	0.324	0.484	-0.234	-0.236	+0.142
1.0	0.797	-0.091	-0.756	+0.431	0.616	-0.335	-0.063	0.038
	100° WEDGE				110° WEDGE			
0.2	0.053	-0.048	-0.001	+0.002	0.032	-0.028	-0.004	0.004
0.4	0.139	-0.112	-0.017	0.013	0.089	-0.071	-0.015	0.013
0.6	0.240	-0.167	-0.050	0.032	0.159	-0.107	-0.047	0.032
0.8	0.348	-0.202	-0.097	0.054	0.239	-0.149	-0.064	0.040
1.0	0.457	-0.206	-0.165	0.083	0.322	-0.171	-0.099	+0.055
	120° WEDGE							
0.2	0.018	-0.016	-0.002	+0.002				
0.4	0.054	-0.043	-0.007	+0.006				
0.6	0.100	-0.073	-0.015	+0.012				
0.8	0.153	-0.101	-0.031	+0.020				
1.0	0.212	-0.125	-0.048	+0.028				

Table 4.4

EMPIRICAL FIT TO PHASE OF MONOSTATIC PERTURBATION FIELD. HORIZONTAL POLARIZATION

$$\rho_H^P = P_0 + P_1 \sin^2\left(\frac{\varphi}{\gamma}\right) + P_2 \sin^4\left(\frac{\varphi}{\gamma}\right) + P_3 \sin^6\left(\frac{\varphi}{\gamma}\right)$$

	P_0	P_1	P_2	P_3	P_0	P_1	P_2	P_3
ka	60^o WEDGE				70^o WEDGE			
0.2	-1.840	+0.241	-2.739	3.190	-1.825	+0.926	-5.165	5.145
0.4	-1.651	-0.055	-2.035	2.581	-1.664	+0.426	-3.436	3.746
0.6	-1.418	-0.451	-1.425	1.995	-1.479	-0.184	-1.889	2.412
0.8	-1.207	-0.804	-0.870	1.295	-1.316	-0.594	-0.873	1.403
1.0	-1.007	-1.040	-0.718	+0.882	-1.141	-0.921	-0.443	0.903
	80^o WEDGE				90^o WEDGE			
0.2	-1.778	+1.085	-5.379	5.332	-1.718	0.610	-3.261	3.604
0.4	-1.649	+0.494	-3.222	3.502	-1.620	0.324	-2.161	2.623
0.6	-1.519	+0.076	-2.042	2.476	-1.524	0.067	-1.253	1.800
0.8	-1.393	-0.204	-1.385	1.840	-1.425	-0.254	-0.75	1.425
1.0	-1.265	-0.446	-0.997	1.412	-1.325	-0.292	-0.614	1.118
	100^o WEDGE				110^o WEDGE			
0.2	-1.647	0.976	-4.110	+4.002	-1.565	0.380	-1.841	2.249
0.4	-1.572	0.662	-2.897	3.002	-1.506	0.274	-1.308	1.751
0.6	-1.498	0.420	-2.116	2.344	-1.451	0.188	-0.996	1.444
0.8	-1.424	0.229	-1.610	1.897	-1.397	0.093	-0.755	1.210
1.0	-1.349	+0.050	-1.231	1.552	-1.343	0.0117	-0.609	1.049
	120^o WEDGE							
0.2	-1.472	0.3978	-1.7293	2.0235				
0.4	-1.427	0.3089	-1.2251	1.5512				
0.6	-1.387	0.2379	-0.9382	1.2892				
0.8	-1.349	0.1711	-0.7344	1.0963				
1.0	-1.311	0.1099	-0.6003	0.9624				

Table 4.5

EMPIRICAL FIT TO MAGNITUDE OF SYMMETRICAL INCIDENCE PERTURBATION FIELD. VERTICAL POLARIZATION

$$F_v^p(ka, \varphi_o = \pi - \alpha) = M_4 \sin\left(\frac{\varphi}{\gamma}\right) + M_5 \sin^2\left(\frac{\varphi}{\gamma}\right)$$

	M_4	M_5		M_4	M_5
ka	60^o WEDGE			70^o WEDGE	
0.2	0.270	0.017		0.183	0.010
0.4	0.596	0.086		0.416	0.051
0.6	0.965	0.172		0.668	0.129
0.8	1.392	0.238		0.921	0.246
1.0	1.850	0.278		0.210	0.354
	80^o WEDGE			90^o WEDGE	
0.2	0.122	0.005		0.078	0.005
0.4	0.288	0.031		0.198	0.014
0.6	0.470	0.081		0.327	0.045
0.8	0.652	0.165		0.460	0.099
1.0	0.838	0.275		0.593	0.176
	100^o WEDGE			110^o WEDGE	
0.2	0.048	0.004		0.030	0.006
0.4	0.121	0.016		0.081	0.003
0.6	0.208	0.037		0.142	0.011
0.8	0.301	0.069		0.212	0.023
1.0	0.393	0.121		0.287	0.042
	120^o WEDGE				
0.2	0.0170	0.0			
0.4	0.0474	0.001			
0.6	0.086	0.004			
0.8	0.130	0.011			
1.0	0.178	0.021			

Table 4.6

EMPIRICAL FIT TO PHASE OF SYMMETRICAL INCIDENCE PERTURBATION FIELD. VERTICAL POLARIZATION

$$\rho_v^p(ka, \varphi_0 = \pi - \alpha) = P_4 + P_5 \sin\left(\frac{\varphi}{\gamma}\right) + P_6 \sin^2\left(\frac{\varphi}{\gamma}\right)$$

	P_4	P_5	P_6		P_4	P_5	P_6
ka	60^o WEDGE				70^o WEDGE		
0.2	-2.042	+0.001	-0.118		-1.987	-0.001	-0.074
0.4	-2.043	+0.007	-0.278		-1.978	0.002	-0.181
0.6	-2.040	+0.012	-0.460		-1.977	0.007	-0.307
0.8	-2.037	+0.025	-0.666		-1.975	0.012	-0.445
1.0	-2.031	+0.046	-0.896		-1.972	+0.064	-0.644
	80^o WEDGE				90^o WEDGE		
0.2	-1.909	+0.001	-0.048		-1.833	-0.002	-0.028
0.4	-1.909	+0.005	-0.122		-1.834	-0.001	-0.074
0.6	-1.909	+0.006	-0.205		-1.834	+0.002	-0.132
0.8	-1.908	+0.011	-0.303		-1.832	+0.001	-0.194
1.0	-1.906	+0.020	-0.414		-1.832	+0.007	-0.270
	100^o WEDGE				110^o WEDGE		
0.2	-1.753	+0.002	-0.019		-1.666	+0.001	-0.011
0.4	-1.754	+0.004	-0.050		-1.667	+0.001	-0.028
0.6	-1.754	0.0	-0.081		-1.664	+0.003	-0.054
0.8	-1.755	+0.004	-0.125		-1.663	+0.004	-0.082
1.0	-1.755	0.008	-0.175		-1.668	+0.027	-0.129
	120^o WEDGE						
0.2	-1.572	0.0	-0.002				
0.4	-1.573	0.0	-0.016				
0.6	-1.574	0.0	-0.024				
0.8	-1.574	+0.001	-0.042				
1.0	-1.574	+0.002	-0.060				

For comparison purposes, the suitability of an empirical fit to perturbation data for a cylindrically tipped wedge was investigated. An attempt to represent the monostatic results presented in Fig. 4.7 in the form of the expansion (4.3) led to the need for additional terms with considerable reduction in accuracy. Thus the perturbation data for the rounded wedge are better suited to an empirical fit than corresponding data for the cylindrically-tipped wedge.

4.3 Parametric Dependence of Coefficients

Determination of the ka and α dependence of the tabulated coefficients M_i and P_i is necessary to obtain an explicit analytical representation for perturbation fields. The worth of such closed-form approximations requires that we investigate the behaviour of these coefficients.

Although the specialized angular expansions (4.3) through (4.6) satisfy periodicity and reciprocity constraints, they represent but one of many possible forms. The proper form will satisfy the general bistatic case, and this form must be identified prior to meaningful investigation of the parametric dependence of the coefficients. In retrospect, certain of the sets of specialized coefficients listed in Tables 4.1 through 4.6 are suspect: i.e., instances occur where coefficient amplitude is non-monotonic in ka, and where the sign of the coefficient changes with wedge angle.

Consider the problem of constructing the general bistatic expansion which accurately fits the magnitudes of vertical-polarization perturbation data. We proceed by detailed examination of perturbation data for arbitrary choices of incidence and observation angles. These observations,

together with the requirement that the general bistatic form preserve the accuracy already demonstrated in specialized cases (monostatic and symmetrical-incidence bistatic) leads to the following form

$$F_v^p(ka,\varphi,\varphi_o) = G_1 \sin\left(\frac{\varphi}{\gamma}\right)\sin\left(\frac{\varphi_o}{\gamma}\right) + G_2 \sin^2\left(\frac{\varphi}{\gamma}\right)\sin^2\left(\frac{\varphi_o}{\gamma}\right)$$

$$+ G_3 \sin\left(\frac{\varphi}{\gamma}\right)\sin\left(\frac{\varphi_o}{\gamma}\right)\cos\left(\frac{\varphi}{\gamma}\right)\cos\left(\frac{\varphi_o}{\gamma}\right)$$

$$+ G_4 \sin^2\left(\frac{\varphi}{\gamma}\right)\sin^2\left(\frac{\varphi_o}{\gamma}\right)\cos\left(\frac{\varphi}{\gamma}\right)\cos\left(\frac{\varphi_o}{\gamma}\right) \qquad (4.7)$$

$$+ \text{-----}$$

Comparing (4.7) with the specialized expansions (4.3) and (4.5) we obtain the relation between coefficients

$$\begin{aligned} G_1 &= M_4 \\ G_2 &= M_5 \\ G_3 &= M_1 - M_4 \\ G_4 &= -M_3 \end{aligned} \qquad (4.8)$$

Evaluation of (4.7) and (4.8) for arbitrary combinations of φ and φ_o reveals good agreement with boundary value calculations. The error in estimating perturbation magnitude lies in the third decimal place provided $ka\cos\alpha \leq 0.7$. This accuracy is maintained for the maximum value $ka\cos\alpha = 0.866$ in the restricted bistatic interval $|\varphi,\varphi_o| \leq \pi-\alpha$. For $ka\cos\alpha > 0.7$ and larger bistatic angles, the general bistatic fit is poor, and accuracy is recovered by introducing a step-function attenuation of terms in G_3 and G_4 when $\varphi, \varphi_o > \pi-\alpha$. The modification noted implies that many additional terms are necessary in (4.7) to describe the general bistatic dependence of the magnitude of the perturbation field.

The substantial prediction capability of (4.7) indicates that we have identified the first four terms in the general bistatic expansion. It is now realistic to investigate the parametric dependence of $G_1 = M_4$, the dominant coefficient in (4.7). Using Table 4.5 we plot G_1 versus wedge angle as a function of rounding in Fig. 4.8.

Because the dominant coefficient appears to be a well-behaved function of ka and α, an attempt was made to represent G_1 by a simple product of these two parameters. However, expressions of the above form were found to be inaccurate (with error greater than 10 percent), due to the change in α dependence as ka increased from 0.2 to 1.0. Once this interdependence between functional forms of ka and α is identified, we recognize the parametric dependence of G_1 to be relatively complex. At this point the search for accurate closed-form expressions for perturbation fields was terminated.

4.4 Comments

As with any exact solution of a complex problem, the results are not easily approximated. Nonetheless, we have obtained accurate, compact, angular expansions for monostatic and symmetrical-incidence-bistatic perturbation fields scattered by a wedge with rounded edge. These expressions, together with tabulated coefficients, provide the reradiation characteristics for rounded-edge scattering centers having wedge angle $60° \leq 2\alpha \leq 120°$ and $0 \leq ka \leq 1.0$ without any additional work.

Corresponding angular expansions for the general bistatic case are lengthy and less accurate. Because of the complicated parametric dependence of the dominant coefficient in the above angular expansions, we conclude that it is not feasible to obtain a closed-form representation of the perturbation field.

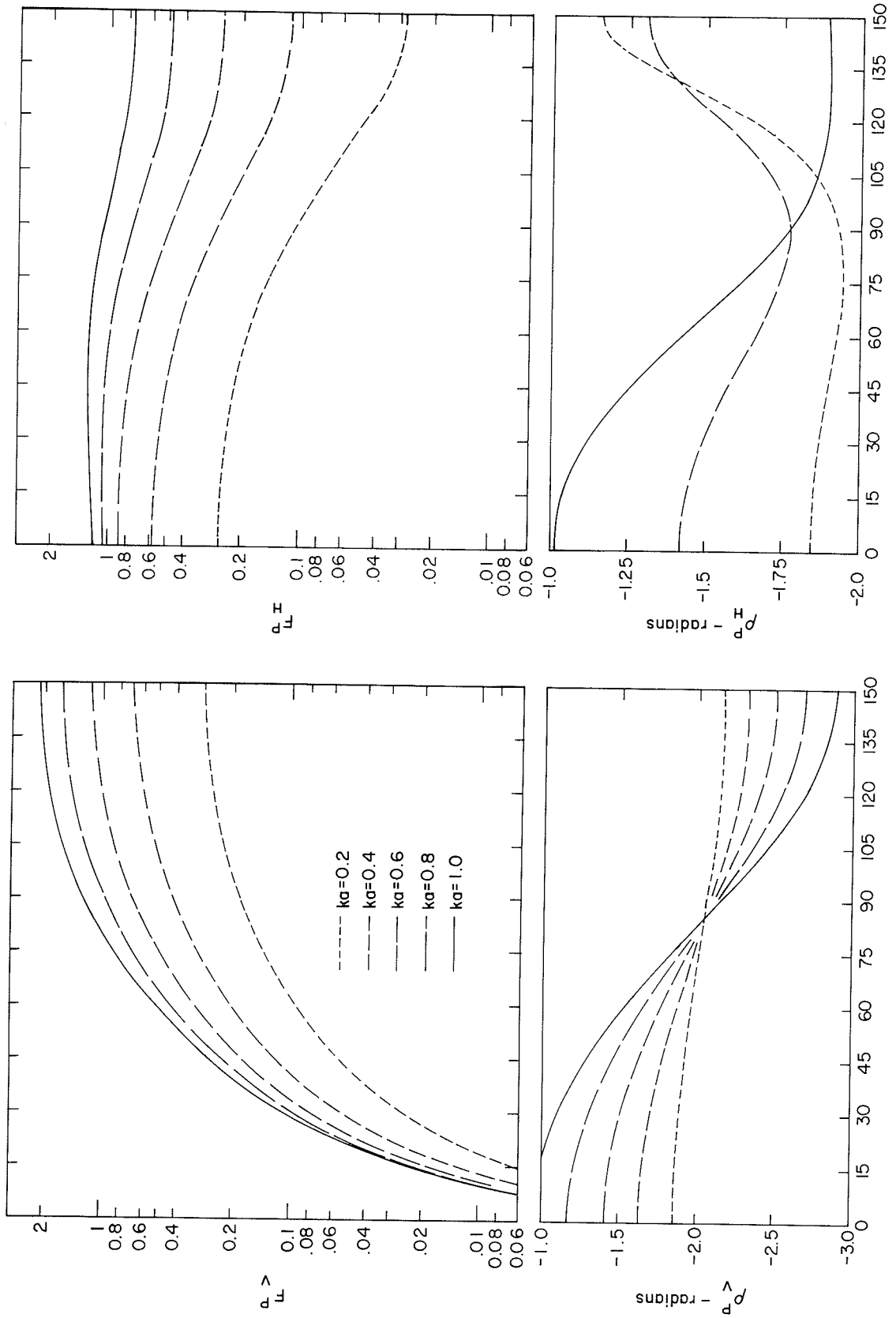

Figure 4.1 MONOSTATIC PERTURBATION DATA FOR 60° WEDGE WITH ROUNDED EDGE. $0 \leqslant ka \leqslant 1.0$

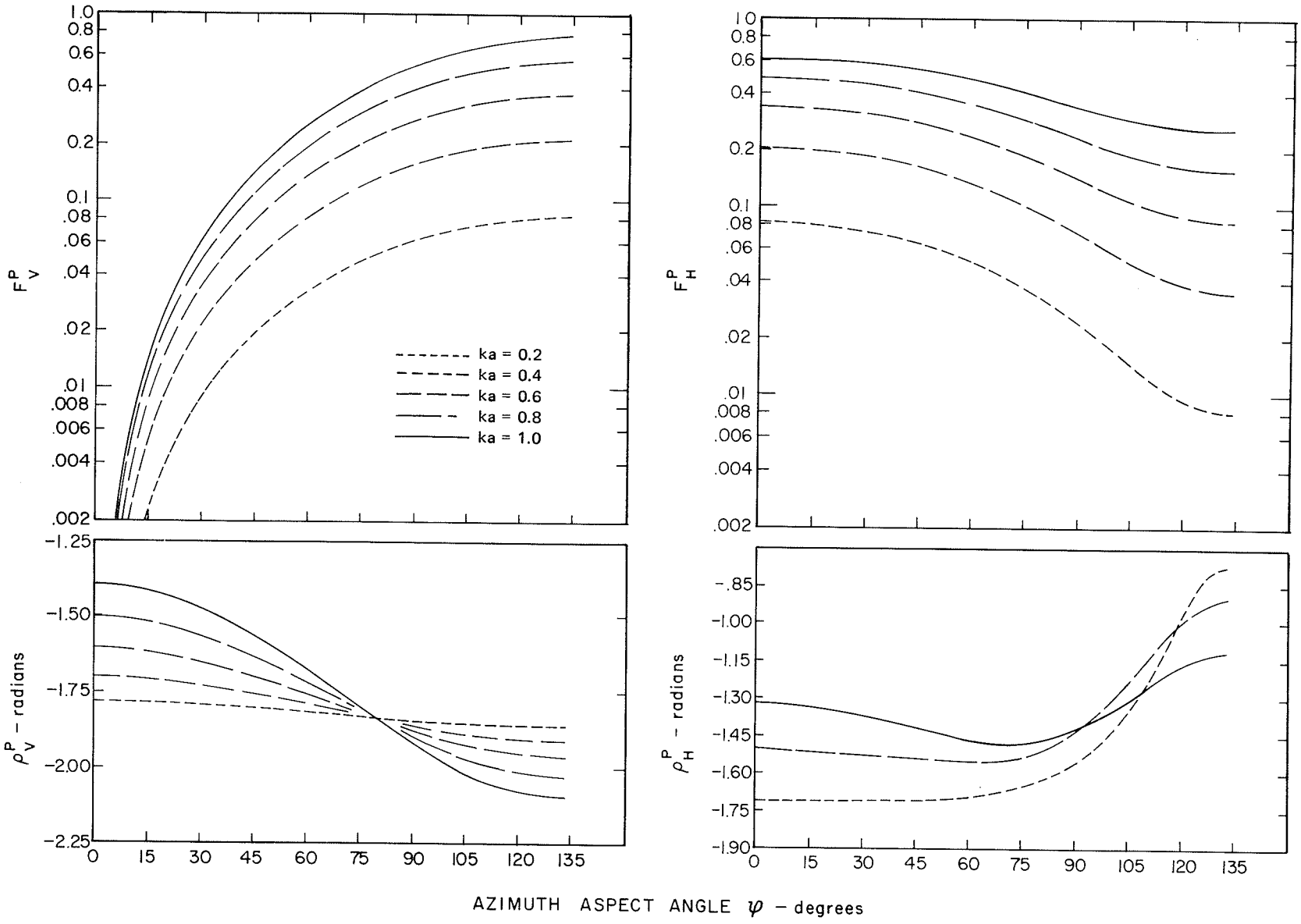

Figure 4.2 MONOSTATIC PERTURBATION DATA FOR 90° WEDGE WITH ROUNDED EDGE. $0 \leqslant ka \leqslant 1.0$

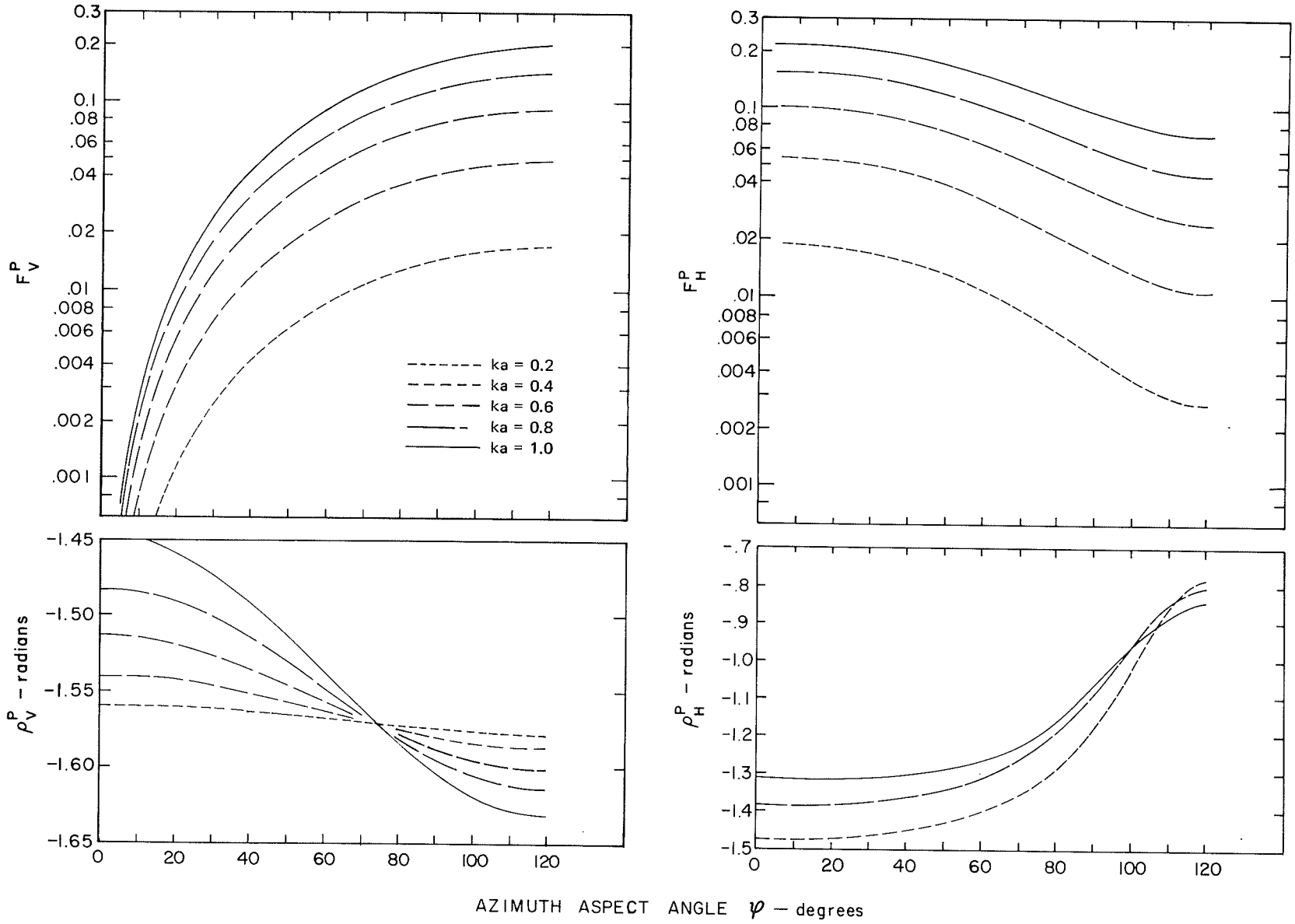

Figure 4.3 MONOSTATIC PERTURBATION DATA FOR 120° WEDGE WITH ROUNDED EDGE. $0 \leqslant ka \leqslant 1.0$

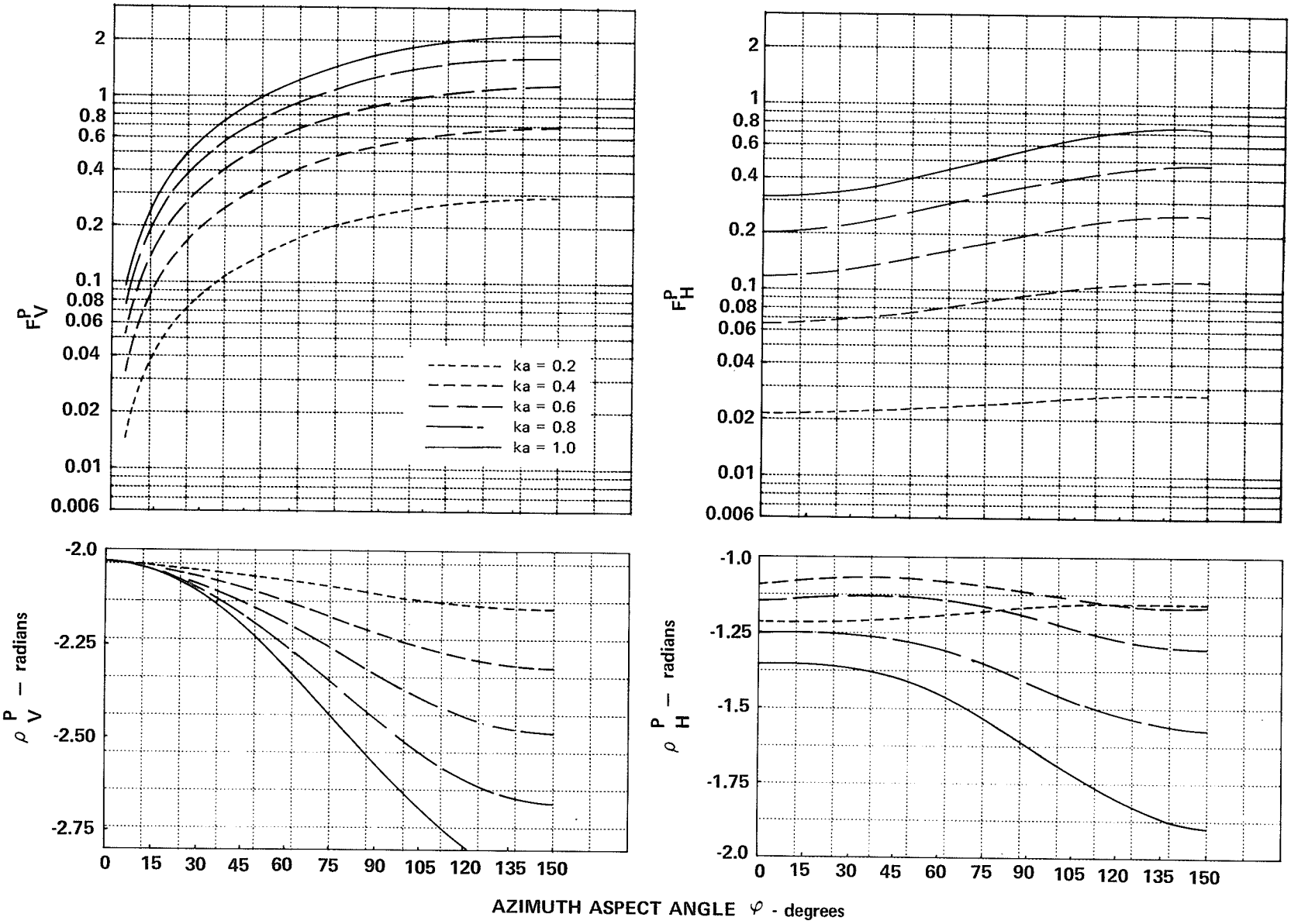

Figure 4.4 SYMMETRICAL INCIDENCE BISTATIC PERTURBATION DATA FOR 60° WEDGE WITH ROUNDED EDGE. $0 \leqslant ka \leqslant 1.0$

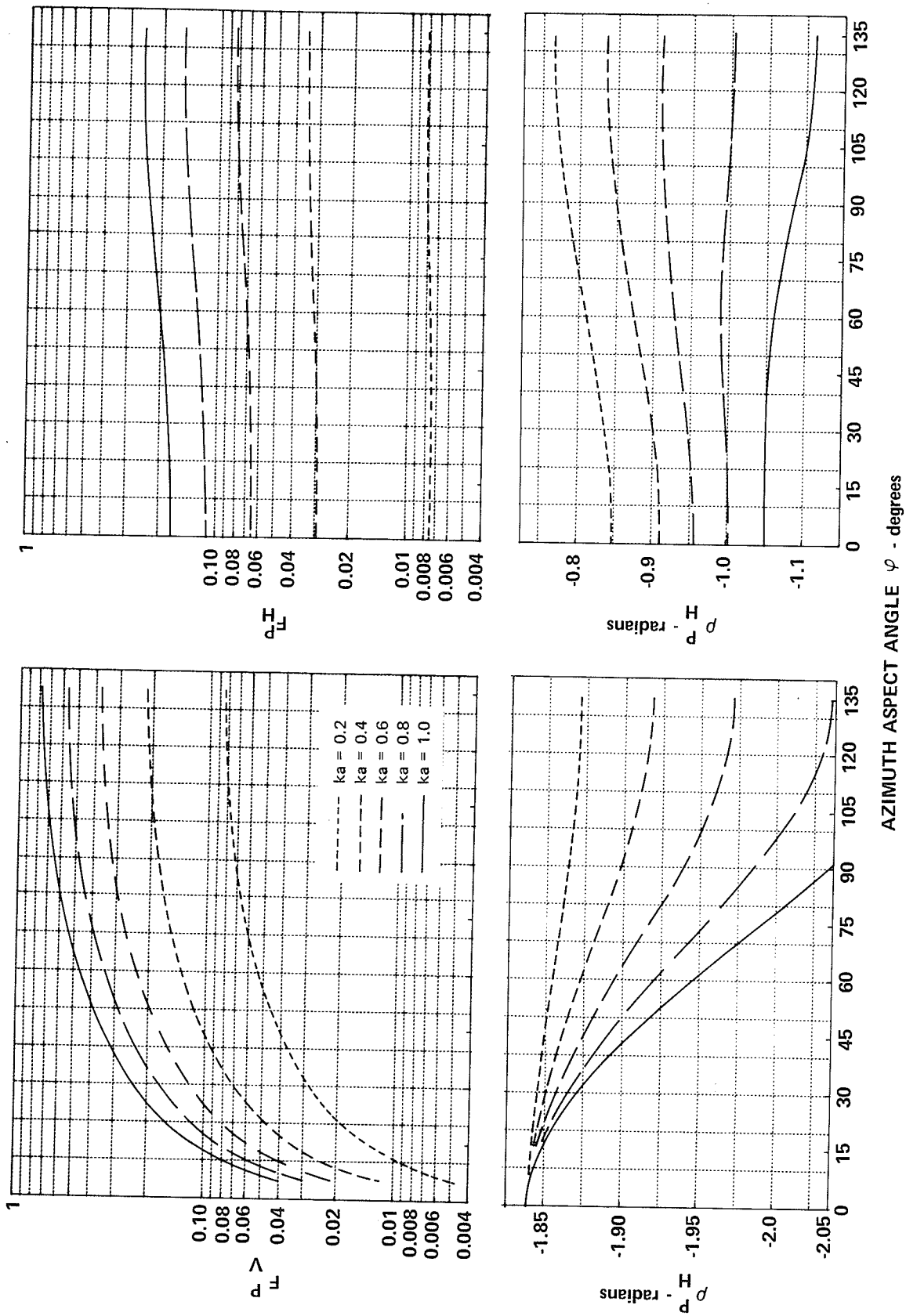

Figure 4.5 SYMMETRICAL INCIDENCE BISTATIC PERTURBATION DATA FOR 90° WEDGE WITH ROUNDED EDGE. $0 \leqslant ka \leqslant 1.0$

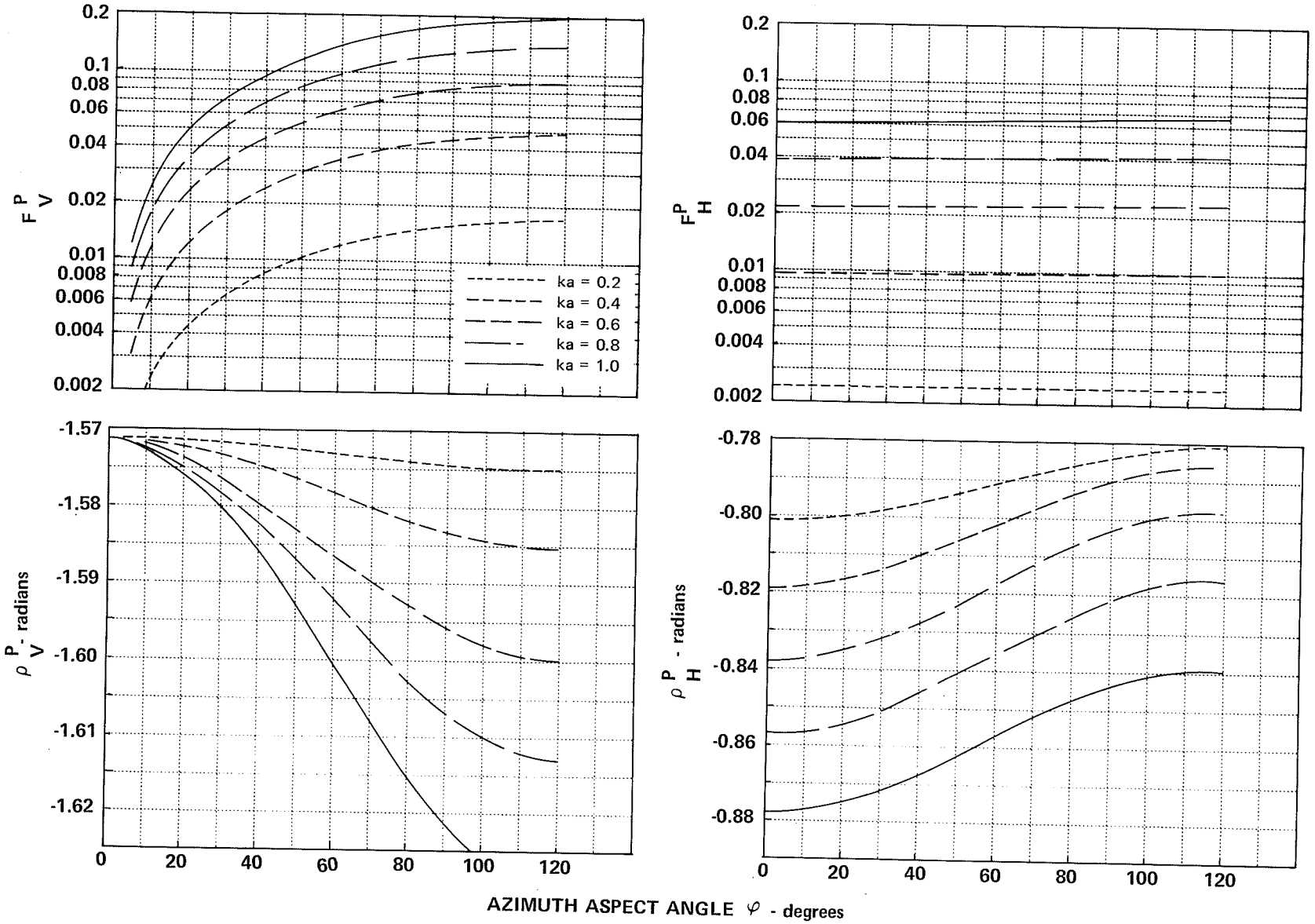

Figure 4.6 SYMMETRICAL INCIDENCE BISTATIC PERTURBATION DATA FOR 120° WEDGE WITH ROUNDED EDGE. $0 \leqslant ka \leqslant 1.0$

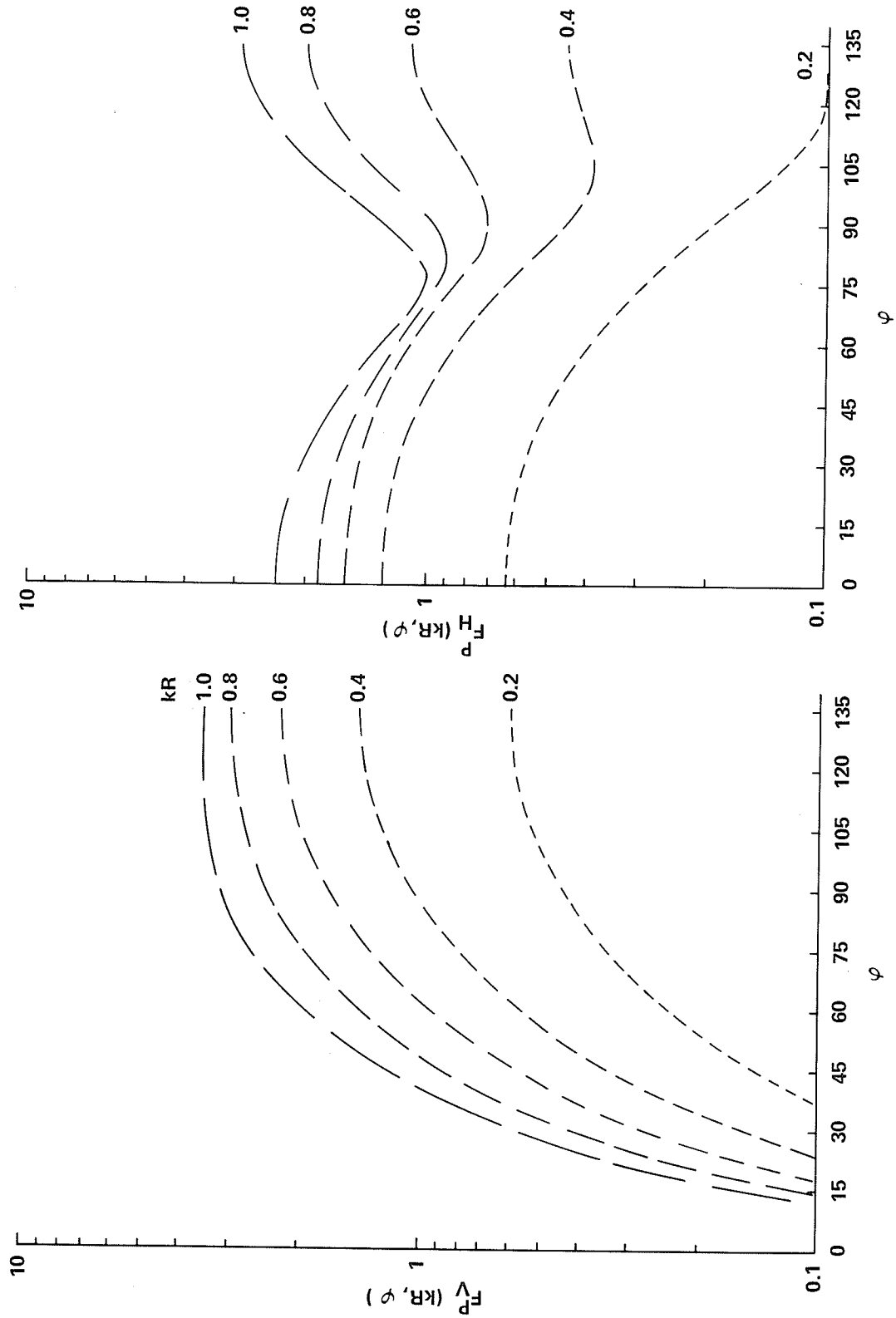

Figure 4.7 MONOSTATIC PERTURBATION DATA FOR A CYLINDRICALLY TIPPED 90° WEDGE. $0 \leqslant kR \leqslant 1.0$

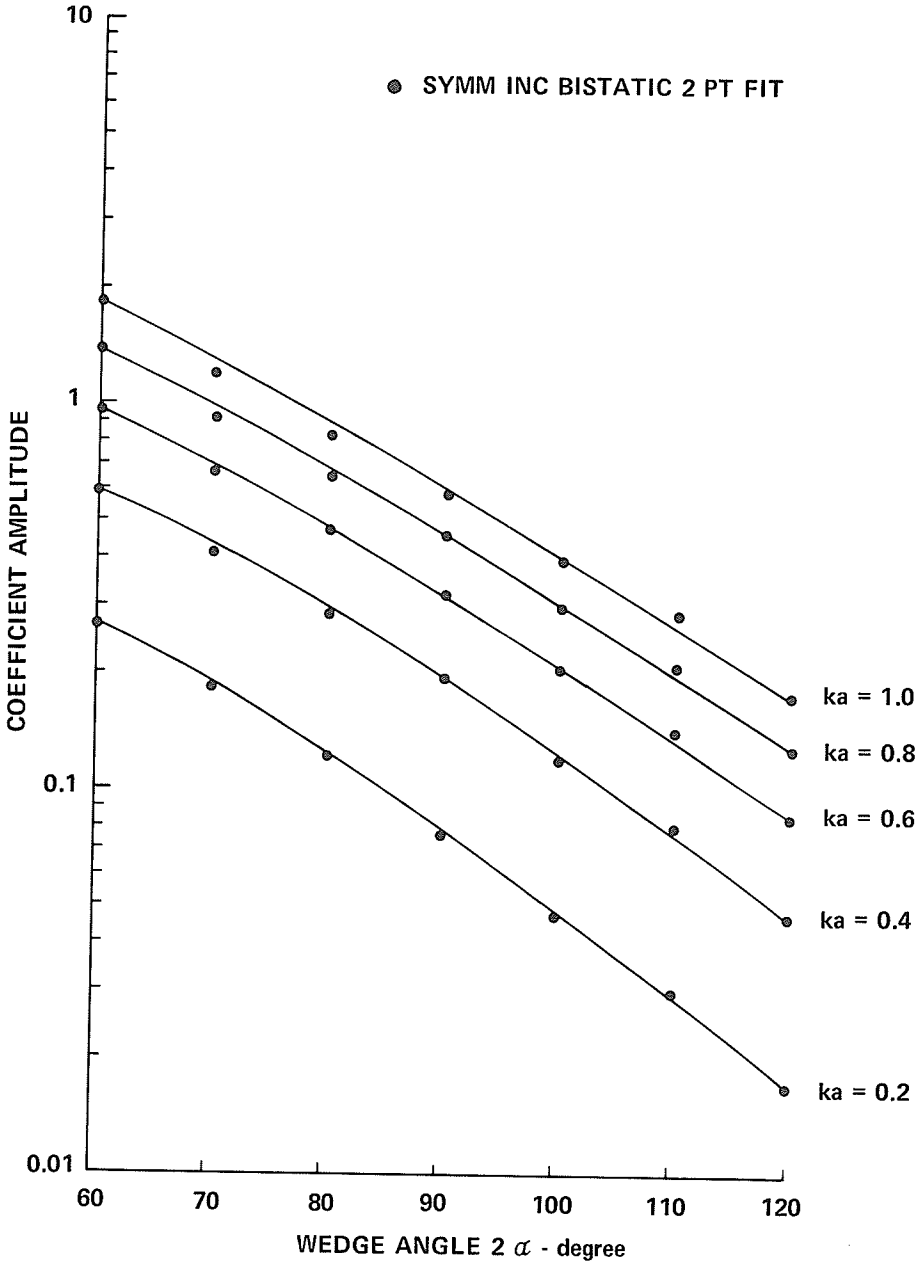

Figure 4.8 PARAMETRIC DEPENDENCE OF DOMINANT COEFFICIENT G_1 IN (4.7)

5. APPLICATIONS

The perturbation approach of Chapter 4 provides a convenient means of applying the results of the boundary value solution in the calculation of scattering by targets with one or more rounded edges. In this chapter we examine the effects of moderate rounding upon scattering by equilateral triangular prisms, square prisms, and finite, right-circular cylinders. Both the magnitude and phase of the principal polarization scattering patterns of a target are necessary in the description of the scattering process. As an example, phase is needed to completely specify the polarization scattering matrix of a target; phase data are also required when one treats scattering by multiple targets. For this reason, phase as well as magnitude information will be examined unless the presentation format suffers due to unnecessary complexity.

An evaluation of the effects of rounding the edges of targets involves the choice of some convenient gauge. We will assume that rounding is negligible provided that the change in the scattering pattern is not measurable using modern radars. Typical precision radars can supply experimental estimates of radar cross section accurate to 0.2 dB and scattering phase to within 5 degrees.

Section 5.1 treats scattering by an equilateral triangular prism. For a regular prism with sharp edges separated by at least three wavelengths, scattering center theory which neglects interactions is shown to be in excellent agreement with accurate calculations based upon an integral equation formulation. A similar comparison study involving a triangular prism with one rounded edge provides an external check on the boundary value solution. Then the scattering center theory is used to predict changes in the scattering pattern due to rounding all three edges of the triangular prism for $0.2 \leq ka \leq 1.0$.

A parallel analysis reported in Section 5.2 applies for a square prism. Extension of our work with prisms to three-dimensional targets is straightforward and Section 5.3 examines scattering by a finite, right-circular cylinder with rounded edges. General observations on the effects of rounding the edges of targets are contained in Section 5.4.

Finally, it should be realized that our analytical approach allows calculation of the reradiation characteristics of any rounded-edge scattering center having ka and α investigated in Chapter 4. Thus the prisms and cylinders treated next represent targets of convenience only.

5.1 Modified Equilateral Triangular Prism

Consider scattering by a two-dimensional equilateral triangular prism with three sharp edges as shown in Fig. 5.1(a). The electrical side length kL will be chosen large enough so that a single diffraction version of geometrical diffraction theory accurately predicts the scattering phenomenon. First the regular prism is modified in the manner shown in Fig. 5.1(b) where one edge is rounded; this configuration is employed to obtain an external check on the boundary value solution. Then a prism with three rounded edges (see Fig. 5.1(c)) is used to evaluate the effects of edge rounding.

5.1.1 Minimum Dimension of Prism

Geometrical diffraction theory has direct application to the regular prism shown in Fig. 5.1(a) since the reradiation characteristics of the scattering center formed by a sharp edge are known. As shown in this figure, the incidence (observation) angle θ_0 (θ) is referenced to a symmetry plane.

Principal polarization fields reradiated from the regular prism are easily derived using geometrical diffraction theory (single-diffraction terms only) in the manner outlined in Refs. 29 and 31. Expressing the radar cross section σ per unit length in terms of the scattering pattern $Fe^{j\rho}$ we have

$$\sigma = \frac{F^2}{k} \tag{5.1}$$

where

$$F = \left| F_1 e^{j\rho} + F_2 e^{j\rho} + F_3 e^{j\rho} \right| \tag{5.2}$$

$$\rho = \tan^{-1} \left\{ \frac{F_1 \sin\rho_1 + F_2 \sin\rho_2 + F_3 \sin\rho_3}{F_1 \cos\rho_1 + F_2 \cos\rho_2 + F_2 \cos\rho_3} \right\} \tag{5.3}$$

and the numerical subscripts refer to edges labelled in Fig. 5.1(a). In the angular interval $\theta \le \theta_0$, $\theta \le \pi$, the amplitudes assigned to edge scattering centers are given by

$$F_1 = \frac{\sin\left(\frac{\pi}{\gamma}\right)}{\gamma} \left[\left\{ \cos\left(\frac{\pi}{\gamma}\right) - \cos\left(\frac{3\pi - \theta_0 - \theta}{\gamma}\right) \right\}^{-1} \mp \left\{ \cos\left(\frac{\pi}{\gamma}\right) - \cos\left(\frac{\theta_0 - \theta}{\gamma}\right) \right\}^{-1} \right] \tag{5.4}$$

$$F_2 = \frac{\sin\left(\frac{\pi}{\gamma}\right)}{\gamma} \left[\left\{ \cos\left(\frac{\pi}{\gamma}\right) - \cos\left(\frac{3\pi + \theta_0 + \theta}{\gamma}\right) \right\}^{-1} \mp \left\{ \cos\left(\frac{\pi}{\gamma}\right) - \cos\left(\frac{\theta_0 - \theta}{\gamma}\right) \right\}^{-1} \right]; \; 0 \le \theta_0, \theta \le \alpha$$

$$= 0; \; \alpha < \theta_0, \; \theta < \frac{\pi}{2}$$

$$= \frac{\sin\left(\frac{\pi}{\gamma}\right)}{\gamma} \left[\left\{ \cos\left(\frac{\pi}{\gamma}\right) - \cos\left(\frac{\pi - \theta_0 - \theta}{\gamma}\right) \right\}^{-1} \mp \left\{ \cos\left(\frac{\pi}{\gamma}\right) - \cos\left(\frac{\theta_0 - \theta}{\gamma}\right) \right\}^{-1} \right]; \; \frac{\pi}{2} \le \theta_0, \theta \le \pi$$

$$= \frac{\sin\left(\frac{\pi}{\gamma}\right)}{\gamma} \left[\left\{ \cos\left(\frac{\pi}{\gamma}\right) - \cos\left(\frac{\pi + \theta_0 + \theta}{\gamma}\right) \right\}^{-1} \mp \left\{ \cos\left(\frac{\pi}{\gamma}\right) - \cos\left(\frac{2\pi - \theta_0 - \theta}{\gamma}\right) \right\}^{-1} \right]; \tag{5.5}$$

$$0 \le \theta_0 \le \alpha, \; \frac{\pi}{2} \le \theta \le \pi$$

$$F_3 = \frac{\sin\left(\frac{\pi}{\gamma}\right)}{\gamma}\left[\left\{\cos\left(\frac{\pi}{2}\right)-\cos\left(\frac{\pi+\theta_0+\theta}{\gamma}\right)\right\}^{-1} \mp \left\{\cos\left(\frac{\pi}{\gamma}\right)-\cos\left(\frac{\theta_0-\theta}{\gamma}\right)\right\}^{-1}\right];\ \theta \le \theta_0,\ \theta \le \pi-\alpha$$

$$= 0;\ \pi-\alpha < \theta_0,\ \theta \le \pi \qquad (5.6)$$

and the phases assigned to edge scattering centers, referenced to the origin of Fig. 5.1(a), are given by

$$\rho_1 = -\frac{\pi}{4} - kL\left[\cos(\alpha+\theta_0) + \cos(\alpha+\theta)\right] \qquad (5.7)$$

$$\rho_2 = -\frac{\pi}{4} - kL\left[\cos(\alpha-\theta_0) + \cos(\alpha-\theta)\right] \qquad (5.8)$$

$$\rho_3 = -\frac{\pi}{4} \qquad (5.9)$$

where $\gamma = 5/3$ and $\alpha = 30°$.

The upper and lower signs in (5.4) through (5.6) refer to vertical and horizontal polarizations respectively. Angular restrictions on (5.4) through (5.6) are a consequence of a single-diffraction analysis; individual centers contribute to the total scattered field only when they are directly illuminated by the transmitter and directly "observed" by the receiver. Finally, the presence of singularities at aspects which produce specular scattering ($\theta_0 = \theta = \frac{\pi}{2} - \alpha$, $\theta_0 = \theta = \pi$, $\theta_0 + \theta = \pi - 2\alpha$) and for the forward-scattering case ($\theta - \theta_0 = \pi$) is noted in (5.4) through (5.6). This situation is characteristic of applications of unmodified geometrical diffraction theory. However, singularities may be cancelled to yield the following valid expressions[64]

$$F\left(\theta_0 = \theta = \frac{\pi}{2} - \alpha\right) = \left| kL e^{j\frac{\pi}{4}} \mp 2\frac{\sin\left(\frac{\pi}{\gamma}\right)}{\gamma}\left\{\cos\left(\frac{\pi}{\gamma}\right) - 1\right\}^{-1} e^{-j\frac{\pi}{4}} \right| \tag{5.10}$$

$$\equiv F(\theta_0 = \theta = \pi)$$

$$F(\theta_0 = 0;\ \theta = \pi - 2\alpha) = \left| kL e^{+j\frac{\pi}{4}} \mp 2\frac{\sin\left(\frac{\pi}{\gamma}\right)}{\gamma}\left\{\cos\left(\frac{\pi}{\gamma}\right) - \cos\left(\frac{\pi - 2\alpha}{\gamma}\right)\right\}^{-1} e^{-j\frac{\pi}{4}} + F_2\, e^{-j\frac{\pi}{4}} \right| \tag{5.11}$$

$$F(\theta_0 = 0;\ \theta = \pi) = \left| kL e^{j\frac{\pi}{4}} \pm 2\frac{\sin\left(\frac{\pi}{\gamma}\right)}{\gamma}\left\{\cos\left(\frac{\pi}{\gamma}\right) - \cos\left(\frac{2\pi}{\gamma}\right)\right\}^{-1} e^{-j\frac{\pi}{4}} \right| \tag{5.12}$$

Thus $F(\theta_0, \theta)$ is a continuous function with valid limiting representations given by (5.10) through (5.12). This completes the single diffraction description of scattering by the regular triangular prism of Fig. 5.1(a) based upon geometrical diffraction theory.

It is known that the accuracy of geometrical diffraction theory increases with an increase in the separation between scattering centers. We now wish to establish a minimum value of kL for which interaction phenomena are negligible. To accomplish this we compare results of approximate theory with accurate predictions based upon an integral equation formulation (IEF) of the scattering problem. It is only necessary to consider one polarization combination, and we choose the vertical polarization case. Table 5.1 compares the magnitudes of the scattering pattern $F_{v(GDT)}$ and $F_{v(IEF)}$ for a regular triangular prism with electrical side length kL = 20. $F_{v(IEF)}$ calculations based upon (B.7) of Appendix B are accurate to at least three significant figures. The data presented in Table 5.1 show that geometrical diffraction theory (5.2 through 5.12) is accurate to within 7 percent, with maximum error at the monostatic aspect which corresponds to shadowing of an edge. We conclude that the single

Table 5.1 SCATTERING PATTERN OF A REGULAR TRIANGULAR PRISM (ka = 0, kL = 20)

MONOSTATIC $\Theta = \Theta_0$				BISTATIC $\Theta_0 = 0^o$			
Θ^o	$F_{v(GDT)}$	$F_{v(IEF)}$	% ERROR	Θ^o	$F_{v(GDT)}$	$F_{v(IEF)}$	% ERROR
0	1.410	1.422	-0.8	0	1.410	1.422	-0.8
10	1.158	1.111	4.2	20	1.241	1.203	3.2
20	1.166	1.153	1.1	40	1.291	1.226	5.0
30	1.448	1.547	-6.4	60	1.686	1.686	0.0
40	1.815	1.860	-2.4	80	2.653	2.624	1.1
50	2.135	2.181	-2.1	100	4.652	4.622	0.6
60	20.02	20.09	-0.3	120	10.12	9.866	2.6

Table 5.2 SCATTERING PATTERN OF A MODIFIED TRIANGULAR PRISM (ka = 1.0, kL = 20)

MONOSTATIC $\Theta = \Theta_0$				BISTATIC $\Theta_0 = 0^o$			
Θ^o	$F_{v(GDT)}$	$F_{v(IEF)}$	% ERROR	Θ^o	$F_{v(GDT)}$	$F_{v(IEF)}$	% ERROR
0	1.886	1.923	-1.9	0	1.886	1.923	-1.9
10	1.956	2.040	-4.1	20	1.999	2.076	-3.7
20	1.715	1.758	-2.4	40	2.060	2.122	-3.1
30	1.576	1.695	-6.3	60	2.405	2.440	-1.4
40	1.586	1.595	-0.6	80	3.228	3.231	-0.1
50	1.613	1.607	0.4	100	5.256	5.264	-0.2
60	18.82	18.79	0.2	120	9.207	9.296	-1.0

diffraction version of geometrical diffraction theory accurately describes scattering by a regular triangular prism with side length $kL \geq 20$.

5.1.2 External Check on Boundary Value Solution

The integral equation formulation has been extended to provide accurate estimates of vertical polarization scattering by the modified prism shown in Fig. 5.1(b). With one edge rounded (B.9) of Appendix B applies. Geometrical diffraction theory is easily extended to the modified prism using the perturbation approach on the rounded edge. Here we replace $F_3 e^{j\rho_3}$ in (5.2) with the return $F_{R_3} e^{j\rho_3}$ associated with a rounded edge, i.e.,

$$F_{R_3} e^{j\rho_{R_3}} = F_3 e^{j\rho_3} + F^P e^{j\rho^P} \tag{5.13}$$

In (5.13), F_3 and ρ_3 are given by (5.6) and (5.9). The complex perturbation $F^P e^{j\rho^P}$ associated with rounding edge number 3 can be determined from analyses of the 60° wedge reported in Chapter 4. The perturbation magnitude F^P has the form of (4.3) with $\varphi \rightarrow \pi - \alpha - \theta$ and with polarization-dependent coefficients contained in Tables 4.1 and 4.3. Similarly, the perturbation phase ρ^P is given by (4.4) with coefficients listed in Tables 4.3 and 4.4. For the symmetrical-incidence bistatic case, vertical polarization magnitude F_V and phase ρ_V have the forms (4.5) and (4.6) with coefficients listed in Tables 4.5 and 4.6, respectively. Finally, the limiting formulas (5.10) through (5.12) are also modified by the inclusion of $F^P e^{j\rho^P}$.

Table 5.2 compares scattering pattern magnitudes at vertical polarization for a triangular prism with electrical side length $kL = 20$ and a near edge with rounding $ka = 1.0$ (see Fig. 5.1(b)). The overall agreement

between $F_{V(IEF)}$ and $F_{V(GDT)}$ shown in Table 5.1 is preserved. Thus the data in Table 5.2 constitute an external check on the boundary value solution and its application through the perturbation approach.

5.1.3 Scattering by a Triangular Prism with Three Rounded Edges

Fig. 5.1(c) depicts an equilateral triangular prism modified such that all three edges are rounded with equal radii of curvature a. Monostatic scattering by a triangular prism with three rounded edges is estimated using (5.1) through (5.12) with modifications of the form of (5.13) for all three scattering centers. Specifically, we retain (5.13) and expand (5.4) and (5.5) in the following manner:

$$F_{R_1} e^{j\rho_{R_1}} = F_1 e^{j\rho_1} + F^P(\theta - 120) e^{j\rho^P(\theta-120)} \tag{5.14}$$

$$F_{R_2} e^{j\rho_{R_2}} = F_2 e^{j\rho_2} + F^P(\theta + 120) e^{j\rho^P(\theta+120)} \tag{5.15}$$

where the perturbation contribution $F^P(\theta + x) e^{j\rho^P(\theta+x)}$ is shifted by an angle x from the contribution $F^P e^{j\rho^P}$ obtained in the manner described for (5.13).

By incorporating the above modifications we can evaluate the dependence of the scattering phenomenon upon edge rounding using scattering center theory. Figs. 5.2 through 5.6 present the magnitude and phase of the principal polarization scattering patterns of the triangular prism with three equally rounded edges for $0 \leq ka \leq 1.0$. In Fig. 5.2, a rounding of $ka = 0.2$ produces negligible change in the scattering pattern of the regular triangular prism. Notice that the peak in F_H occurring for $\theta = 18°$ is most sensitive to this small degree of rounding. For $ka = 0.4$, Fig. 5.3

shows that the effect of rounding upon magnitude and phase is no longer negligible for either principal polarization. Considerable alteration of the pattern for the regular prism is observed in Fig. 5.4 when ka = 0.6; peak and null locations are shifted and the magnitude of the horizontal polarization pattern assumes a different character in the angular region about θ = 18°. The effect of increasing rounding to ka = 0.8 and ka = 1.0 are shown in Figs. 5.5 and 5.6. Here the character of the pattern for the regular prism is completely altered except in the angular region containing the specular peak ($\theta \sim 60°$); cross section differences of greater than 15 dB occur along with phase differences as large as 180°.

5.2 Modified Square Prism

Next we examine the scattering characteristics of a square prism as a function of edge rounding. Fig. 5.7(a) depicts a regular square prism with scattering centers formed by the four sharp edges. The electrical side length is again chosen to be 20 to assure that interactions between scattering centers are negligible.

For the monostatic case ($\theta = \theta_0$), symmetry allows us to treat the limited aspect interval $0 \le \theta \le \frac{\pi}{4}$, in which case the edge labelled 4 in Fig. 5.7(a) does not contribute in the single-diffraction analysis. The amplitudes and phases assigned to edge scattering centers are given by

$$F_1 = \frac{\sin\left(\frac{\pi}{\gamma}\right)}{\gamma}\left[\left\{\cos\left(\frac{\pi}{\gamma}\right) - \cos\left(\frac{\frac{\pi}{2}+2\theta}{\gamma}\right)\right\}^{-1} \mp \left\{\cos\left(\frac{\pi}{\gamma}\right) - 1\right\}^{-1}\right] \tag{5.16}$$

$$F_2 = \frac{\sin\left(\frac{\pi}{\gamma}\right)}{\gamma}\left[\left\{\cos\left(\frac{\pi}{\gamma}\right) - \cos\left(\frac{\frac{\pi}{2}-2\theta}{\gamma}\right)\right\}^{-1} \mp \left\{\cos\left(\frac{\pi}{2}\right) - 1\right\}^{-1}\right] \tag{5.17}$$

$$F_3 = \frac{\sin\left(\frac{\pi}{\gamma}\right)}{\gamma}\left[\left\{\cos\left(\frac{\pi}{\gamma}\right) - \cos\left(\frac{2\theta}{\gamma}\right)\right\}^{-1} \mp \left\{\cos\left(\frac{\pi}{2}\right) - 1\right\}^{-1}\right] \tag{5.18}$$

$$\rho_1 = -\frac{\pi}{4} - 2kL\cos(\alpha+\theta) \tag{5.19}$$

$$\rho_2 = -\frac{\pi}{4} - 2kL\cos(\alpha-\theta) \tag{5.20}$$

$$\rho_3 = -\frac{\pi}{4} \tag{5.21}$$

with $\gamma = 3/2$ and $\alpha = \pi/4$. When $\theta = \pi/4$, specular scattering is determined by

$$F\left(\theta = \frac{\pi}{2} - \alpha\right) = \left| kL\, e^{j\frac{\pi}{4}} \mp 2\frac{\sin\left(\frac{\pi}{\gamma}\right)}{\gamma}\left\{\cos\left(\frac{\pi}{\gamma}\right) - 1\right\}^{-1} e^{-j\frac{\pi}{4}} \right| \tag{5.22}$$

Equations (5.16) through (5.22), together with (5.1) through (5.3), allow prediction of monostatic scattering by a regular square prism for both principal polarizations.

Figure 5.7(b) shows a modified square prism with equal rounding of all four edges. Scattering by the modified prism is predicted using the perturbation data presented in Chapter 4. The necessary extension to (5.16) through (5.22) parallels the steps outlined in Section 5.1; the important difference is that perturbation data for a 90° wedge apply here (see Tables 4.1, 4.2, 4.3, and 4.4). Figs. 5.8 through 5.10 present the magnitude and phase of the principal polarization scattering patterns of the square prism with four equally rounded edges for $0 \leq ka \leq 1.0$. According to data shown in Fig. 5.8, a rounding of $ka < 0.6$ produces negligible change in the scattering pattern of the square prism. When rounding is increased to $ka = 0.8$, Fig. 5.9 indicates appreciable change in the magnitude of nonspecular peaks. Finally, rounding of $ka = 1.0$ has a significant effect upon both the location and magnitude of peaks in the pattern; results shown in Fig. 5.10 indicate up to 5 dB change in radar cross section and as much as 30° change in scattering phase.

5.3 Modified Finite Right-Circular Cylinder

In this section we examine the effect of rounding the edges of a finite, right-circular cylinder to illustrate the application of our analysis to three-dimensional targets. For this target, the two-dimensional analysis of Section 5.2 applies directly provided we incorporate the proper divergence factor. Briefly, the divergence factor is a geometrical construction introduced so that theory satisfies the optical form of the law of conservation of energy. Thus the following analysis of scattering by regular and modified finite, right-circular cylinders is a straightforward extention of our previous work.[29]

First consider monostatic scattering by a regular cylinder with four sharp edges. Let the center of the cylinder be the phase reference and let the aspect angle θ be measured from the axis of the target to the radar line-of-sight as shown in Fig. 5.11(a). Here A is the radius of the cylinder and h is the half-height. Target symmetry requires definition of scattering in the limited aspect interval $0 \le \theta \le \frac{\pi}{2}$.

The expression for three-dimensional radar cross section is

$$\sigma = \frac{F^2}{k^2} \tag{5.23}$$

where

$$F = \left| \sum_{i=1}^{3} F_i e^{j\rho_i} \right| \tag{5.24}$$

with the amplitude of each contribution given by

$$F_1 = C_1 \frac{\sin\left(\frac{\pi}{\gamma}\right)}{\gamma} \left[\left\{ \cos\left(\frac{\pi}{\gamma}\right) - \cos\left(\frac{\pi+2\theta}{\gamma}\right) \right\}^{-1} \mp \left\{ \cos\left(\frac{\pi}{\gamma}\right) - 1 \right\}^{-1} \right] \tag{5.25}$$

$$F_2 = C_2 \frac{\sin\left(\frac{\pi}{\gamma}\right)}{\gamma}\left[\left\{\cos\left(\frac{\pi}{\gamma}\right)-\cos\left(\frac{\pi-2\theta}{\gamma}\right)\right\}^{-1} \mp \left\{\cos\left(\frac{\pi}{\gamma}\right)-1\right\}^{-1}\right] \tag{5.26}$$

$$F_3 = C_3 \frac{\sin\left(\frac{\pi}{\gamma}\right)}{\gamma}\left[\left\{\cos\left(\frac{\pi}{\gamma}\right)-\cos\frac{2\theta}{\gamma}\right\}^{-1} \mp \left\{\cos\left(\frac{\pi}{\gamma}\right)-1\right\}^{-1}\right] \tag{5.27}$$

and with the geometric phases

$$\rho_1 = -\frac{\pi}{4} + 2k(A\sin\theta + h\cos\theta) \tag{5.28}$$

$$\rho_2 = -\frac{\pi}{4} - 2k(A\sin\theta - h\cos\theta) \tag{5.29}$$

$$\rho_3 = -\frac{\pi}{4} + 2k(A\sin\theta + h\cos\theta) \tag{5.30}$$

Accounting for a change in aspect and phase references, (5.25) through (5.30) are the same as (5.16) through (5.21) except for the quantities

$$C_1 = C_3 = \sqrt{\frac{kA}{\sin\theta}} \tag{5.31}$$

$$C_2 = C_1 e^{j\frac{\pi}{2}} \tag{5.32}$$

which arise in the evaluation of the divergence factor. When incidence is axial or broadside, specular scattering is given by[29]

$$F(\theta \to 0) = 2\sqrt{\pi}(kA)^2 \frac{J_1(2kA\sin\theta)}{2kA\sin\theta} e^{j\frac{\pi}{2} + j2kh\cos\theta} \tag{5.33}$$

$$F(\theta \to \tfrac{\pi}{2}) = -2kh\sqrt{kA}\,\frac{\sin(2kh\cos\theta)}{2kh\cos\theta} e^{-j\frac{3\pi}{4} + j2kA\sin\theta} \tag{5.34}$$

Equations (5.23) through (5.34) allow prediction of monostatic scattering by a regular finite, right-circular cylinder for both principal polarizations.

Figure 5.11(b) depicts a finite, right-circular cylinder modified such that edges have equal radii of curvature a. To predict scattering by the modified cylinder, we replace (5.24) through (5.30) with equations of the form

$$F_{R_i} e^{j\rho_{R_i}} = F_i e^{j\rho_i} + C_i F_i^P e^{j(\rho_i^P + \rho_i - \frac{\pi}{4})} \tag{5.35}$$

which in turn will alter the limiting formulas (5.33) and (5.34). The complex perturbation $F_i^P e^{j\rho_i^P}$ in (5.35) is determined from Tables 4.1 through 4.4 using F^P and ρ^P for a 90° wedge with angular shifts given by

$$\begin{aligned} F_1^P e^{j\rho_1^P} &= F^P(\theta - 45)\, e^{j\rho^P(\theta - 45)} \\ F_2^P e^{j\rho_2^P} &= F^P(\theta + 45)\, e^{j\rho^P(\theta + 45)} \\ F_3^P e^{j\rho_3^P} &= F^P(\theta - 135)\, e^{j\rho^P(\theta - 135)} \end{aligned} \tag{5.36}$$

Figs. 5.12 through 5.15 present the magnitude of the scattering pattern of a finite right-circular cylinder with $kA = kh = 10$, $0 \le ka \le 1.0$. From Figs. 5.12 and 5.13 we conclude that edge roundings less than ka = 0.8 have small effect upon principal polarization patterns. For ka = 1.0, Figs. 5.14 and 5.15 show appreciable change in the pattern magnitude, especially at intermediate aspects.

5.4 Conclusions

Results for modified triangular and square prisms show that, for a given rounding, the scattering pattern is most sensitive to target shape; the narrower the wedge angle 2α associated with target geometry, the greater the effect of rounding. Studies involving the square prism and right circular cylinder indicate that, for fixed wedge angle, patterns of

two- and three-dimensional targets exhibit much the same sensitivity to rounding.

The change in the scattering pattern of a target due to rounding is not markedly dependent upon aspect angle provided we exclude those aspects which give rise to specular scattering. Then the choice of polarization determines the following general behavior: for vertical polarization, rounding increases the magnitude of peaks; for horizontal polarization, peak values are reduced by rounding. This dependence stems from the fact that the dominant return for vertical (horizontal) polarization arises at the near (far) scattering centers on the target, which experience increase (decrease) with rounding due to the aspect dependence noted in Chapter 2.

As the scattering center progresses from a sharp edge to one with finite but small rounding, the scattering pattern of the target exhibits fluctuations in the magnitudes of nonspecular peaks while retaining the same peak-null character in aspect angle. This initial behavior indicates that change is due to F^{P} rather than to ρ^{P}. Increase in rounding leads to change in the peak-null character as well, i.e., the perturbation phase ρ^{P} is now also important in determining the effect of rounding upon the scattering pattern of the target.

It should be realized that rounding the edge of a target alters the envelope of the peaks in the scattering pattern. At aspects other than specular, this envelope is independent of the dimensions of the target, (i.e., kL, kA or kh). Thus the observations noted with targets three wavelengths on a side will apply for much larger targets as well. Finally, another advantage of the perturbation approach becomes apparent: analytical expressions of scattering by targets with rounded edges retain the singularity-cancellation capability of the unmodified theory.

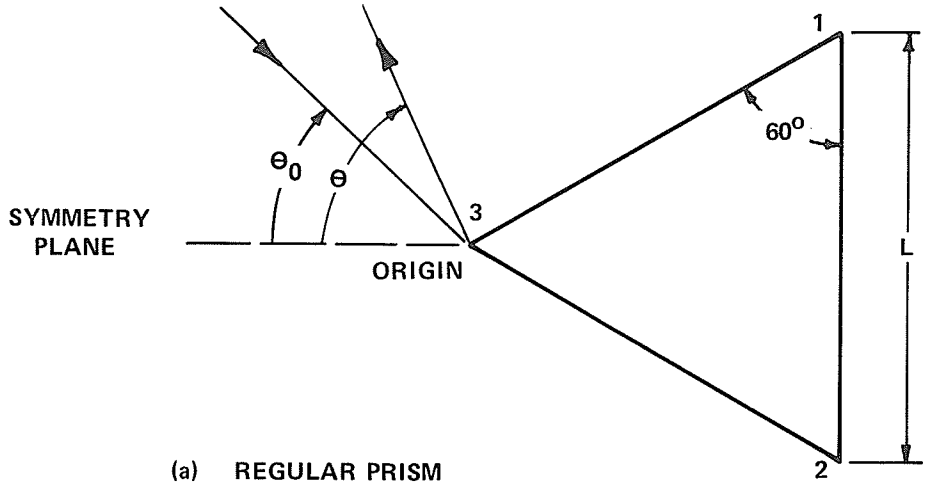

(a) REGULAR PRISM

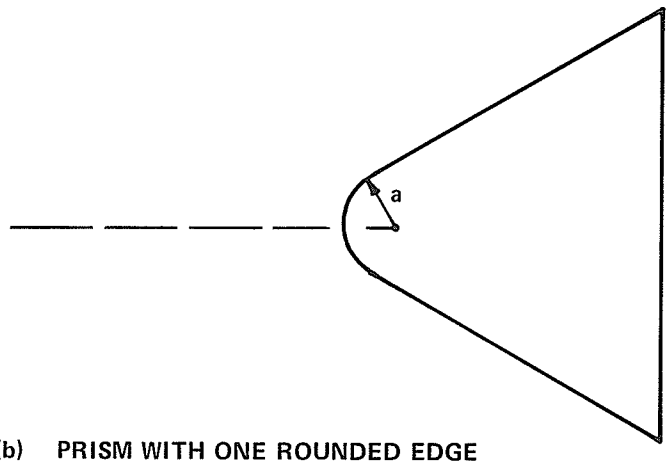

(b) PRISM WITH ONE ROUNDED EDGE

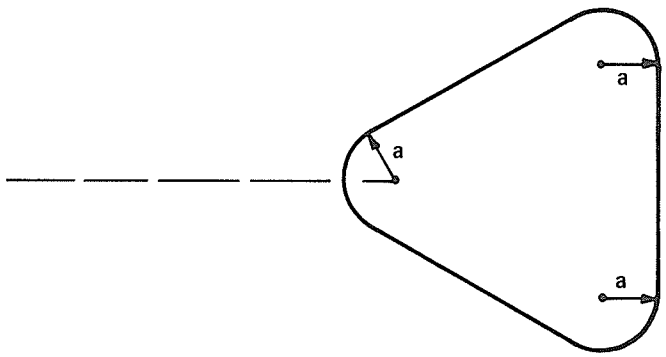

(c) MODIFIED PRISM WITH THREE ROUNDED EDGES

Figure 5.1 REGULAR AND MODIFIED EQUILATERIAL TRIANGULAR PRISMS

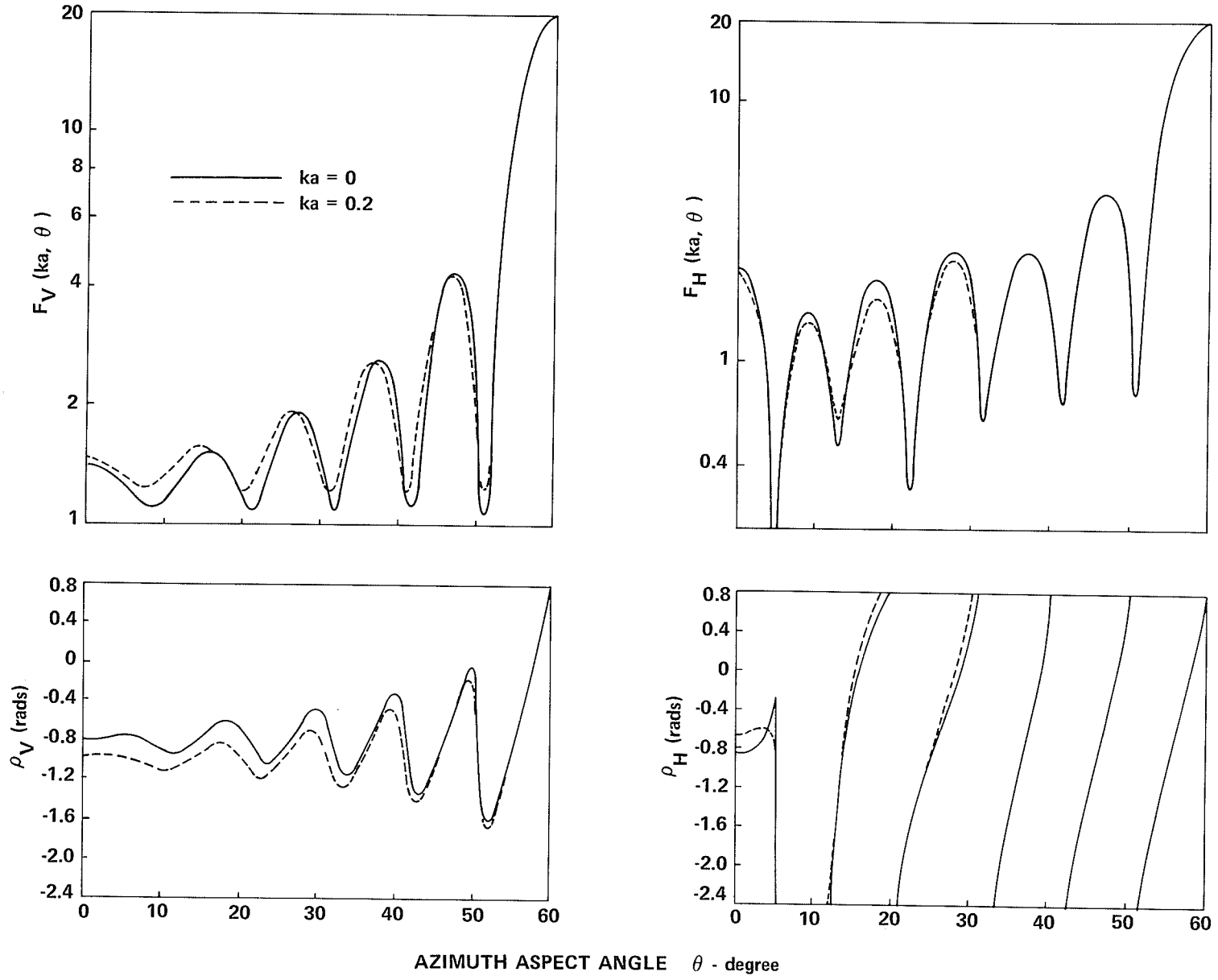

Figure 5.2 BACKSCATTERING FROM A MODIFIED EQUILATERAL TRIANGULAR PRISM. kL = 20. ka = 0, 0.2

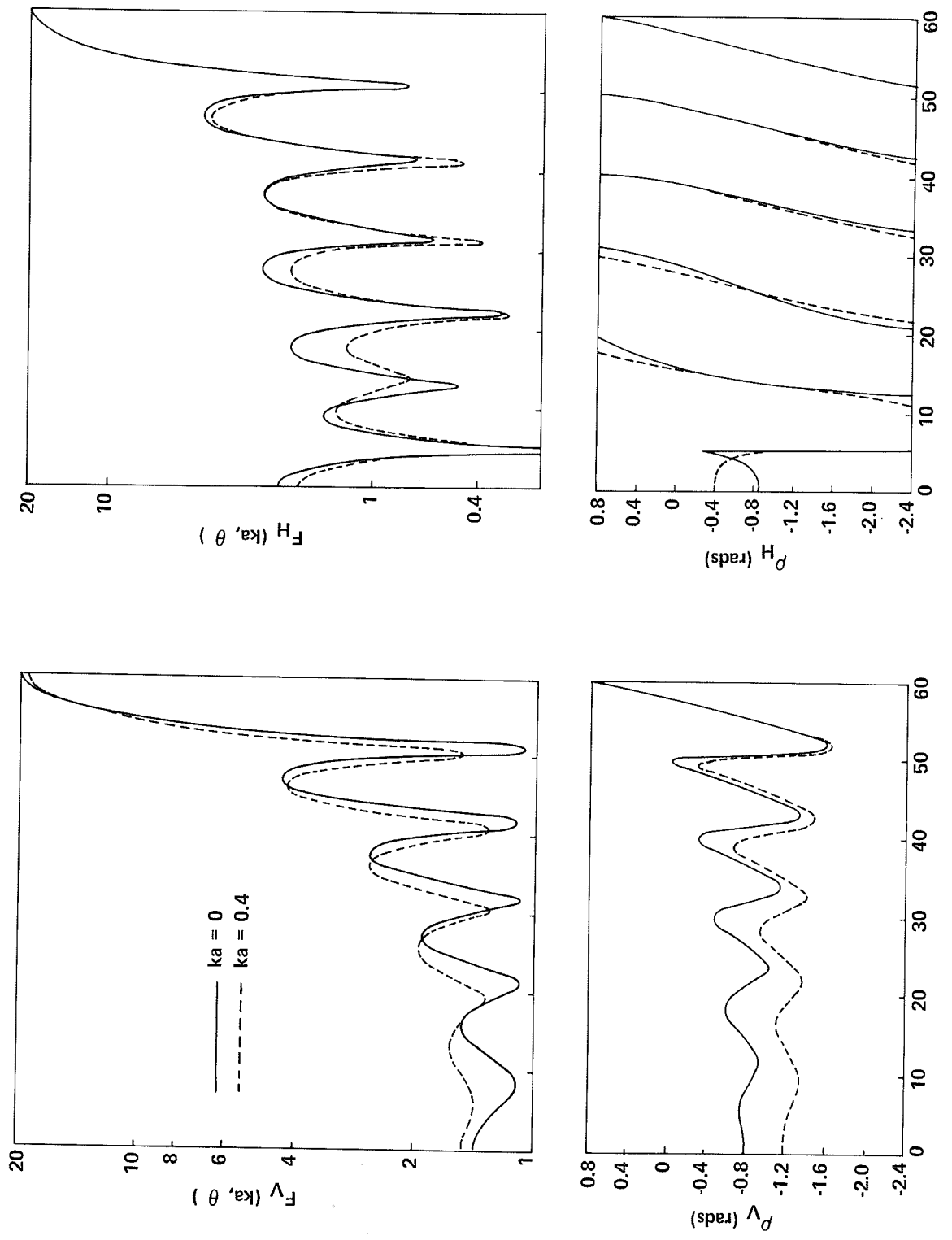

Figure 5.3 BACKSCATTERING FROM A MODIFIED EQUILATERAL TRIANGULAR PRISM. kL = 20. ka = 0, 0.4

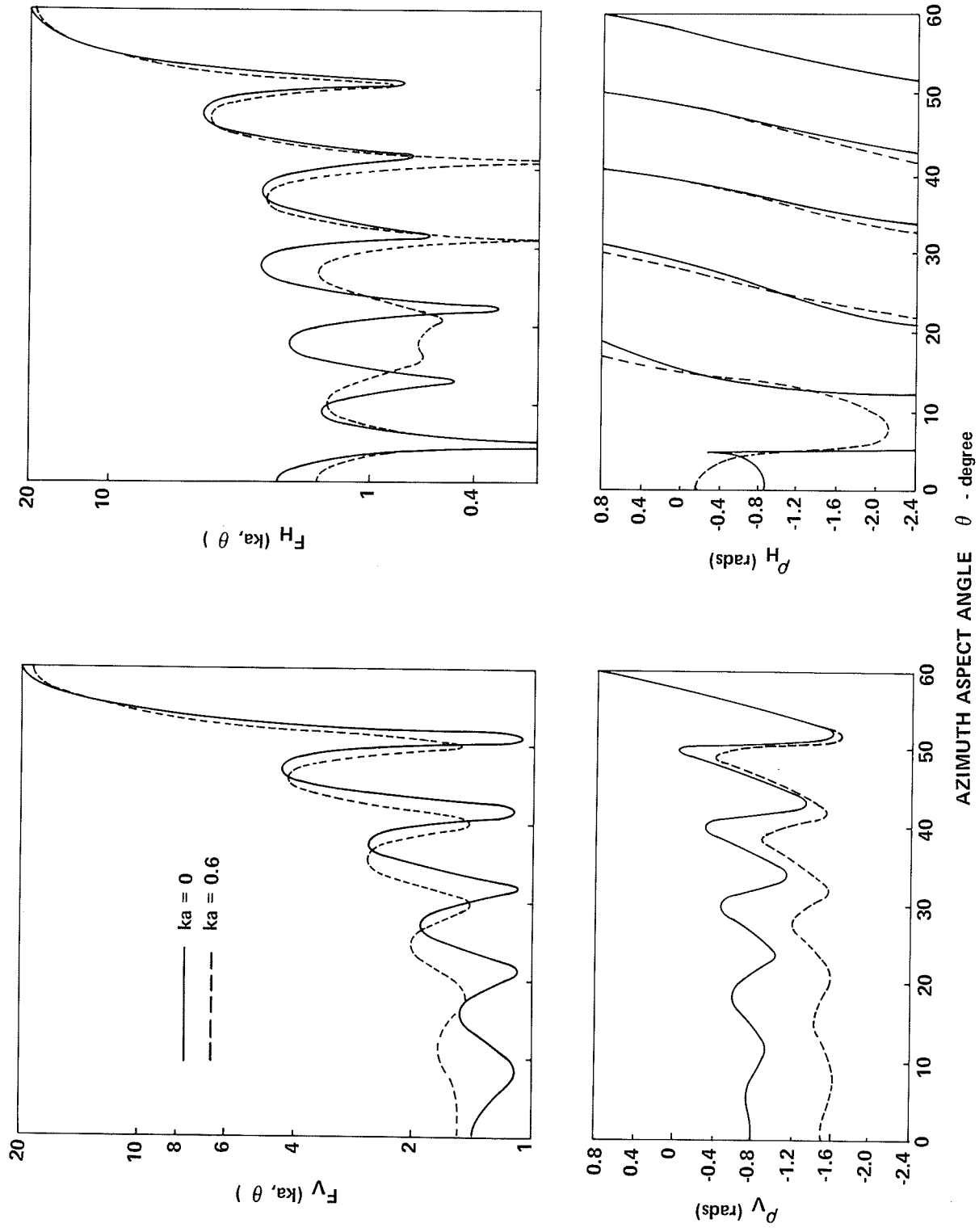

Figure 5.4 BACKSCATTERING FROM A MODIFIED EQUILATERAL TRIANGULAR PRISM. kL = 20. ka = 0, 0.6

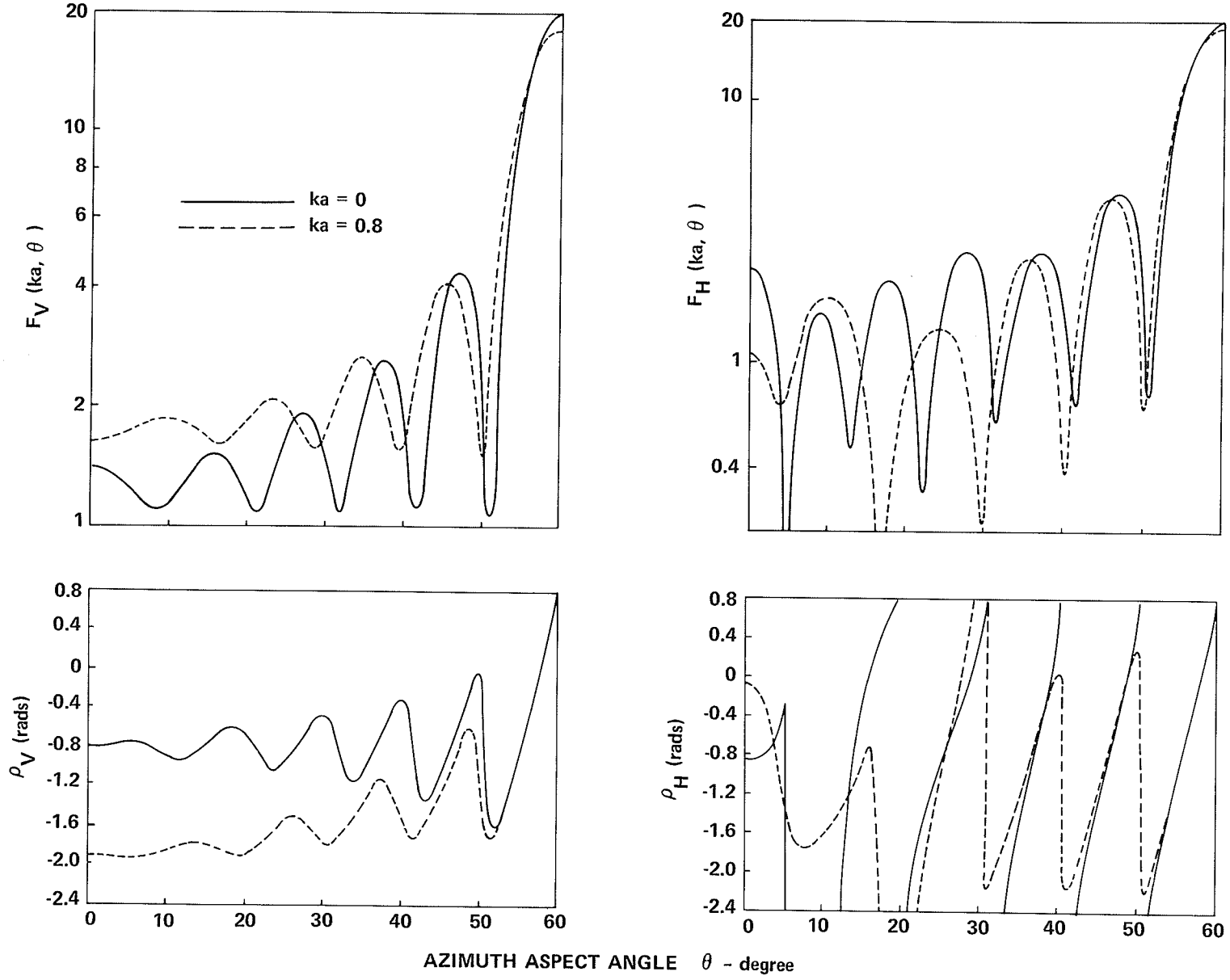

Figure 5.5 BACKSCATTERING FROM A MODIFIED EQUILATERAL TRIANGULAR PRISM. kL = 20. ka = 0, 0.8

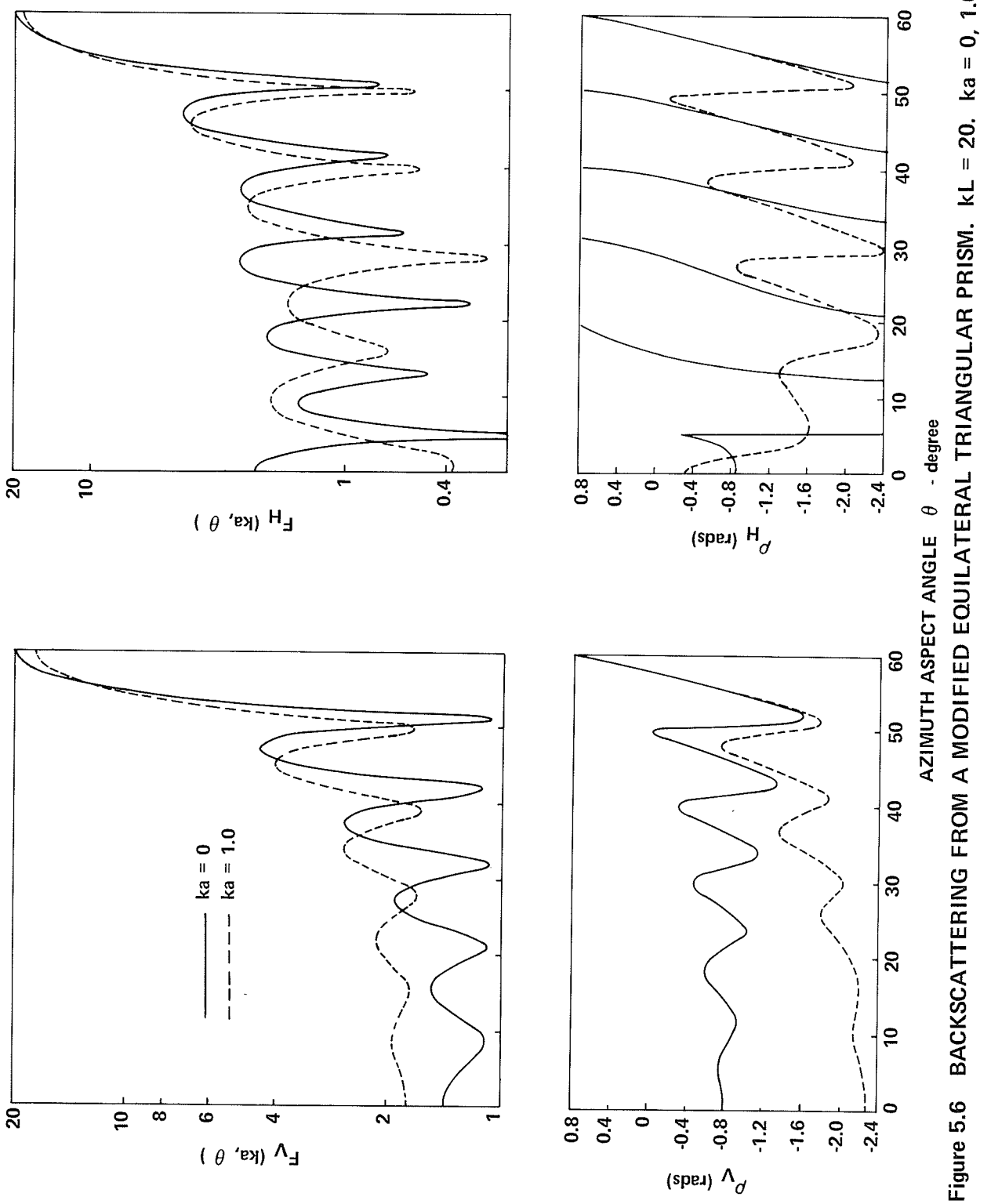

Figure 5.6 BACKSCATTERING FROM A MODIFIED EQUILATERAL TRIANGULAR PRISM. kL = 20. ka = 0, 1.0

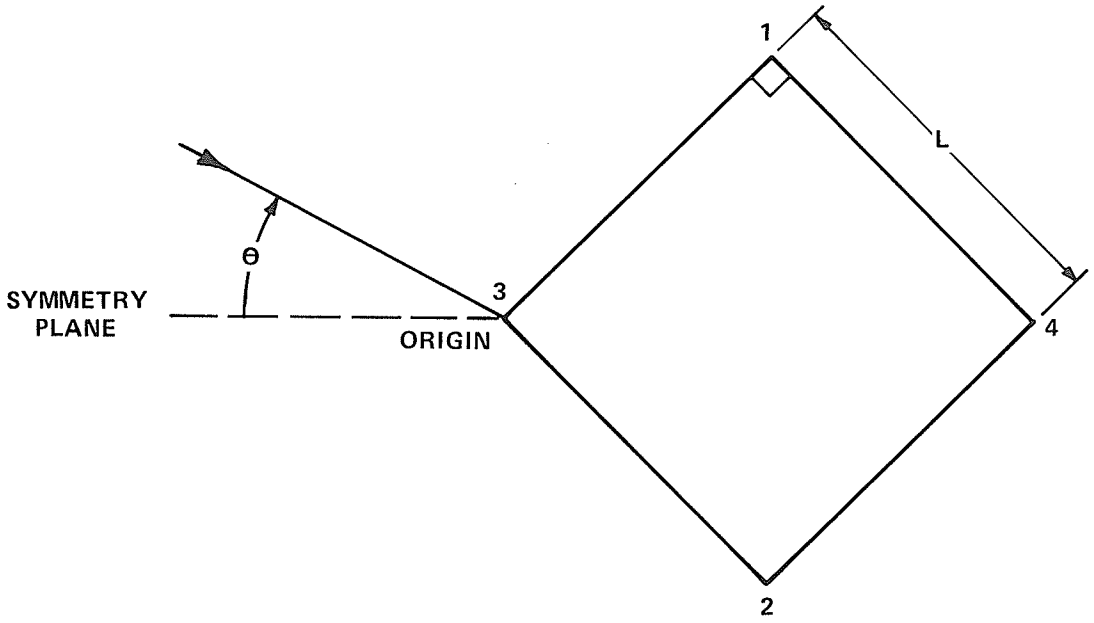

(a) REGULAR SQUARE PRISM

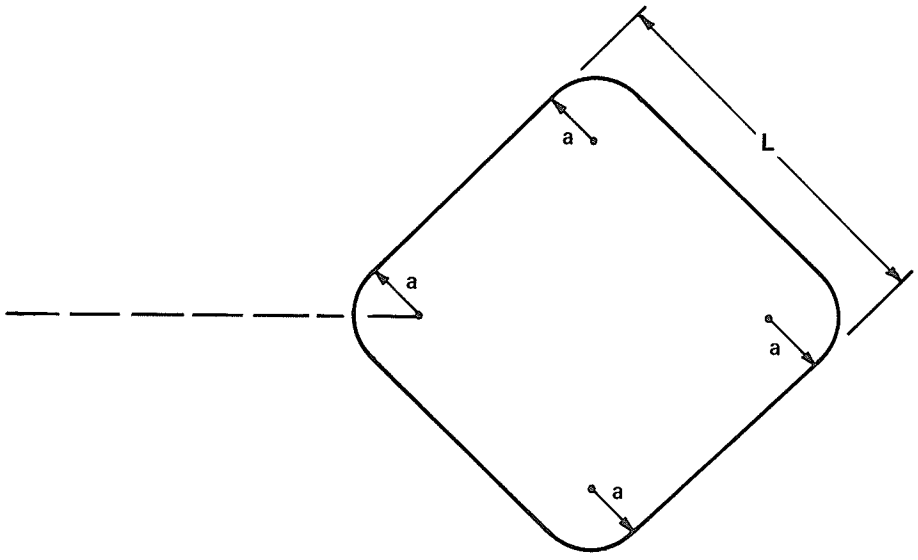

(b) MODIFIED SQUARE PRISM

Figure 5.7 REGULAR AND MODIFIED SQUARE PRISMS

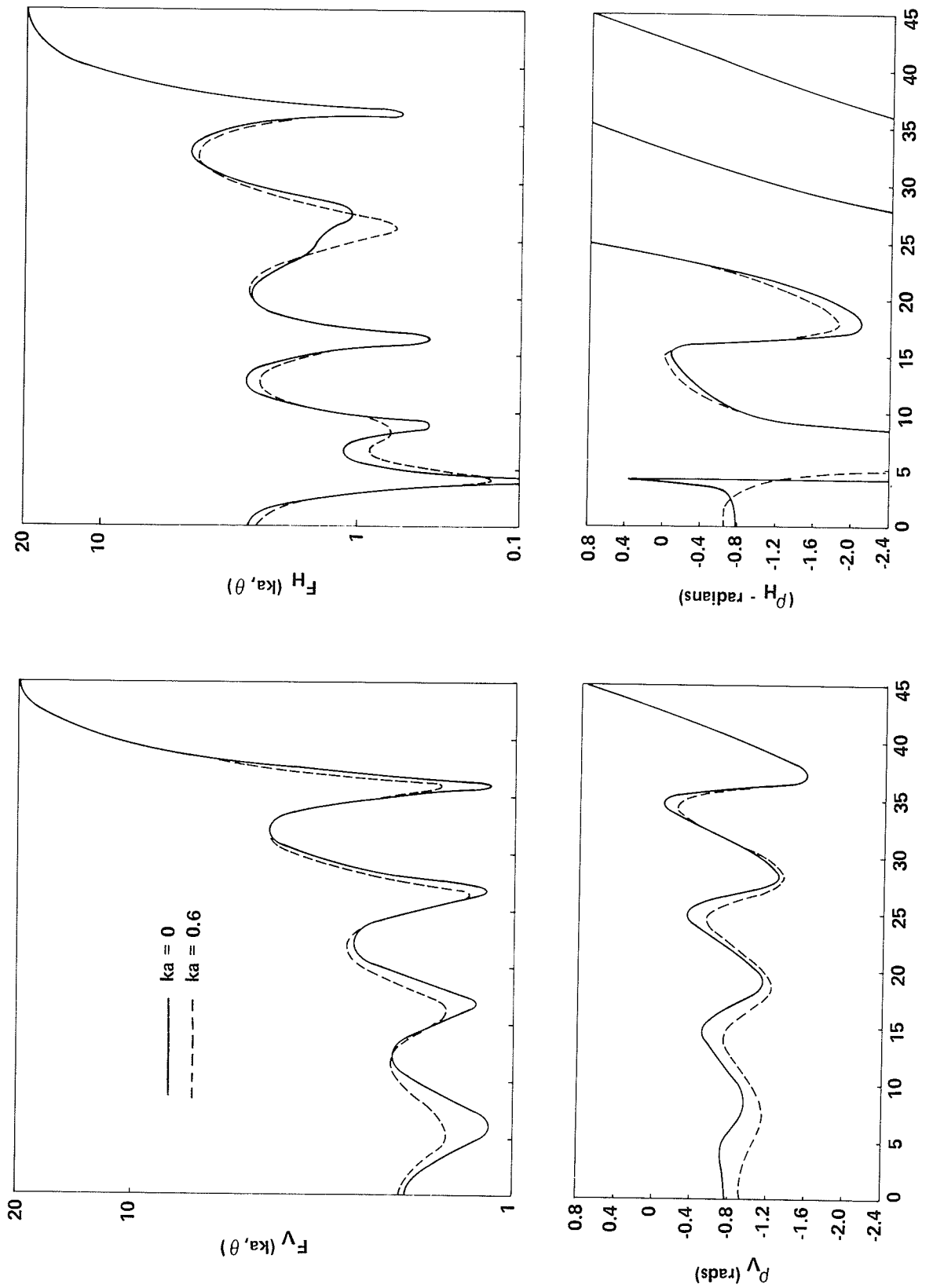

Figure 5.8 BACKSCATTERING FROM A MODIFIED SQUARE PRISM. kL = 20. ka = 0, 0.6

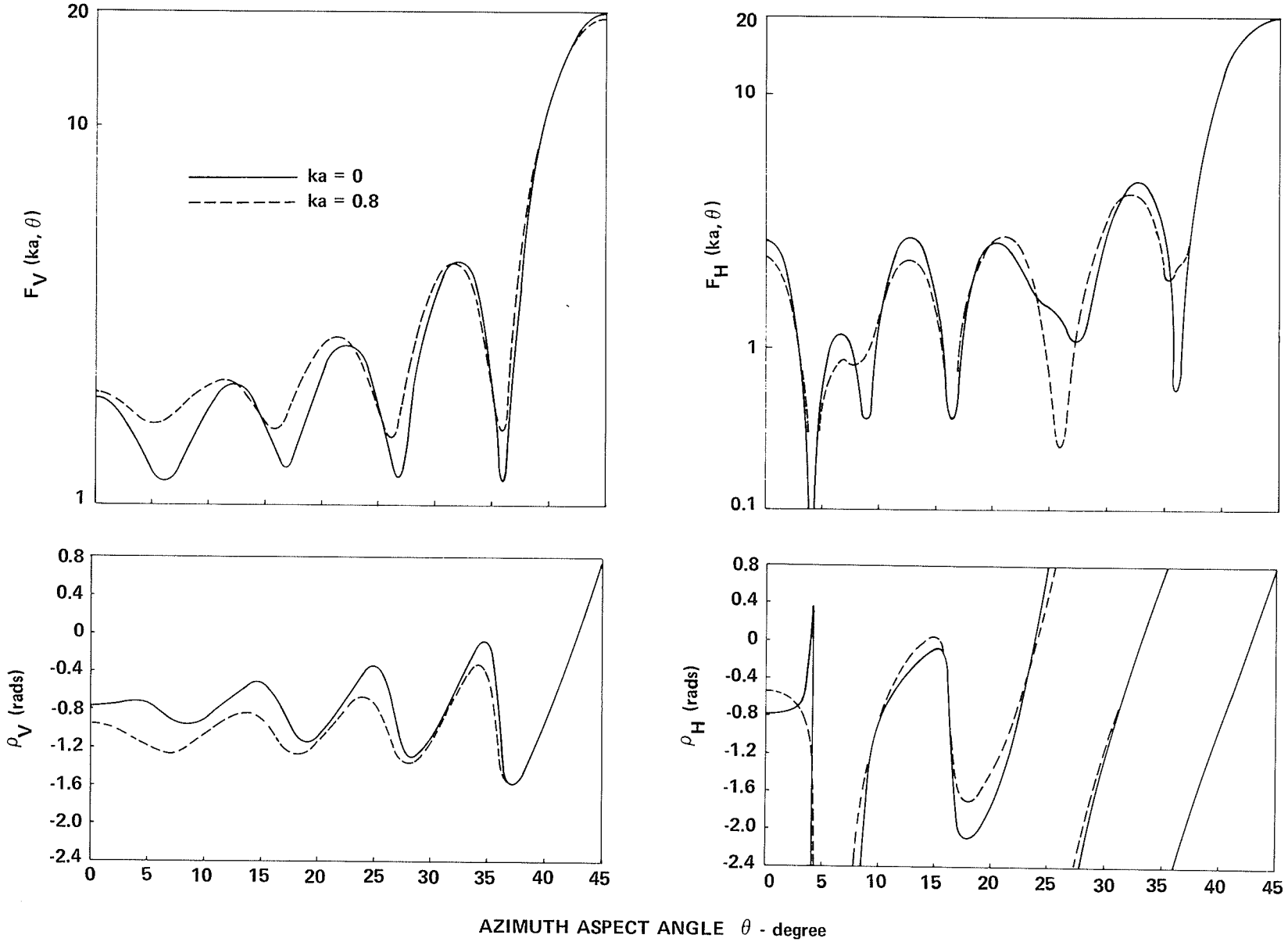

Figure 5.9 BACKSCATTERING FROM A MODIFIED SQUARE PRISM. kL = 20. ka = 0, 0.8

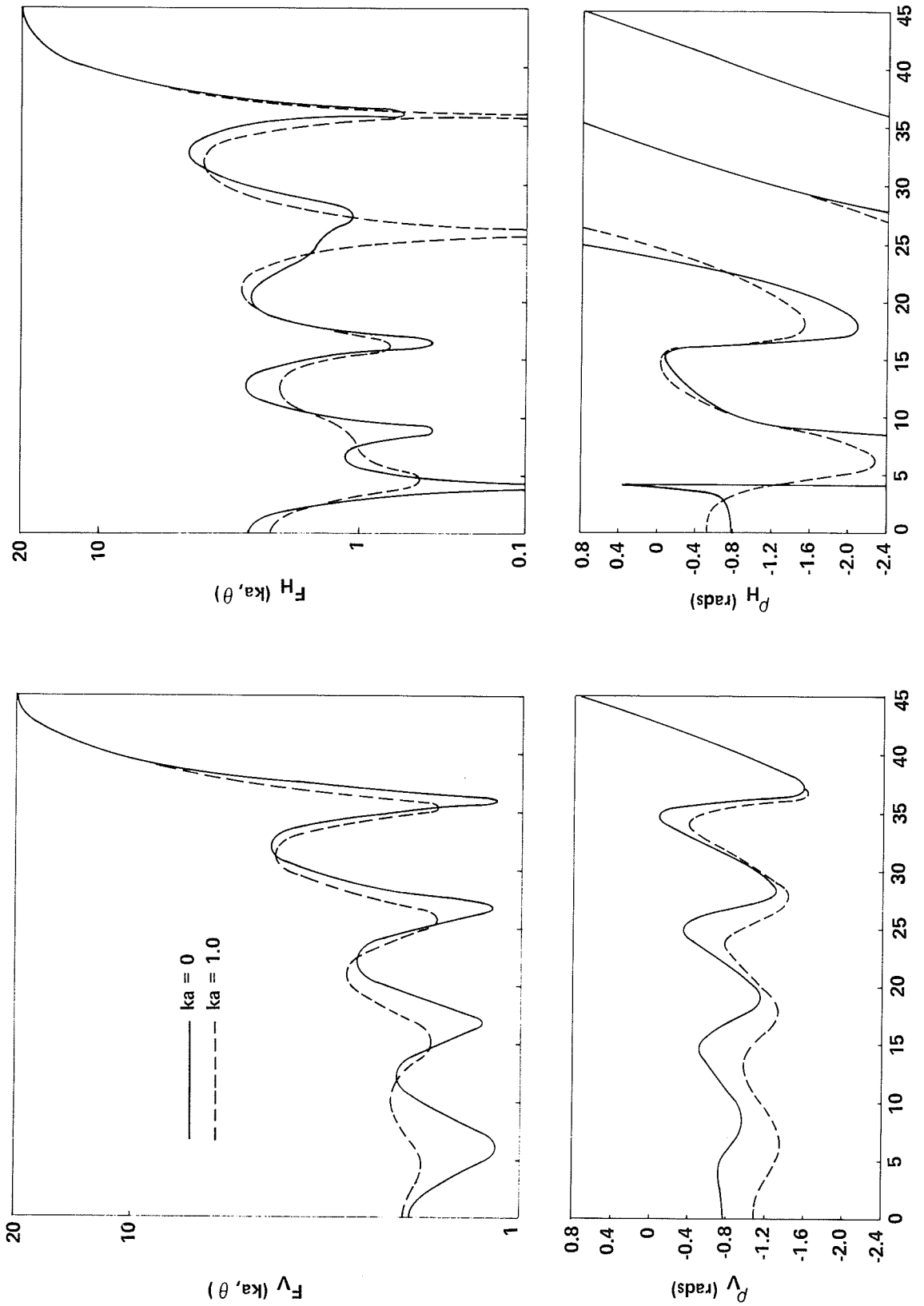

Figure 5.10 BACKSCATTERING FROM A MODIFIED SQUARE PRISM. kL = 20. ka = 0, 1.0

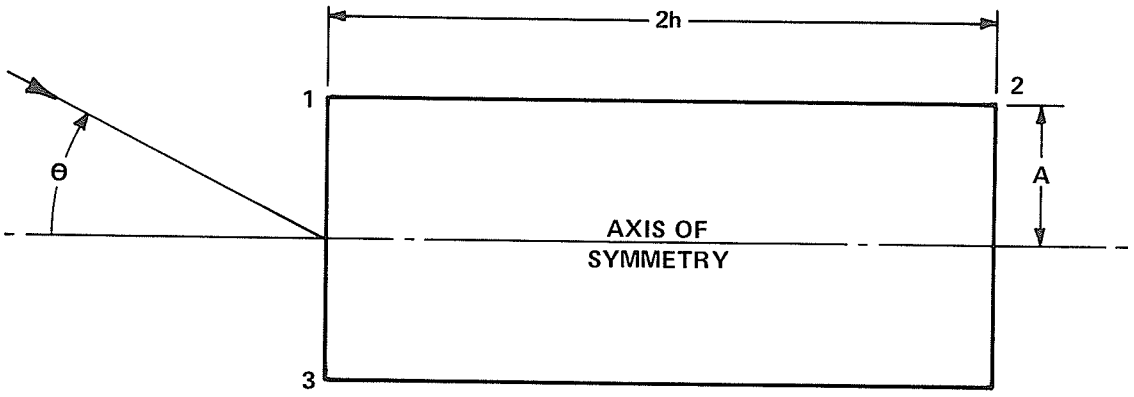

(a) REGULAR CYLINDER

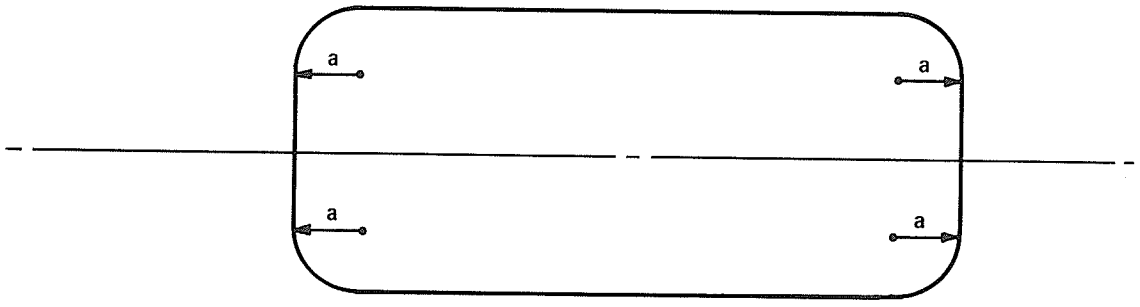

(b) MODIFIED CYLINDER

Figure 5.11 REGULAR AND MODIFIED FINITE, RIGHT-CIRCULAR CYLINDERS

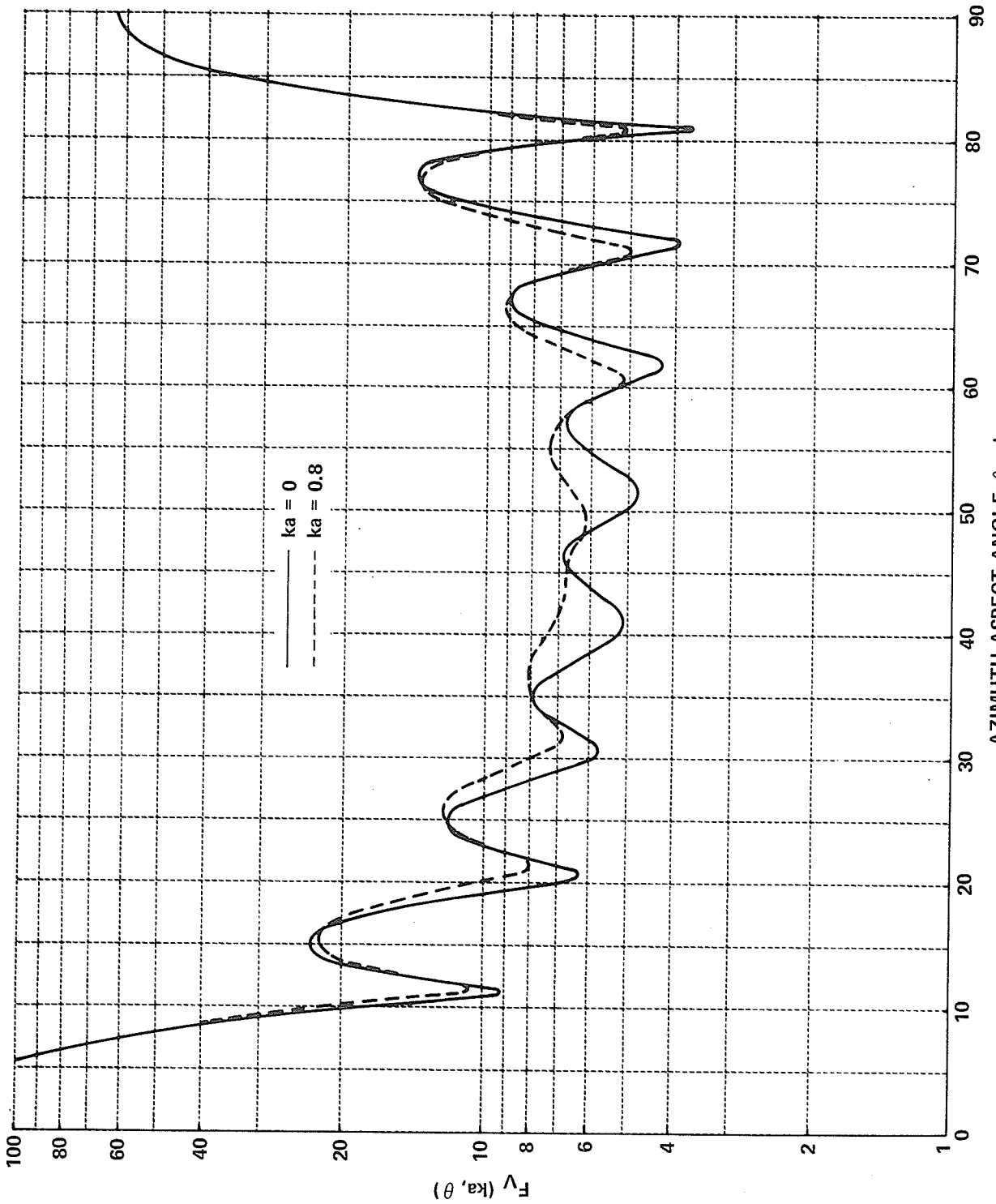

Figure 5.12 VERTICAL POLARIZATION BACKSCATTERING FROM A MODIFIED, FINITE, RIGHT-CIRCULAR CYLINDER. kh = kA = 10. ka = 0, 0.8

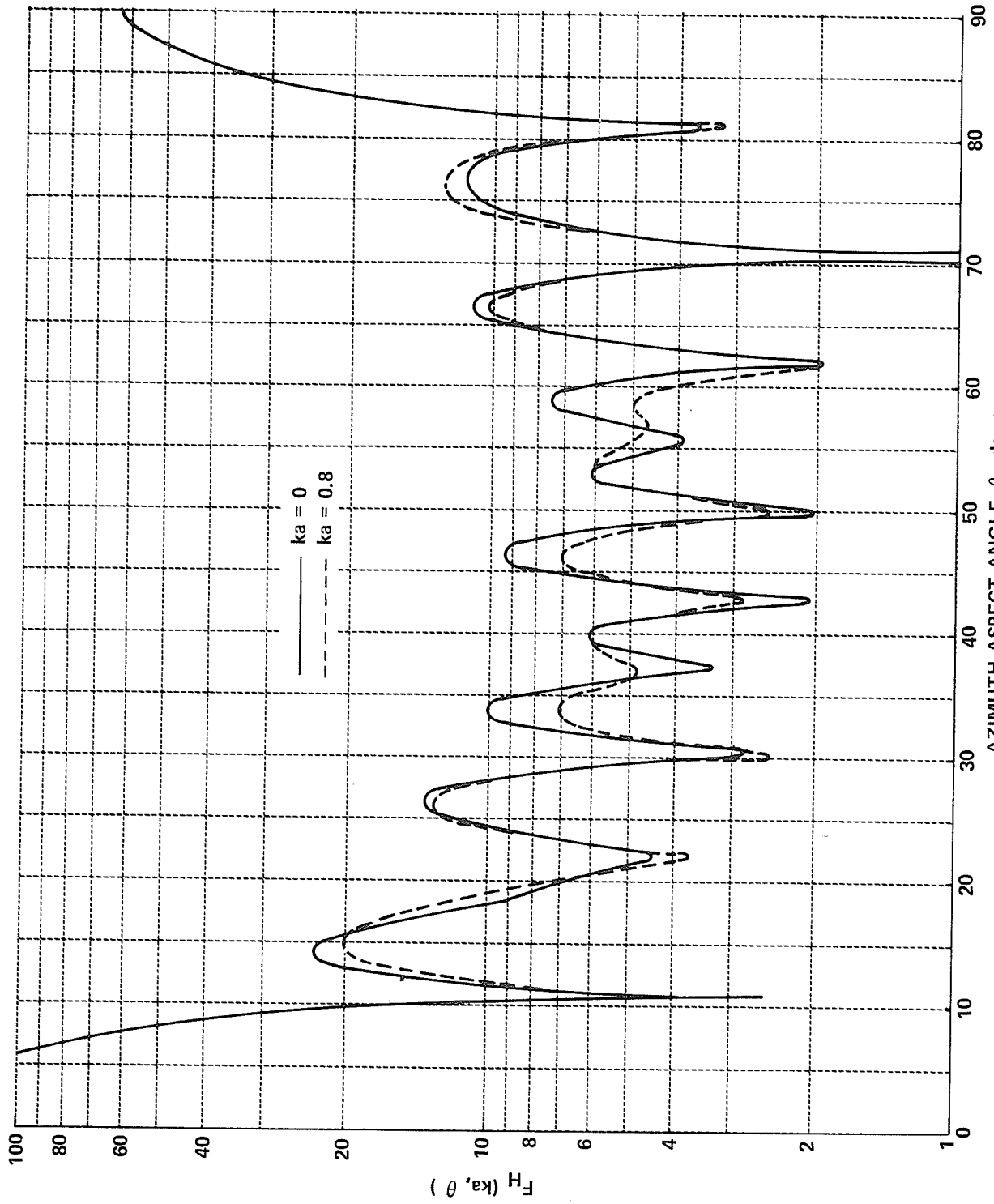

Figure 5.13 HORIZONTAL POLARIZATION BACKSCATTERING FROM A MODIFIED, FINITE, RIGHT-CIRCULAR CYLINDER. kh = kA = 10. ka = 0, 0.8

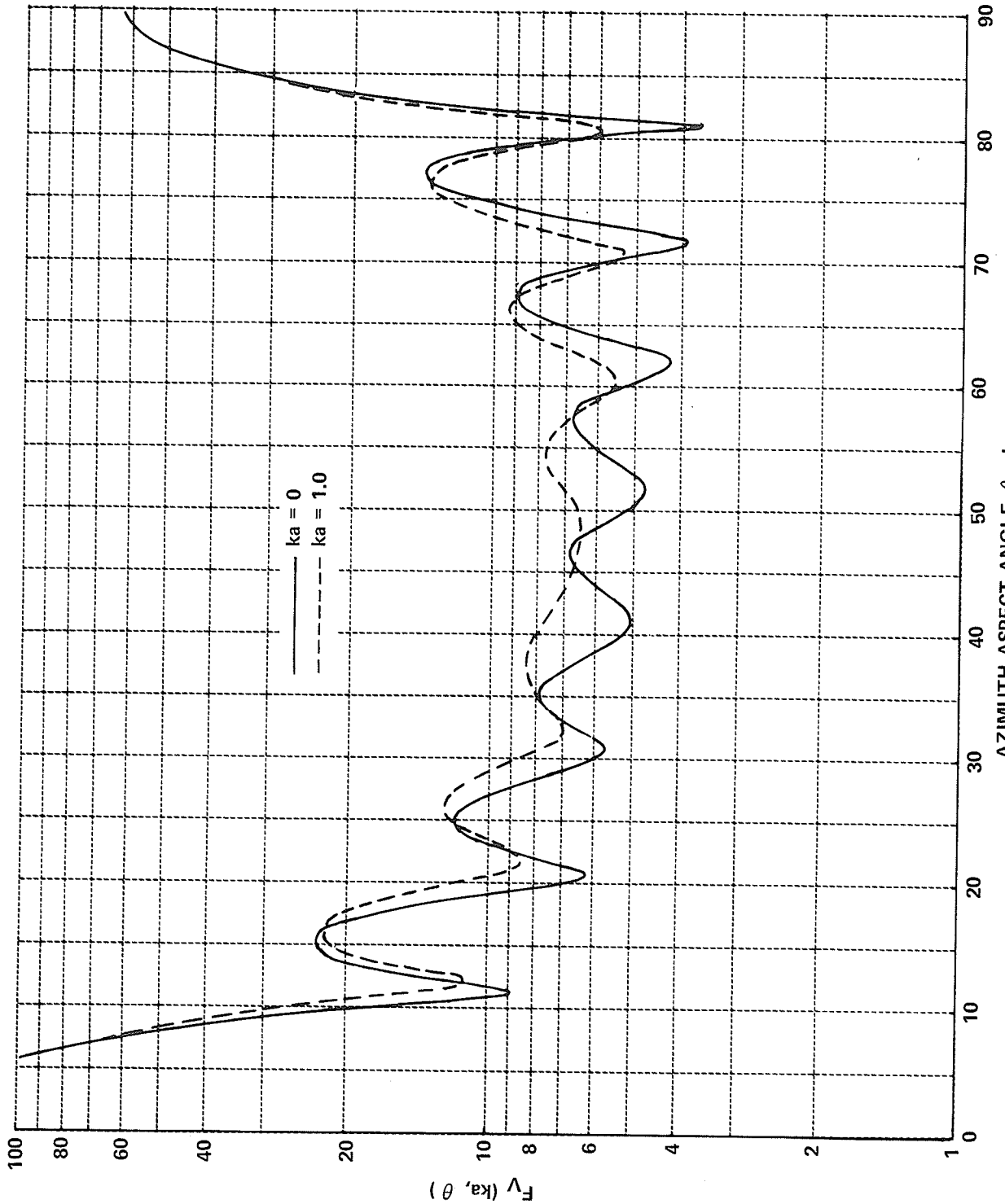

Figure 5.14 VERTICAL POLARIZATION BACKSCATTERING FROM A MODIFIED, FINITE, RIGHT-CIRCULAR CYLINDER. kh = kA = 10. ka = 0, 1.0

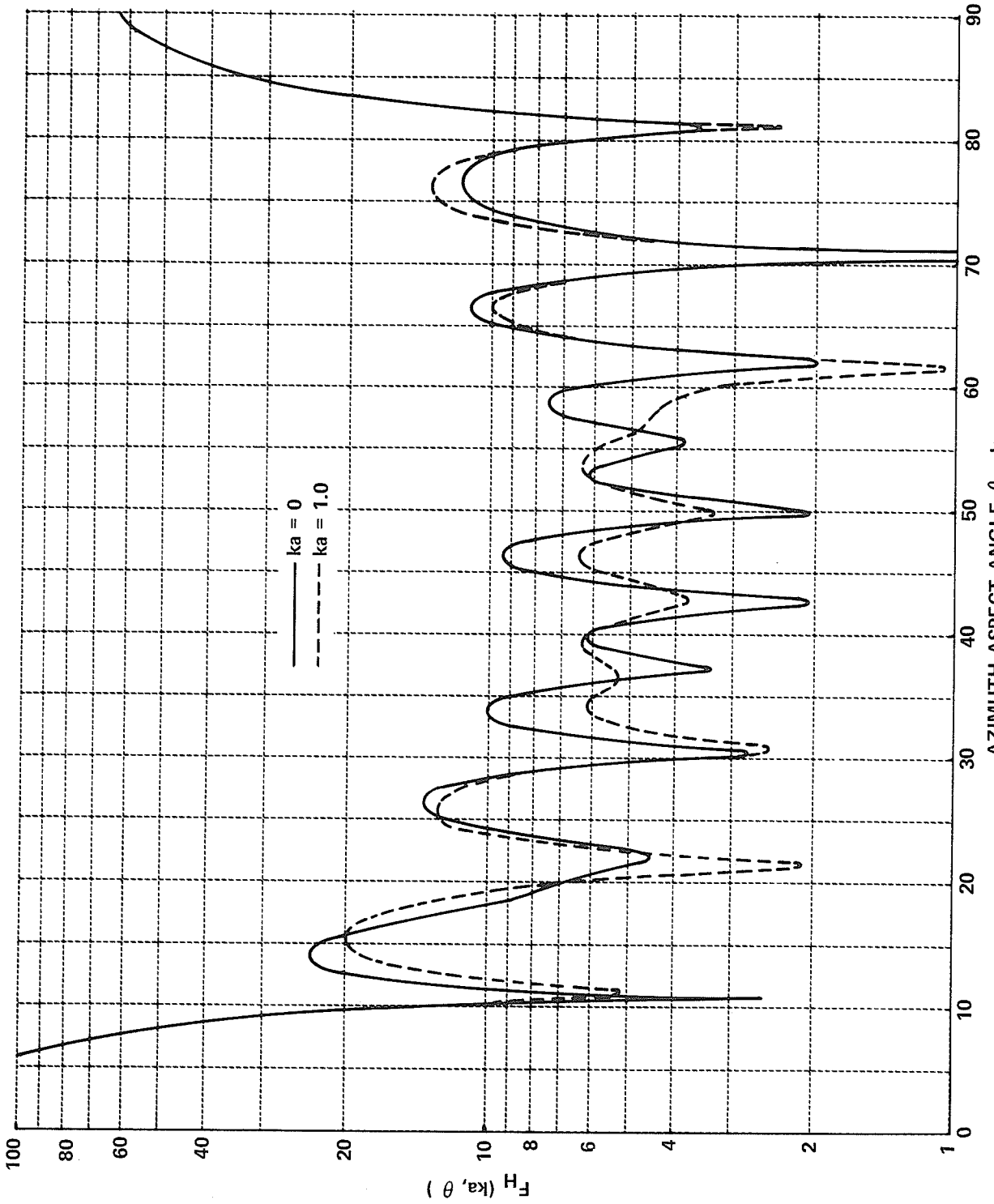

Figure 5.15 HORIZONTAL POLARIZATION BACKSCATTERING FROM A MODIFIED, FINITE, RIGHT-CIRCULAR CYLINDER. kh = kA = 10. ka = 0, 1.0

6. EXTENSION OF THE BOUNDARY VALUE SOLUTION FOR THE TRUNCATED WEDGE

6.1 Introduction

This chapter generalizes the boundary value approach introduced in Chapter 2. For convenience, discussion is limited to that class of obstacles formed upon modification of the tip of a semi-infinite wedge. Although scattering by more complex obstacles may be treated by this same technique, no attempt at all-inclusive coverage is intended.

The boundary value approach of Chapter 2 comprises three major steps:

(1) Formulate eigenseries expansions for the region I and II fields with unknown expansion coefficients.

(2) Apply the addition theorem to the region I fields to obtain a common coordinate origin.

(3) Solve a set of simultaneous equations for the region I expansion coefficients and then compute the scattered field in region II.

Implicit in step (1) above is a prior knowledge of valid eigenseries expansions for both the region II contour (including the matching boundary) and the region I contour. Despite this restriction, many problems can be analyzed using the above generalization.

In Section 6.2 we discuss targets made up from combinations of cylinder and wedge sections. Within the confines of scattering center theory, the most interesting of the new geometries is the truncated wedge. The analysis in Chapter 2 is easily altered in Section 6.3 to apply to the truncated wedge, and backscattering data for 60°, 90° and 120° wedges are presented. In Section 6.4, geometrical diffraction theory is applied to

the truncated wedge in a form suited to strong interaction between edge scattering centers. The capability of approximate theory is evaluated by comparison with boundary value calculations for symmetric incidence on wedges having various degrees of truncation. An improvement over present approximate theory is suggested which incorporates the exact solution for a wedge in the description of interaction terms. Finally, suggestions for future research are presented in Section 6.5 within the context of Hunter's detailed investigation of scattering by a truncated wedge.

6.2 Modified Wedges

The generalized boundary value approach of Section 6.1 has direct application to cylinder-wedge and wedge-wedge combinations. Representative examples are discussed next to illustrate the scope of application.

6.2.1 Cylinder-Wedge Combinations

Chapter 2 contains a specific application of the boundary value approach for tip configurations ranging from the wedge with cylindrical tip to the wedge with rounded edge. Fig. 6.1(a) depicts the situation when the cylindrical tip is assigned an intermediate location. Given the wedge half angle α, the cylinder radius a_2, and the separation distance $d_2 (0 \le d_2 \le \alpha_1)$, we compute the radius to the matching boundary using

$$R = \sqrt{a_2^2 + d_2^2 + 2a_2 d_2 \cos\left(\alpha + \sin^{-1}\left[\frac{d_2 \sin\alpha}{a_2}\right]\right)} \qquad (6.1)$$

Then the analysis of Chapter 2 (given in (2-26), (2-29), (2-44) and (2-45)) applies without modification provided $d_2 > R$. For intermediate locations corresponding to $d_2 < R$, we interchange the roles of d and R in the

addition theorem (2-7) and project this change into relations used for computations. Finally, we notice that the limiting behavior of our solution is proper. As the separation distance d_2 approaches zero, R approaches a by (6.1), and the region I expansion coefficients (d_p, f_p, D_p and F_p) approach zero. Thus we recover the solution for a wedge with cylindrical tip of radius a.

The derivation in Chapter 2 also applies without modification when the cylinder radius exceeds that corresponding to the rounded edge. In Fig. 6.2(b), parameters a_1, d_1 denote a rounded edge and the larger pair a_2, d_2 give rise to a discontinuity in the normal to the surface at the join. Notice that R is calculated as if the edge were rounded (using a_1 and d_1). Choosing a value for separation so that $d_2 > d_1$ and computing the cylinder radius using

$$a_2 = \sqrt{d_2^2 + R^2 - 2 d_2 R \cos\alpha} \qquad (6.2)$$
$$> a_1$$

we may apply the final results of Chapter 2 directly.

Next consider the situation in which the radius of the cylinder is less than that value corresponding to the wedge with rounded edge. In Fig. 6.1(c), R and d_1 remain parameters associated with the wedge with rounded edge. The reduced radius of the cylinder is chosen such that $a_2 < d_1 \tan\alpha_1$. There it is necessary to alter the eigenvalues in the expansion for the region I fields. Specifically, $p \to \frac{p\pi}{\gamma_2}$ in (2.5) and (2.32) where $\gamma_2 = (2\pi - 2\alpha_2)/\pi$. Of course relations based upon these initial equations will also require alteration, but the proper form of the final result can be obtained by inspection.

6.2.2 Wedge-Wedge Combination

The generalization of Section 6.1 also has utility when the region I contour includes a section of a wedge. Fig. 6.2 depicts an interior wedge with half angle α_2. For $\alpha_2 > \alpha_1/2$, this wedge section exhibits the proper "interior" character. To obtain a valid expansion for region I fields, we introduce general expansion coefficients in the known eigenseries expansion for a wedge with half-angle α_2. Again care must be exercised in applying the addition theorem in cases where $d < R$.

Allowing α_2 to increase to $\pi/2$ results in a truncated wedge. This particular configuration will be analysed in Section 6.3. Further increase in α_2 leads to a wedge with notched edge.

6.2.3 Further Applications

Modified wedges discussed in Subsections 6.2.1 and 6.2.2 contain a plane of symmetry. However, the addition theorem allows arbitrary translation of circular cylindrical waves. This means that the generalized boundary value approach applies to asymmetrically modified wedges. Fig. 6.3 provides an illustration based upon the wedge-wedge combination. This problem can be solved in the same manner as the symmetrical case (see Subsection 6.2.2).

In three dimensions, the sphere and cone correspond to the cylinder and wedge, respectively. By introducing the addition theorem for spherical Bessel functions,[65] known boundary value solutions for the sphere and cone can be manipulated to provide a solution for the cone with modified tip. Both sphere-cone and cone-cone combinations can be treated. Because of the complexity of the component boundary value

solutions, one can anticipate increased difficulty in three-dimensional problems.

6.3 Boundary Value Solution for the Truncated Wedge

In this section we apply boundary value theory to the truncated wedge and report findings on the behaviour of scattered fields under plane wave excitation. The present formulation is easily constructed by paralleling the derivation contained in Chapter 2.

Fig. 6.4 depicts a two-dimensional, semi-infinite, perfectly conducting wedge with truncated tip. Once the wedge half angle α and truncation length L are chosen, the separation d between coordinate origins is given by

$$d = \frac{L}{2} \cot \alpha \tag{6.3}$$

while the circular cylindrical matching boundary (R, ϕ) is determined by

$$R = \frac{L}{2} \csc \alpha \; ; \qquad \alpha \leq \phi \leq 2\pi - \alpha . \tag{6.4}$$

Eigenseries expansions for region II and III fields remain those chosen in Chapter 2 (see (2.3), (2.4), (2.30), (2.31), (2.13) and (2.14)). In region I we satisfy the boundary conditions on the conductor using the expansion for a half-space. Set γ_2 equal to 1 in the wedge solution for electric line source exitation to obtain

$$E_z^I(\rho,\theta) = -\frac{k^2 I_o}{4\omega\epsilon} \sum_{p=1}^{\infty} J_p(k\rho) H_p(k\rho_o) \left[d_p \sin\frac{p\pi}{2} \cos p\theta + f_p \cos\frac{p\pi}{2} \sin p\theta \right] \tag{6.5}$$

Normalizing the expansion coefficients with respect to $\sin\frac{p\pi}{2}$, $\cos\frac{p\pi}{2}$ we can rewrite (6.5) as

$$E_z^I(\rho,\theta) = -\frac{k^2 I_o}{4\omega\epsilon}\sum_{p=i}^{\infty} J_p(k\rho)H_p(k\rho_o)\left[\alpha_p \cos p\theta + f_p \sin p\theta\right]$$

$$\alpha_p = 0\,;\ p \text{ even} \qquad (6.6)$$

$$f_p = 0\,;\ p \text{ odd}$$

When the line source of Fig. 6-4 is a magnetic filament, we have

$$H_z^I(\rho,\theta) = -\frac{k^2 K_o}{4\omega\mu}\sum_{p=0}^{\infty} J_p(k\rho)H_p(k\rho_o)\left[D_p \cos p\theta + F_p \sin p\theta\right]$$

$$D_p = 0\,;\ p \text{ odd} \qquad (6.7)$$

$$F_p = 0\,;\ p \text{ even}$$

This completes step (1) of Section 6.1.

In the application of the addition theorem to the observation coordinates (ρ,θ) of (6.6) and (6.7) above, there are no restrictions since the circular cylindrical functions are Bessel functions of the first kind, and p is an integer. Thus step (2) of Section 6.1 is accomplished upon direct use of (2.7).

The resulting far field expansions for plane wave incidence are obtained by paralleling the analysis of Sections 2.2 through 2.5. The end result of step (3) of Section 6.1 is found to be

$$\frac{E_z^s(r,\phi)}{E_z^i} \sim \frac{e^{-j(kr+\frac{\pi}{4})}}{(2\pi kr)^{1/2}} \left\{ \frac{\sin\frac{\pi}{\gamma}}{\gamma} \left[\frac{1}{\cos\frac{\pi}{\gamma} - \cos\frac{\phi+\phi_o-2\alpha}{\gamma}} - \frac{1}{\cos\frac{\pi}{\gamma} - \cos\frac{\phi-\phi_o}{\gamma}} \right] \right.$$

$$+ \frac{8j}{\gamma} \sum_{n=1}^{\infty} e^{j\frac{n\pi}{\gamma}} \frac{J_{\frac{n}{\gamma}}(kR)}{H_{\frac{n}{\gamma}}(kR)} \sin\left[\frac{n}{\gamma}(\phi-\alpha)\right] \sin\left[\frac{n}{\gamma}(\phi_o-\alpha)\right]$$

$$\frac{-4je^{jkd\cos\phi_o}}{\psi} \sum_{n=1}^{\infty} e^{j\frac{n}{2}\frac{\pi}{\gamma}} \frac{\sin\left[\frac{n}{\gamma}(\phi-\alpha)\right]}{H_{\frac{n}{\gamma}}(kR)} \times$$

$$\left. \sum_{p=1}^{\infty} \sum_{q=-\infty}^{\infty} J_q(kR)\, J_{p+q}(kd) \left[d_p I_1 + f_p I_2 \right] \right\} \qquad (6.8)$$

$$\frac{H_z^s(k,\phi)}{H_z^i} \sim \frac{e^{-j(kr+\frac{\pi}{4})}}{(2\pi kr)^{1/2}} \left\{ \frac{\sin\frac{\pi}{\gamma}}{\gamma} \left[\frac{1}{\cos\frac{\pi}{\gamma} - \cos\frac{\phi+\phi_o-2\alpha}{\gamma}} + \frac{1}{\cos\frac{\pi}{\gamma} - \cos\frac{\phi-\phi_o}{\gamma}} \right] \right.$$

$$- \frac{4j}{\gamma} \sum_{n=0}^{\infty} \epsilon_n e^{j\frac{n\pi}{\gamma}} \frac{J'_{\frac{n}{\gamma}}(kR)}{H'_{\frac{n}{\gamma}}(kR)} \cos\left[\frac{n}{\gamma}(\phi-\alpha)\right] \cos\left[\frac{n}{\gamma}(\phi_o-\alpha)\right]$$

$$\frac{+2je^{jkd\cos\phi_o}}{\psi} \sum_{n=0}^{\infty} \epsilon_n e^{j\frac{n\pi}{2\gamma}} \frac{\cos\left[\frac{n}{\gamma}(\phi-\alpha)\right]}{H'_{\frac{n}{\gamma}}(kR)} \times$$

$$\left. \sum_{p=0}^{\infty} \sum_{q=-\infty}^{\infty} J'_q(kR)\, J_{p+q}(kd) \left[D_p I_3 + F_p I_4 \right] \right\} \qquad (6.9)$$

with the expansion coefficients determined by

$$\sum_{p=1}^{\infty}\sum_{q=-\infty}^{\infty}\left[J_q(kR)\frac{H_m'}{\gamma}(kR)-J_q'(kR)\frac{H_m}{\gamma}(kR)\right]J_{p+q}(kd)\left[d_p I_1+f_p I_2\right] \tag{6.10}$$

$$=-\frac{4j}{kR}\sin\left[\frac{m}{\gamma}(\phi_o-\alpha)\right]e^{-j\left(kd\cos\phi_o-\frac{m\pi}{2\gamma}\right)}$$

$$\sum_{p=0}^{\infty}\sum_{p=-\infty}^{\infty}\left[J_q(kR)\frac{H_m'}{\gamma}(kR)-J_q'(kR)\frac{H_m}{\gamma}(kR)\right]J_{p+q}(kd)\left[D_p I_3+F_p I_4\right] \tag{6.11}$$

$$=-\frac{4j}{kR}\cos\left[\frac{m}{\gamma}(\phi_o-\alpha)\right]e^{-j\left(kd\cos\phi_o-\frac{m\pi}{2\gamma}\right)}$$

and

$$d_p = F_p = 0;\ p \text{ even}$$
$$f_p = D_p = 0;\ p \text{ odd} \tag{6.12}$$

In (6.8) through (6.11) above, ϵ_n is the Neumann number, $\psi=\pi\gamma$ and I_1 through I_4 are given by (2.20), (2.21), (2.39) and (2.40).

It is interesting to note that the solution for the wedge with rounded edge can be manipulated to produce the above solution for the

truncated wedge. Taking the final results of Chapter 2 and introducing the following modifications:

(1) Reinterpret α and R according to (6.3) and (6.4).

(2) Set the parameter a to zero.

(3) Enforce (6.12).

Then (2.26), (2.29), (2.44) and (2.45) reduce to (6.8) through (6.12). An a priori rationale for this procedure cannot be based upon geometrical continuity, but rather it arises from the relationship between eigenseries expansions assigned to the fields in region I.

To maintain uniformity of presentation, we calculate the range-independent scattering pattern $F(kL, \varphi)$ for the truncated wedge, where φ is the azimuth aspect angle referred to a wedge face (i.e., $\varphi = \phi - \alpha$). Figs. 6.5 through 6.7 compare principal polarization values of $F(0, \varphi)$ with $F(kL, \varphi)$ as a function of φ for $2\alpha = 60°$, $90°$, $120°$ with $kL = 1$, 2 and 3, respectively. These backscattering data exhibit much the same gross characteristics as the rounded wedge data: When $\varphi > \frac{\pi}{2}$ truncation causes an increase in the sharp wedge result due to the flat-surface specular; when $\varphi < \frac{\pi}{2}$, scattering decreases since the return from an illuminated edge decreases with increasing wedge angle. However, interactions are appreciable for horizontal polarization and increase in kL can allow phasing which can negate the latter behaviour. (This mechanism is becoming apparent in Fig. 6.7.)

The analysis and results of this section constitute a concrete illustration of the generality of the boundary value approach. Additional calculations based upon the boundary value solution are presented in the next section.

6.4 Geometrical Diffraction Theory Applied to the Truncated Wedge

The truncated wedge exhibits (edge) scattering centers whose re-radiation characteristics can be described by geometrical diffraction theory. When the truncation length KL is less than 6, one can expect considerable interaction between edge scattering centers. Thus the boundary value solution of Section 6.3 is suited to evaluation of the ray mechanism of interaction.

6.4.1 Ray Formulations

In a ray theory formulation, the scattered field at the observation point, μ_{total}, is the sum of the fields on all rays passing through that point. Then the magnitude of the scattering pattern is given by

$$F_{RAY} = \sqrt{2\pi kr}\,\left|\mu_{TOTAL}\right| \tag{6.13}$$

The truncated wedge exhibits two scattering centers located at the upper and lower edges (see Fig. 6.8). The singly diffracted contribution μ_1 is due to diffraction of the incident energy by both edges in the direction of the receiver, i.e.,

$$\mu_1 = \mu_{U_1} + \mu_{U_2} \tag{6.14}$$

Higher order diffraction describes the interaction between scattering centers. For example, the doubly diffracted contribution is due to single diffraction at one edge in the direction of the other edge; at the second edge, the ray is again diffracted in the direction of the receiver.

Although there are an infinite number of diffracted rays, their contribution to the total field decreases with increasing order so that we can write

$$\mu_{TOTAL} = \sum_{n=1}^{\infty} \mu_n \tag{6.15}$$

Because of the repetitive nature of multiple diffraction, terms for $n > 3$ contain a power of the recurring complex factor χ which allows (6.15) to be expressed in closed form[26,11]

$$\mu_{TOTAL} = \mu_1 + \frac{\mu_2 + \mu_3}{1 - \chi} \tag{6.16}$$

Equation (6.16) is valid for $|\chi| < 1$ and requires evaluation of single, double and triple diffraction terms only.

In the evaluation of μ_1, μ_2, μ_3 and χ by geometrical diffraction theory, we choose a two-term diffraction coefficient to extend the prediction capability to small truncation lengths. This modified diffraction coefficient was derived previously by Mohsen and Hamid[66] for the half plane. Extending their result for wedge scattering we have

$$\mu_{U_1} = \frac{\sin\frac{\pi}{\gamma}}{\gamma\sqrt{2\pi kr}\,\gamma}\left\{\left[\left(\cos\frac{\pi}{\gamma} - \cos\frac{\pi+\theta+\theta_o}{\gamma}\right)^{-1} \mp \left(\cos\frac{\pi}{\gamma} - \cos\frac{\theta-\theta_o}{\gamma}\right)^{-1}\right]\right.$$
$$\left. + \frac{j}{4kr}\left[\left(\cos\frac{\pi}{\gamma} - \cos\frac{\pi+\theta+\theta_o}{\gamma}\right)^{-3} \mp \left(\cos\frac{\pi}{\gamma} - \cos\frac{\theta-\theta_o}{\gamma}\right)^{-3}\right]\right\} \times \tag{6.17}$$
$$e^{-j\left(k\left[s+\Psi\right]+\frac{\pi}{4}\right)}$$

$$\mu_{L_1} = \mu_{U_1}(r_1 - \theta_1 - \theta_o) \tag{6.18}$$

where

S = range dependent phase of diffracted ray

ψ = range dependent phase of incident ray.

Incidence and observation angles are referenced to the symmetry plane of the truncated wedge (see Fig. 6.8). (Fig. 6.8 also accounts for the simplicity of (6.18) which relates rays singly diffracted at upper and lower edges of the truncated wedge.) The upper and lower signs in (6.17) refer to vertical and horizontal polarizations, respectively. Finally, the correction term in (6.17), which is proportional to $r^{-3/2}$, does not affect the singly diffracted contribution to the scattered field; its inclusion upgrades the description of multiple diffraction only.

Equations (6.17) and (6.18) allow evaluation of the ray interaction model ((6.16) including equations of the form of (6.15)). Formulas specialized to symmetrical incidence backscattering are presented below. For the case of horizontal polarization, the ray method outlined above applies without modification.

$$F_{H(GOT)} = \left\{ \left[jkL + \frac{2\sin\frac{\pi}{\gamma}}{\gamma}\left(\cos\frac{\pi}{\gamma}-1\right)^{-1}\right] e^{-j\frac{\pi}{4}} \right.$$

$$+ \frac{1}{\sqrt{2\pi kL}}\left(\frac{2\sin\frac{\pi}{\gamma}}{\gamma}\right)^2 \left[\left(\cos\frac{\pi}{\gamma}-\cos\frac{\pi}{2\gamma}\right)^{-1} + \frac{j}{4kL}\left(\cos\frac{\pi}{\gamma}-\cos\frac{\pi}{2\gamma}\right)^{-3}\right] X \qquad (6.19)$$

$$\left. \frac{e^{-j\left(\frac{\pi}{2}+kL\right)}}{1-\frac{2\sin\frac{\pi}{\gamma}}{\sqrt{2\pi kL}\,\gamma}\left[\left(\cos\frac{\pi}{\gamma}-1\right)^{-1}+\frac{j}{4kL}\left(\cos\frac{\pi}{\gamma}-1\right)^{-3}\right] e^{-j\left(\frac{\pi}{4}+kL\right)}} \right\}$$

The first term in (6.19) describes the specular return from the truncation length due to singly diffracted rays, while the second term accounts for interactions between scattering centers. Here quantities in $L^{-3/2}$ represent a first-order correction to geometrical diffraction theory included to extend prediction capability for small truncation lengths.

For the case of vertical polarization, the ray method outlined above predicts zero interaction between scattering centers. Keller[67] has shown that the correct diffracted field is in this case proportional to the normal derivative of the incident field at the edge. This necessary alteration has been incorporated in the vertical polarization derivation to obtain

$$F_{V_{(GDT)}} = \left\{ \left[jkL - \frac{2\sin\frac{\pi}{\gamma}}{\gamma}\left(\cos\frac{\pi}{\gamma}-1\right)^{-1} \right] e^{-j\frac{\pi}{4}} - \frac{\frac{8e^{-jkL}}{\sqrt{2\pi}(kL)^{3/2}}\left(\frac{\sin\frac{\pi}{\gamma}\ \sin\frac{\pi}{2\gamma}}{\gamma^2\left(\cos\frac{\pi}{\gamma}-\cos\frac{\pi}{2\gamma}\right)^2}\right)^2\left(1+\frac{3j}{4kL}\left(\cos\frac{\pi}{\gamma}-\cos\frac{\pi}{2\gamma}\right)^{-2}\right)}{1-\frac{4\sin\frac{\pi}{\gamma}}{\sqrt{2\pi}\,\gamma^3(kL)^{3/2}}\left(\cos\frac{\pi}{\gamma}-1\right)^{-2}\left(1+\frac{3j}{4kL}\left(\cos\frac{\pi}{\gamma}-1\right)^{-2}\right)e^{j\left(\frac{\pi}{4}-kL\right)}} \right\} \qquad (6.20)$$

Again, singly diffracted rays describe the specular return in the first bracket and interactions between edges are represented by the second term. Quantities in $L^{-5/2}$ correspond to the first-order correction to geometrical diffraction theory. Comparing (6.19) and (6.20), it is apparent that the predicted interaction is stronger for horizontal polarization.

Figs. 6.9 through 6.11 allow evaluation of approximate theory by comparison with boundary value data. These plots show the magnitude of the symmetrical-incidence backscattering pattern as a function of truncation length for both principal polarizations. Examination of results for 60°, 90° and 120° wedges shows that $F_{H(GDT)}$ is accurate for $kL > 0.5$, 1.5 and 2.5, respectively. Prediction capability is poorer in the vertical polarization case where corresponding limits are $kL > 2$, 3 and 5, respectively.

6.4.2 Modification to Geometrical Diffraction Theory

It seems reasonable to consider whether the use of a three-term diffraction coefficient will lead to improved accuracy. This diffraction coefficient could be obtained by expanding relations presented in Ref. 67. On the other hand, it is possible to formulate an expression for interactions which includes all terms in the diffraction coefficient. The method is illustrated for the horizontal polarization case. We start with the exact solution for scattering by a wedge and apply it to the two scattering centers on the truncated wedge.

$$\mu_{exact_{U_1}} = \frac{2}{\gamma}\sum_{n=0}^{\infty} \epsilon_n j^{\frac{n}{\gamma}} \frac{J_n}{\gamma}(kr)\cos\left[\frac{n}{\gamma}\left(\frac{\pi}{2}+\theta\right)\right]\cos\left[\frac{n}{\gamma}\left(\frac{\pi}{2}+\theta_o\right)\right] \tag{6.21}$$

$$\mu_{exact_{L_1}}(r,\theta,\theta_o) = \mu_{exact_{U_1}}(r,-\theta,-\theta_o) \tag{6.22}$$

For single diffraction we retain (6.17) and (6.18). Multiple diffraction contributions involve the application of (6.24) and (6.22) above as well. Our result becomes

$$\left(F_{H_{GDT}}\right)_{mod.} = \left\{\left[jkL + \frac{2\sin\frac{\pi}{\gamma}}{\gamma}\left(\cos\frac{\pi}{\gamma}-1\right)^{-1}\right]e^{-j\frac{\pi}{4}}\right. \tag{6.23}$$

$$\left. + \frac{8\sin\frac{\pi}{\gamma}\, e^{-j\frac{\pi}{4}}}{\gamma^2}\left(\cos\frac{\pi}{\gamma}-\cos\frac{\pi}{2\gamma}\right)^{-1}\frac{\sum_{n=0}^{N}\epsilon_n j^{\frac{n}{\gamma}} J_{\frac{n}{\gamma}}(kL)\cos\left[\frac{n\pi}{2\gamma}\right]}{1-\frac{2}{\gamma}\sum_{n=0}^{N}\epsilon_n j^{\frac{n}{\gamma}} J_{\frac{n}{\gamma}}(kL)}\right\}$$

Equation (6.23) represents the limiting form of (6.19) in that it contains the complete r dependence for interaction. Thus the above results allows evaluation of the ray theory model for interaction.

6.5 Related Investigation of the Truncated Wedge

The truncated wedge has been chosen to illustrate the generality of the boundary value approach. Boundary value calculations were used to evaluate geometrical diffraction theory, and a modification to approximate theory has been formulated. Hunter[46] has performed a detailed investigation of scattering by a truncated wedge, and his findings are discussed below.

Hunter employed the Surface-Current-Replacement technique to generate accurate scattering data. He then evaluated the single and double diffraction form of geometrical diffraction theory (our (6.16) with $\mu_3 = \chi = 0$) in the bistatic case. For horizontal polarization, the objectionable singularity for forward scattering ($\theta = \theta_0 + \pi$) is observed. For vertical polarization, his interaction term is zero because he treats the field rather than the normal derivative of the field. To improve the approximation, Hunter first constructs a polarization dependent form of physical optics which shows improvement over conventional physical optics. Next Hunter applies the Iterative Surface-Current-Replacement technique to the truncated wedge. This method, which is "postulated" to be exact, leads to an integral form of the diffraction coefficient, and the resulting modification to geometrical diffraction theory no longer exhibits a forward scattering singularity. Hunter states that approximate theory for symmetrical incidence backscattering is now accurate for kL as low as 0.3.

Further work on the wedge with small truncation length should be performed within the context of Hunter's excellent modification to geometrical diffraction theory.

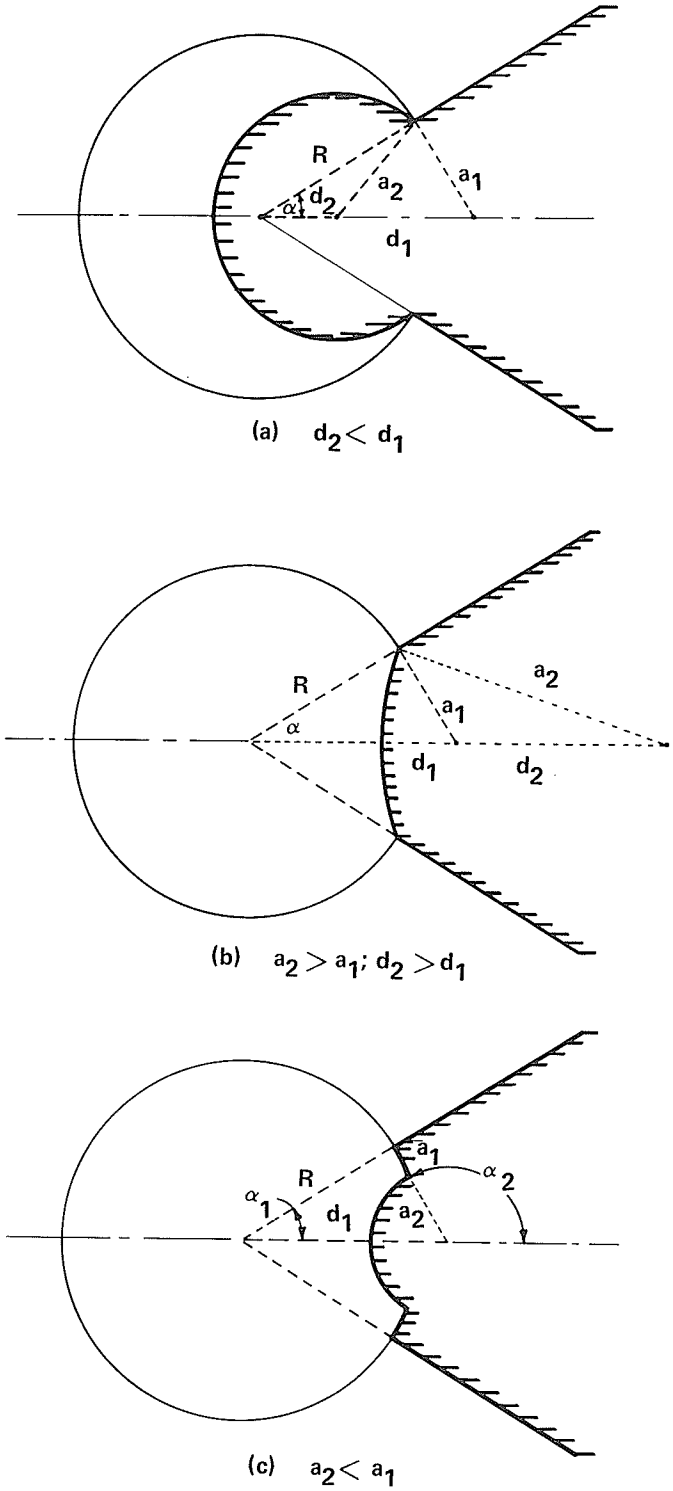

Figure 6-1 CYLINDER-WEDGE COMBINATIONS

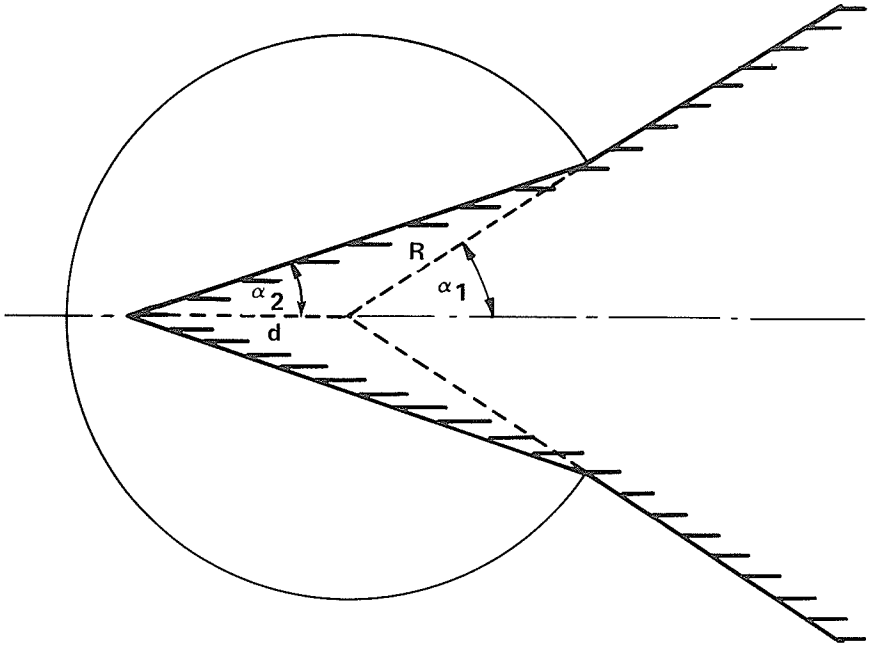

Figure 6.2 SYMMETRICAL WEDGE-WEDGE COMBINATION

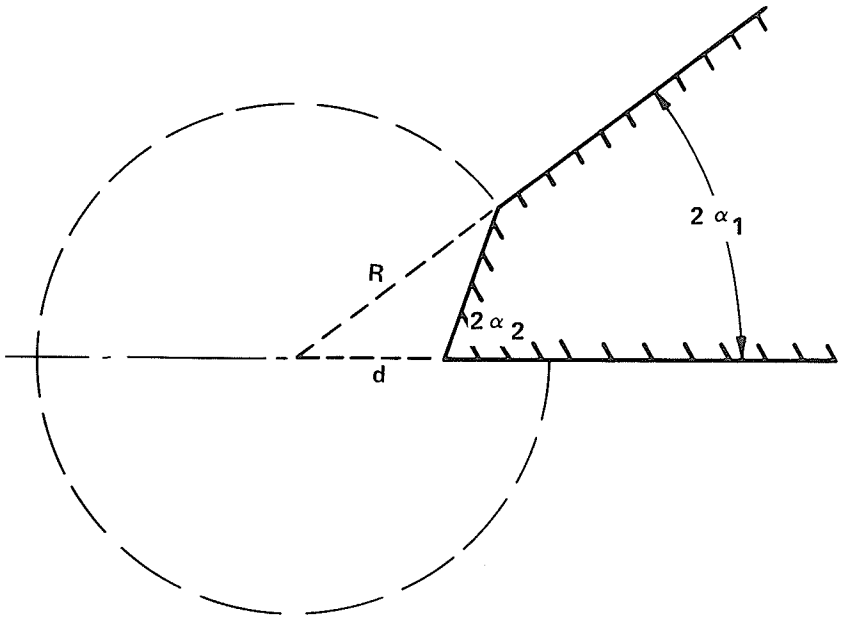

Figure 6.3 ASYMMETRICAL WEDGE-WEDGE COMBINATION

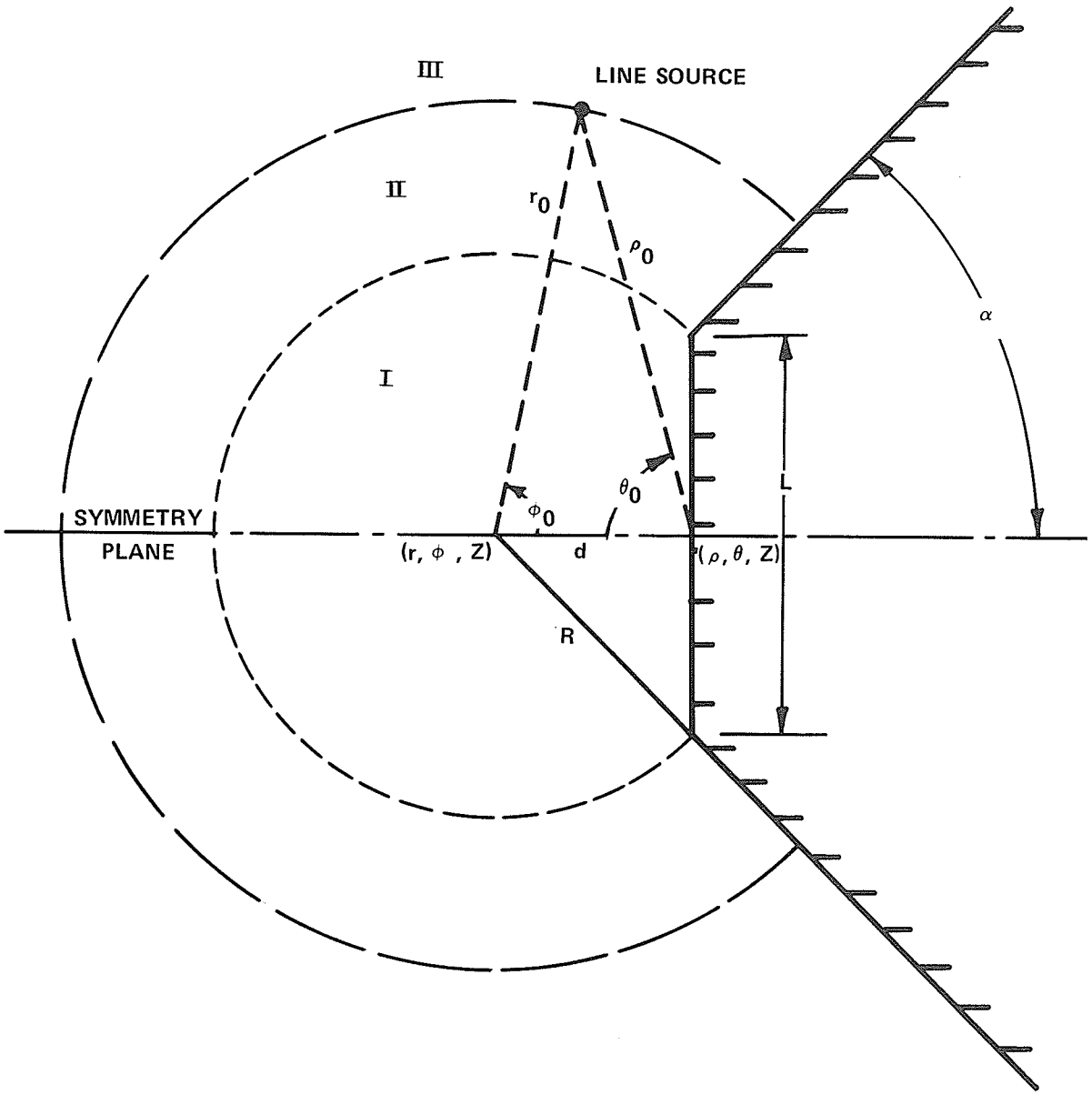

Figure 6.4 SCHEMATIC DIAGRAM OF TRUNCATED WEDGE UNDER LINE SOURCE EXCITATION

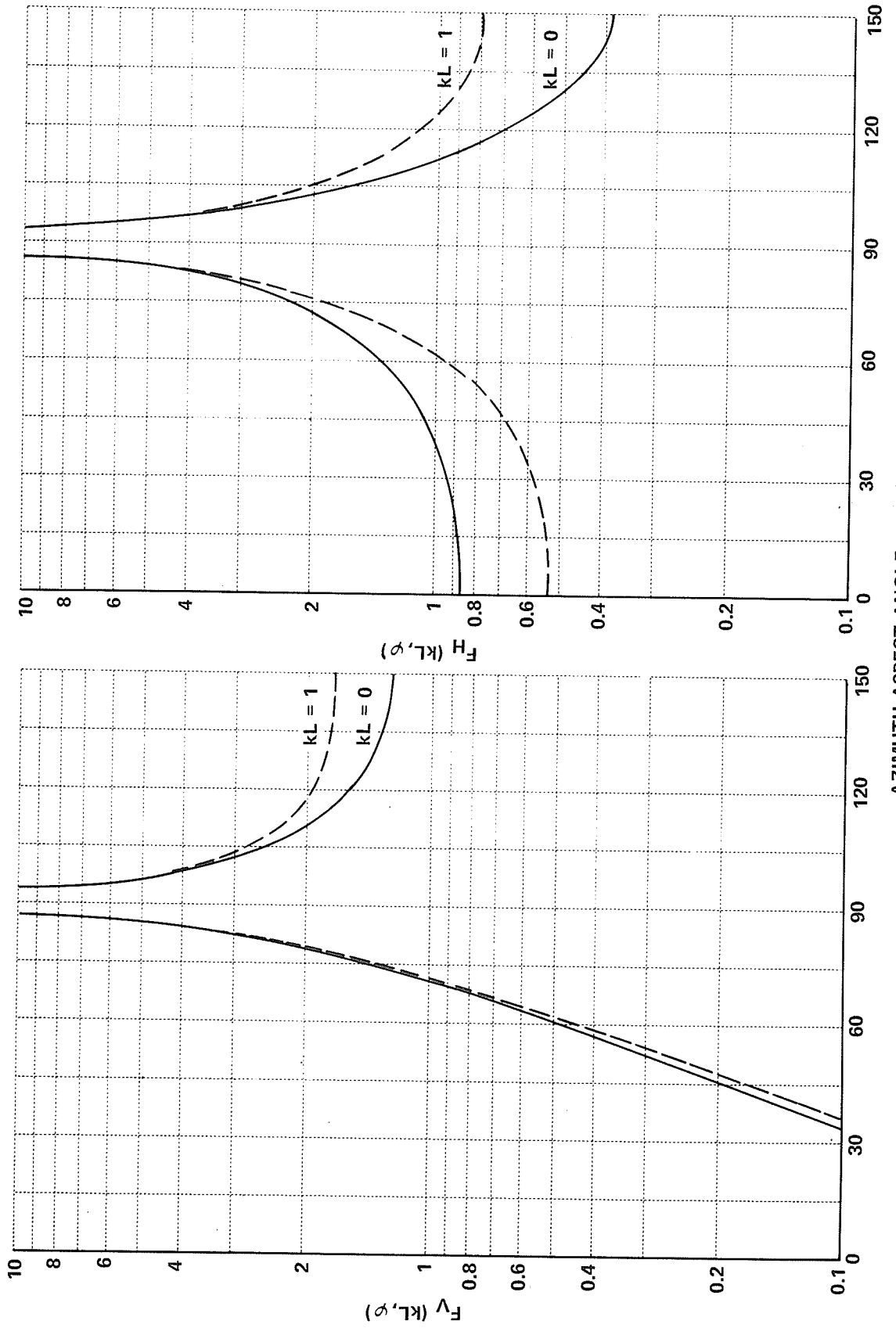

Figure 6.5 SCATTERING DATA FOR 60° TRUNCATED WEDGE

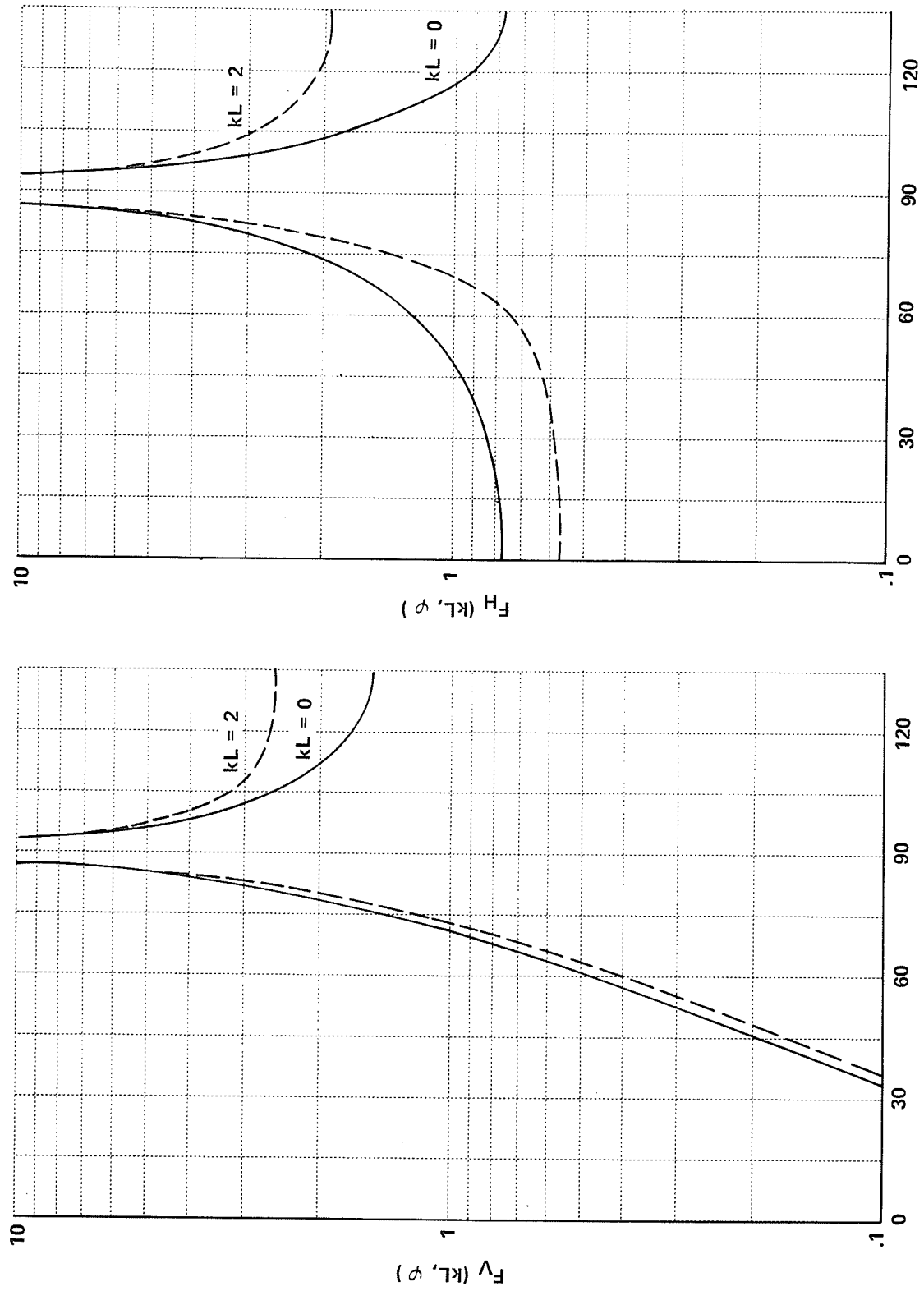

Figure 6.6 SCATTERING DATA FOR 90° TRUNCATED WEDGE

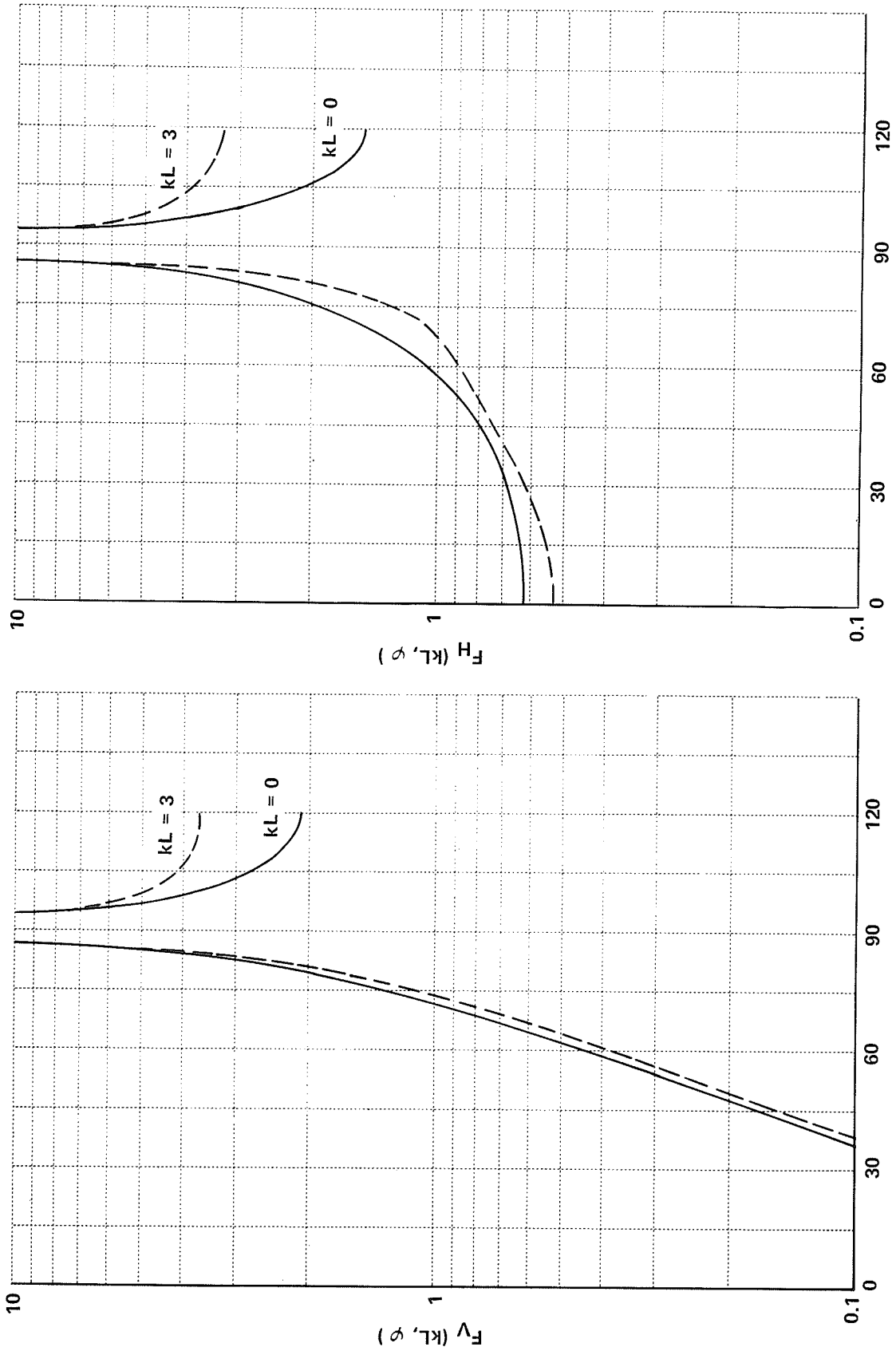

Figure 6.7 SCATTERING DATA FOR 120° TRUNCATED WEDGE

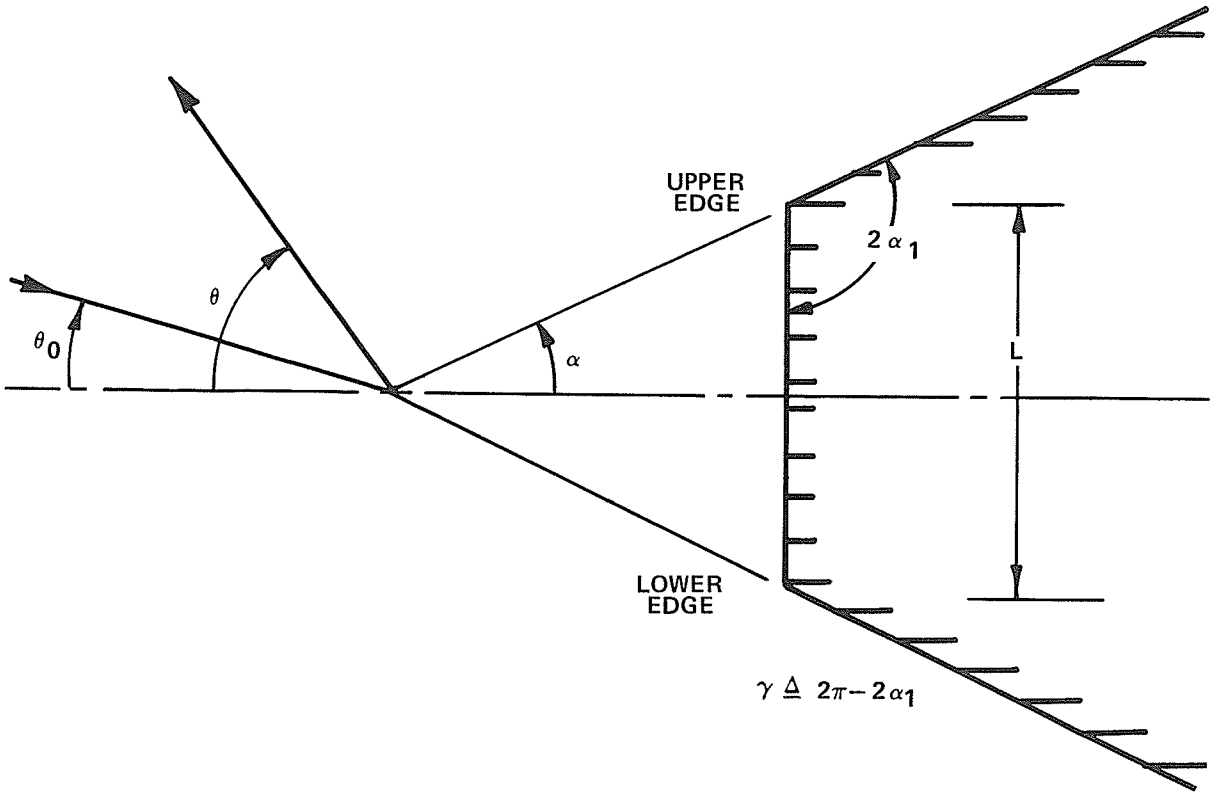

Figure 6.8 SCHEMATIC DIAGRAM OF TRUNCATED WEDGE

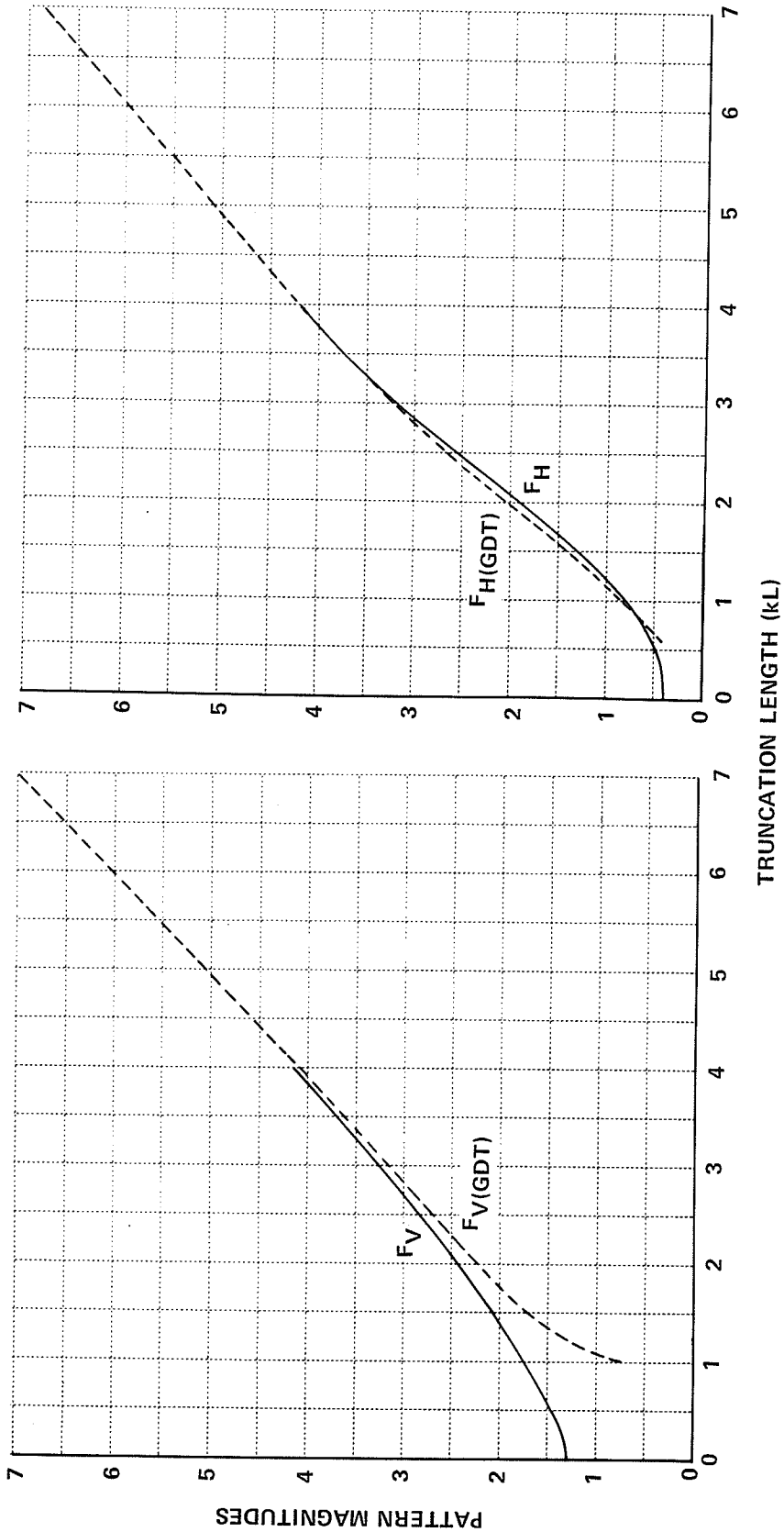

Figure 6.9 SYMMETRICAL INCIDENCE BACKSCATTERING FROM A 60° TRUNCATED WEDGE

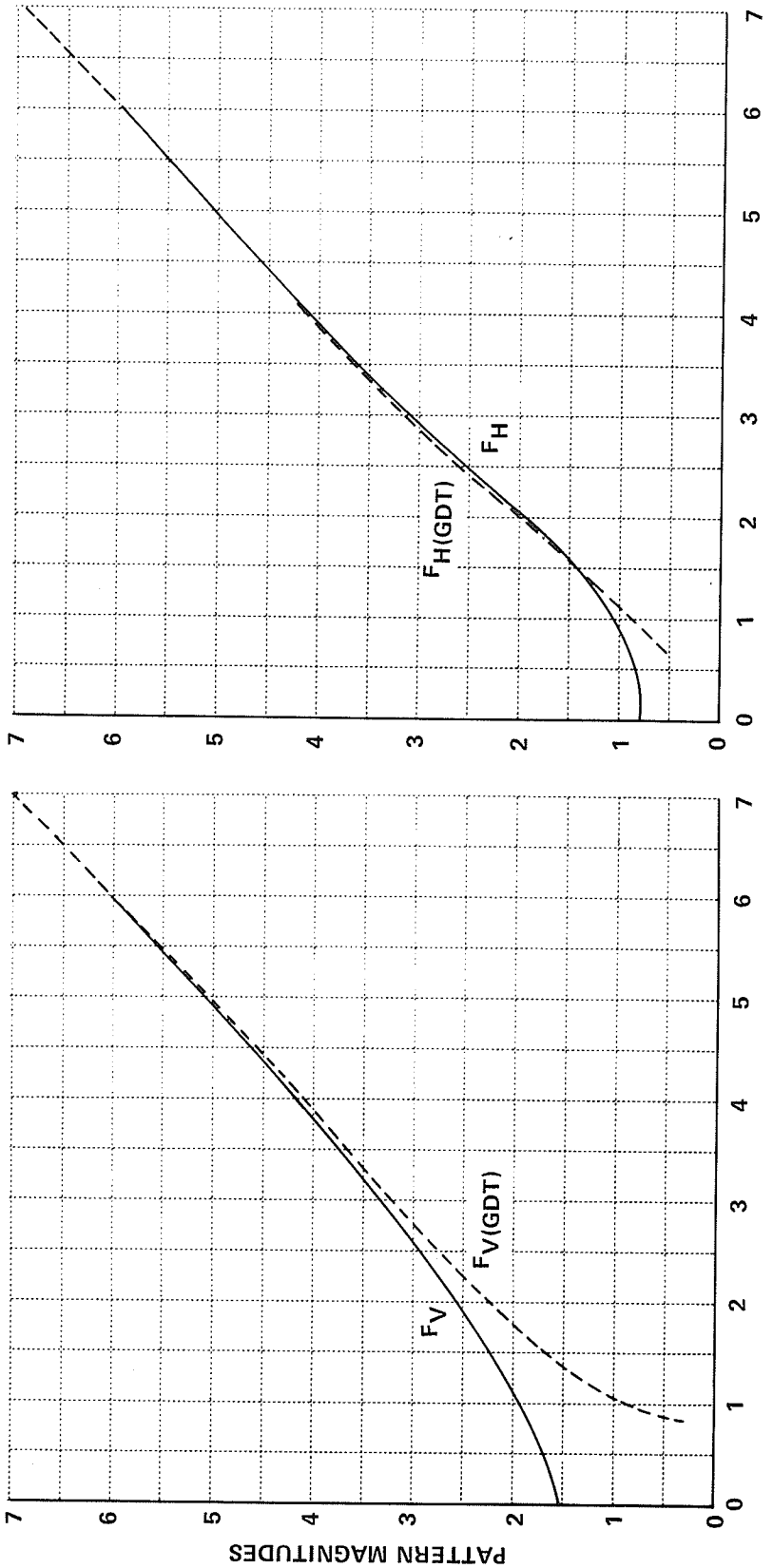

Figure 6.10 SYMMETRICAL INCIDENCE BACKSCATTERING FROM A 90° TRUNCATED WEDGE

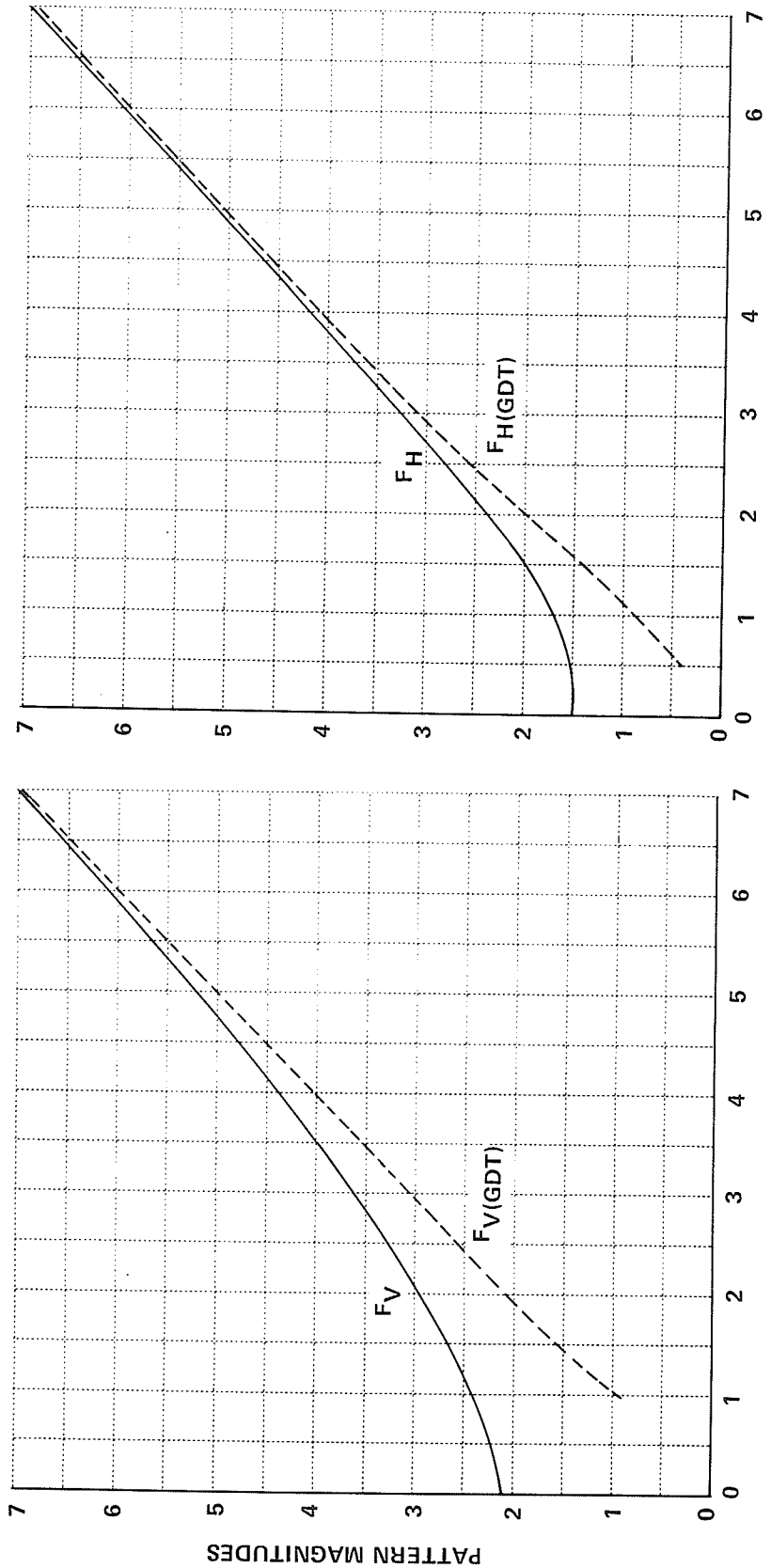

Figure 6.11 SYMMETRICAL INCIDENCE BACKSCATTERING FROM A 120° TRUNCATED WEDGE

7. CONCLUSIONS AND RECOMMENDATIONS

Previous results attest the validity of the scattering center concept for predicting high-frequency electromagnetic scattering by simple, conducting, generic shapes. It is necessary to investigate additional scattering centers in order to treat radar targets of more practical interest, and the geometrical discontinuity formed by a rounded edge was selected for detailed examination.

A solution to the problem of plane wave scattering by a semi-infinite, perfectly conducting wedge with rounded edge has been obtained by the boundary value approach. Checks on calculations provide a demonstration of internal consistency as well as agreement with independent scattering data computed from an integral equation formulation. It has been shown that ka less than unity can double the sharp wedge result, although the effect of rounding is markedly dependent upon aspect angle, polarization and wedge angle. Qualitatively, the change in the sharp wedge result is directly proportional to ka and inversely proportional to wedge angle 2α. Monostatic calculations show that, independent of polarization and wedge angle, increase in rounding causes a decrease in scattering at aspect less than the specular value followed by an increase in scattering at aspects greater than the specular value. Bistatic calculations reveal that more energy is coupled into the shadow region by diffraction at a sharp wedge than by creeping waves on a rounded wedge. More importantly, the boundary value solution for the rounded wedge provides quantitative results which enable us to extend scattering center theory. The numerical capability of the boundary value solution extends over intermediate values of wedge angle with a substantial upper limit on rounding; aspect

dependent calculations allow maximum rounding ka = 4, while symmetrical incidence capability includes ka as large as 7. Following investigation of scattering by a cylindrically-tipped wedge we conclude that greater rounding may be treated by an integral equation solution since the matching boundary collapses to the virtual edge of the sharp wedge.

Provided that incidence is symmetric on a wedge with appreciable rounding, the scattering is insensitive to polarization. Then asymptotic physical optics accurately predicts expressions for the reradiation from scattering centers on the obstacle. In this manner we discover the limiting behavior of the contribution arising at the join scattering center. Modification of asymptotic physical optics to include a polarization-dependent specular return does not improve overall prediction capability. Unfortunately, the observed limitations upon physical optics (large rounding unless wedge angle is narrow and polarization is horizontal; symmetrical incidence only) preclude a general application.

For moderate rounding ($ka \leq 1$), advantages accrue from viewing the boundary value solution as the sharp-wedge result plus a perturbation field. In particular, the monostatic and symmetrical-incidence bistatic aspect dependence of principal-polarization perturbation fields (magnitude and phase) are accurately described by compact expansions. The coefficients of these expansions are tabulated at steps of 0.2 in ka and 10° in wedge angle. However, the observed dependence of these coefficients upon ka and α is complicated, so that considerable additional analysis is required to determine the complete parametric dependence of perturbation data. For this reason, alternate methods which can lead to approximations to the join return should be sought.

The quantitative perturbation data tabulated in this thesis provide a convenient means of extending scattering center theory to include targets with one or more rounded edges separated by at least three wavelengths. Investigation of reradiation by a modified equilateral triangular prism, a modified square prism and a modified finite, right-circular cylinder shows that, for a given rounding, the scattering is most sensitive to target shape; the narrower the wedge angle associated with target scattering centers, the greater the effect of rounding. Finally, the choice of polarization determines the relative strength of pattern peaks at intermediate aspects: for vertical polarization, rounding increases the magnitude of peaks; for horizontal polarization, peak values are reduced by rounding.

Calculations of scattering by a truncated wedge have been performed to illustrate the generality of the boundary value approach. These data have been used to evaluate the geometrical-diffraction-theory model for interactions between closely spaced scattering centers. For symmetrical incidence backscattering, approximate theory is accurate for a truncation length kL as small as 0.5, provided polarization is horizontal and the wedge angle is 60°. Because Hunter has obtained correspondence for kL as low as 0.3, further work on interactions between scattering centers should be performed within the context of his modification to geometrical diffraction theory.

Appendix A
ASYMPTOTIC PHYSICAL OPTICS APPLIED TO WEDGE WITH ROUNDED EDGE

Chapter 3 introduced an asymptotic form of physical optics. Following presentation of general formulas, this approximate theory was specialized to predict scattering by a wedge with rounded edge. The relations (3.13), (3.15) and (3.16) employed in that chapter are derived in this appendix. First the general formula involving a singularity at one end of the interval of integration is used to evaluate the specular transfer function $g(k)_s$. Next we determine the join transfer functions $g(k)_1$ and $g(k)_2$. Finally, limitations on the aspect-dependent asymptotic result are discussed.

Specular Transfer Function $g(k)_s$

Fig. A.1 depicts a wedge with rounded edge illuminated monostatically at an angle θ which is less than the wedge half-angle α. The electrical radius of curvature of the tip (ka) is assumed large enough that physical optics applies.

Specular scattering arising from the cylindrical surface is described by the transfer function $g(k)_s$ evaluated by local application of (3-3). Recall that y is the coordinate along the line-of-sight, and L is the chord of intercept of the target with the plane perpendicular to the line-of-sight. Refering to Fig. A.1, choose $y = 0$ at the virtual apex of the wedge. Denote the shortest (line-of-sight) distance to the cylindrical sector by y_o, and the join distances by y_1 and y_2. Applying (3-3) to the cylindrical sector, we have

$$g(k)_s = k e^{-j\frac{3\pi}{4}} I_s \qquad (A.1)$$

where

$$I_s = \int_{z_0}^{z_1} \frac{dL_1}{dz}\, dz\, e^{-j2kz} + \int_{z}^{z_2} \frac{dL_2}{dz}\, dz\, e^{-j2kz} = I_{s_1} + I_{s_2} \tag{A.2}$$

and

$$\begin{aligned} L &= L_1 + L_2 \\ z_0 &= a\left(\frac{\cos\theta}{\sin\alpha} - 1\right) \\ z_1 &= a\left(\frac{\cos\theta}{\sin\alpha} - \sin(\alpha+\theta)\right) \\ z_2 &= a\left(\frac{\cos\theta}{\sin\alpha} - \sin(\alpha-\theta)\right) \end{aligned} \tag{A.3}$$

To evaluate $g(k)_s$ we examine the first integral, I_{s_1}, in equation (A.2). For points on the cylindrical sector the following transformation is valid

$$z - z_0 = a(1 - \cos\xi) \tag{A.4}$$

with

$$L_1 = a \sin\xi \tag{A.5}$$

and thus

$$\frac{dL_1}{dz}\, dz = a \cos\xi\, d\xi \tag{A.6}$$

Hence, I_{s_1}, can be written in the form

$$I_{s_1} = a e^{-j2ka\frac{\cos\theta}{\sin\alpha}} \int_0^{a[1-\sin(\alpha+\theta)]} \cos\xi\; e^{+j2ka\cos\xi}\, d\xi \tag{A.7}$$

Comparing the integral in (A.7) with the form for the Fourier integral employed in Chapter 3, section 3.3, i.e.,

$$\int_{t_1}^{t_2} e^{+j x t} \, \Phi(t) \, dt$$

we see that

$$\begin{aligned} x &= 2ka \\ t &= \cos\xi \\ \Phi(t) &= -\frac{t}{\sqrt{1-t}\,\sqrt{1+t}} \\ t_1 &= 1 \\ t_2 &= \cos\left[a\left(1-\sin(\alpha+\theta)\right)\right] \end{aligned} \tag{A.8}$$

Notice that a singularity occurs in $\Phi(t)$ at the lower limit. Therefore (3-10) applies in the evaluation of I_{s_1} with $\nu = 1/2$ and $\Phi(t) = \frac{jt}{\sqrt{1+t}}$ in (3-11), i.e.,

$$\begin{aligned} I_{s_1} &= A_N \\ &= -\sum_{n=0}^{N-1} \frac{\Gamma(n+\frac{1}{2})}{n!} e^{j\frac{\pi}{2}(n-\frac{3}{2})} \Phi^{(n)}(1)(2ka)^{-n-\frac{1}{2}} e^{j2ka} \end{aligned} \tag{A.9}$$

Evaluating the first two terms in this asymptotic series we have

$$A_1 = -\sqrt{\frac{\pi}{4ka}}\, e^{-j\left(\frac{\pi}{4}-2ka\right)} \tag{A.10}$$

$$A_2 = A_1 - \frac{3\sqrt{\pi}}{32}(ka)^{-3/2} e^{\left(j\frac{\pi}{4}+2ka\right)} \tag{A.11}$$

Substitution of (A.10) and (A.11) into (A.7) provides the solution for I_{s_1}. Because the solution is independent of the upper limit on the integral, $I_{s_1} = I_{s_2}$ and the specular transfer function is given by

$$g(k)_s = \sqrt{\pi ka}\left\{1 + \frac{j}{2ka}\left[\frac{3}{8}\right] \cdots\right\} e^{j2ka\left(1-\frac{\cos\theta}{\sin\alpha}\right)} \tag{A.12}$$

$$0 \leq \theta < \alpha$$

Finally, the leading term A_1 corresponds to stationary phase evaluation of I_{s_1}. Thus the formalism employed above is only justified when the second and higher order terms in the asymptotic series are of interest.

Join Transfer Functions $g(k)_1$ and $g(k)_2$

Consider the physical optics estimate of the transfer function associated with the join scattering center S_{j1} depicted in Fig. A.2. Again, z_1 is the line-of-sight separation between the virtual apex of the wedge and the near join, so that (3-3) gives

$$g(k)_1 = k e^{-j\frac{3\pi}{4}} I_{j1} \tag{A.13}$$

$$I_{j1} = \int_{-\infty}^{z_1} e^{-j2kz} \frac{dL}{dz} dz \tag{A.14}$$

To obtain $\frac{dL}{dz}$, notice that Fig. A.2 shows

$$L = L_3 - L_4 \tag{A.15}$$

where L_3 is measured on the extension of the wedge surface, i.e.,

$$L_3 = (-z - z_1) \tan(\theta + \alpha) \tag{A.16}$$

and where L_4 is obtained from the equation of the cylindrical surface when referenced to the origin at S_{j1}, i.e.,

$$L_4 = a\cos(\alpha+\theta) + \sqrt{a^2 - \left[(z - z_1) - a\sin(\alpha+\theta)\right]^2} \tag{A.17}$$

Collecting (A.16) and (A.17) in (A.15) we obtain

$$\frac{dL}{dz} = -\tan(\alpha+\theta) - \frac{\left[(z-z_1)-a\sin(\alpha+\theta)\right]}{\sqrt{a^2-\left[(z-z_1)-a\sin(\alpha+\theta)\right]^2}} \tag{A.18}$$

Substitution of (A.18) into (A.14) leads to the evaluation of the join transfer function $g(k)_1$ defined in (A.13).

Converting to the notation of asymptotic physical optics, $\Phi(z)$ equals $\frac{dL}{dz}$ and B_N equals I_{j1}, which, from (3.7), is given by

$$B_N = \sum_{n=0}^{N-1} j^{n-1}\, \Phi^{(n)}(z_1)(-2k)^{-n-1}\, e^{j2kz_1} \tag{A.19}$$

The first three terms in the series $\Phi^{(n)}$ are obtained from (A.18)

$$\begin{aligned}
\Phi^{(0)}(z_1) &= 0 \\
\Phi^{(1)}(z_1) &= -\frac{1}{4k^2 a\cos^3(\alpha+\theta)}\, e^{-j2kz_1} \\
\Phi^{(2)}(z_1) &= -\frac{3j\sin(\alpha+\theta)}{8k^3a^2\cos^5(\alpha+\theta)}\, e^{-j2kz_1}
\end{aligned} \tag{A.20}$$

where $\Phi^{(0)}(z_1)=0$ follows from the continuity of the normal at the join. Collecting results, the first two nonzero terms in the asymptotic expansion of the join transfer function become

$$g(k)_1 = \left\{\frac{1}{2} + \frac{3j\sin(\alpha+\theta)\cos(\alpha+\theta)}{4ka\cos^3(\alpha+\theta)} \quad \cdots\right\} \frac{e^{-j\left[\frac{3\pi}{4}+2ka\left(\frac{\cos\theta}{\sin\alpha}-\sin(\alpha+\theta)\right)\right]}}{2ka\cos^3(\alpha+\theta)} \tag{A.21}$$

$$-\alpha \le \theta \le \pi-\alpha$$

$$= 0\,, \qquad \theta < -\alpha$$

which is (3-15). From the symmetry of the problem, the other join return $g(k)_2$ given by (3.16) is obtained from (A.21) by changing the sign of θ.

Aspect Limitations

In the derivation of the specular transfer function $g(k)_s$, the aspect restriction $\theta < \alpha$ was introduced. Then the first Fresnel zone of specular scattering excludes the join and the asymptotic evaluation of integrals I_{s_1} and I_{s_2} (which is insensitive to the upper limits) is valid for large ka. As aspect increases to the value $\theta = \frac{\pi}{2} - \alpha$, $I_{s_1} \longrightarrow 0$ and the specular return given by (A.12) is reduced by a factor of two. Further increase in aspect angle results in zero specular contribution. For these reasons, the asymptotic evaluation of the specular return from the cylindrical sector is appropriate at and near the symmetrical incidence aspect ($\theta \approx 0$).

The aspect limitation on the join transfer functions $g(k)_1$ and $g(k)_2$ is more serious. This situation arises from the aspect dependent form of terms in the asymptotic expansion; for example, succeeding terms in the expansion for the near join contain higher order singularities when $\theta \longrightarrow \frac{\pi}{2} - \alpha$. Thus the series is nonconvergent for normal incidence and calculations based upon asymptotic theory are invalid. Attempts to find a closed form representation of the series were unsuccessful. Therefore the two term expansion given by (A.21) has utility when θ is sufficiently removed from the normal aspect.

Because of the aspect limitations noted above, our derivation of aspect-dependent formulas based upon asymptotic physical optics is useful only for incidence at or near the symmetrical aspect.

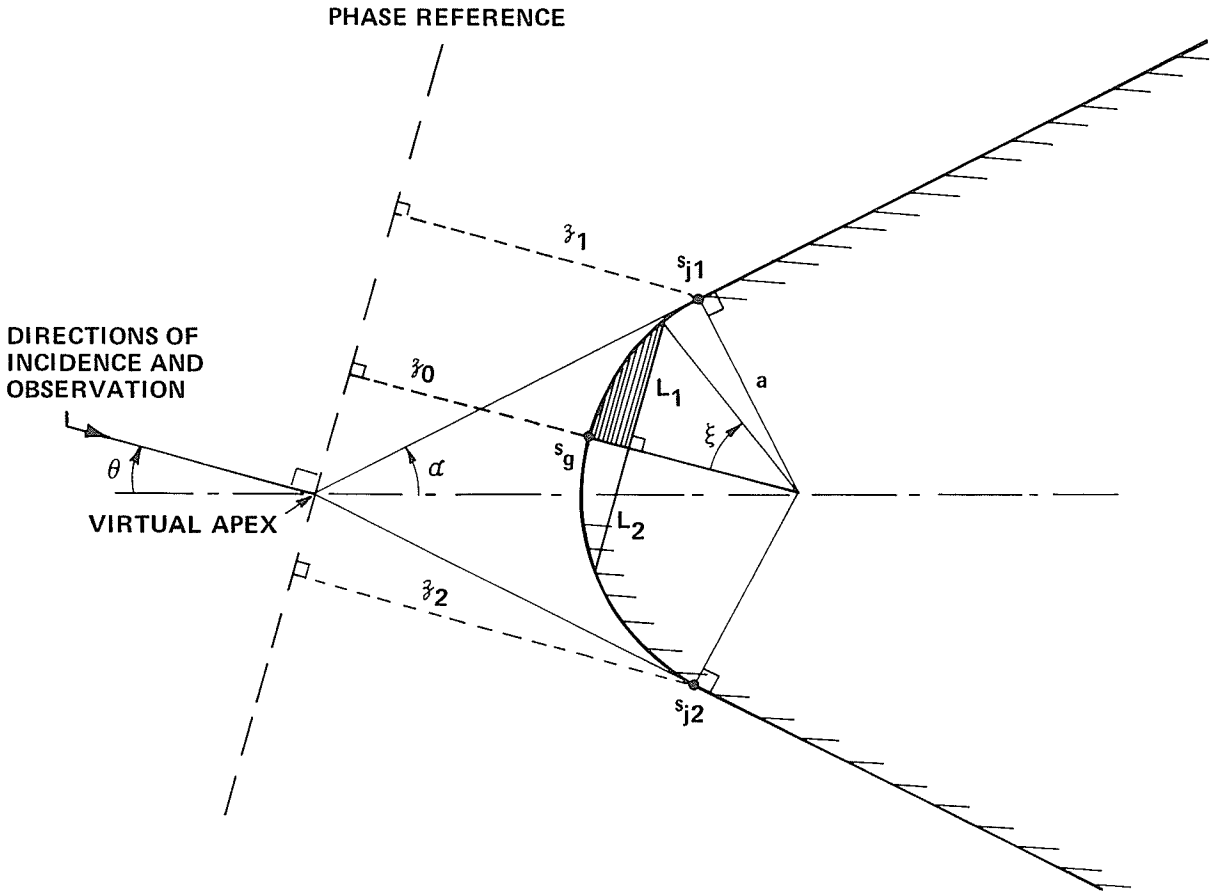

Figure A.1 PARAMETERS USED TO EVALUATE SPECULAR TRANSFER FUNCTION $g(k)_s$

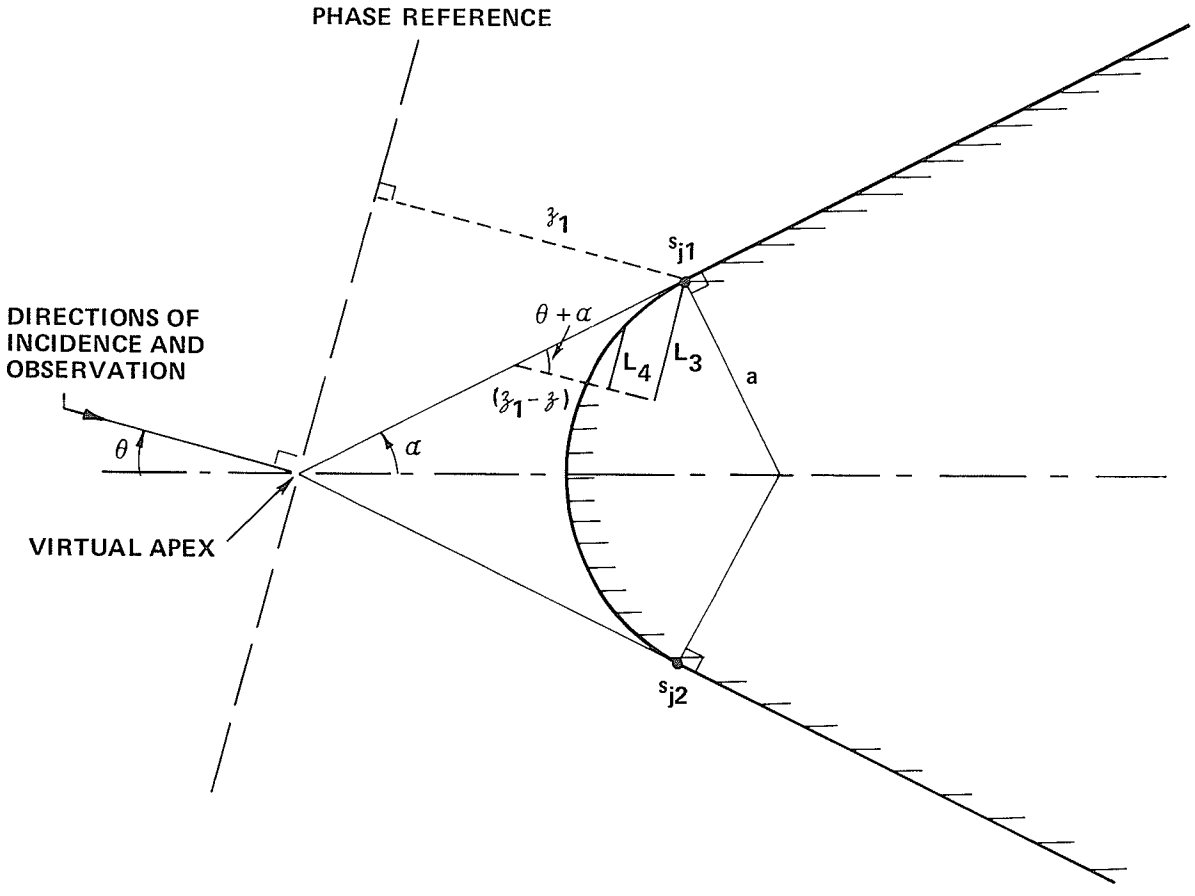

Figure A.2 PARAMETERS USED TO EVALUATE JOIN TRANSFER FUNCTION $g(k)_1$

Appendix B
INTEGRAL EQUATION FORMULATION

A solution of electromagnetic fields in the presence of conducting cylinders of arbitrary cross section, illuminated normally by a plane wave polarized parallel to the axis of the cylinder, may be obtained by an application of Green's identity in the form[68]

$$E_z = E_z^i - 30\pi k \int_c H_0^{(2)}\left(k\,|\vec{r}-\vec{r}'|\right) K_z(\vec{r}')\, dc' \qquad \text{(B.1)}$$

where K_z is the induced current on the surface of the cylinder and the integration is along the contour c of its cross section. Application of the boundary condition on the surface of the conductor reduces (B.1) to

$$E_z^i(\vec{r}_o) = 30\pi k \int_c H_0^{(2)}\left(k\,|\vec{r}_o-\vec{r}'|\right) K_z(\vec{r}')\, dc' \qquad \text{(B.2)}$$

where $\vec{r}_o$ is a position vector associated with a field point on the scatterer. In (B.2), K_z is usually obtained numerically by moment methods.[68] However, for vertical polarization, the induced current is singular at a sharp edge, and the accurate determination of K_z requires treatment of these singularities. One approach involves conformal transformation of the (edgy) surface onto a circular cylinder.[69] Then (B.2) becomes

$$E_z^i(\vec{r}_o) = 30\pi k \int_0^{2\pi} H_0^{(2)}\left(k\,|\vec{r}_o-\vec{r}'|\right) I_z(\phi')\, d\phi' \qquad \text{(B.3)}$$

where $I_z = h K_z$ is now a regular function and h is the metric of the transformed coordinate ϕ with respect to the original x-y coordinates. For the regular, equilateral triangular prism shown in Fig. 5.1(a) the coordinate relations are given by

$$x = 0.59L\left[\cos\phi - \frac{1}{3}\cos(2\phi) + \frac{1}{45}\cos(5\phi)\ldots\right]$$

$$y = 0.59L\left[\sin\phi + \frac{1}{3}\sin(2\phi) - \frac{1}{45}\sin(5\phi)\ldots\right] \qquad \text{(B.4)}$$

while the metric coefficient h is given by

$$h = 0.59\left|\cos(1.5\phi)\right|^{2/3} \qquad \text{(B.5)}$$

Since the transformed current I_z is a regular function of ϕ, it may be expressed in the form

$$I_z(\phi) = \sum_{n=1}^{N}\left[A_n\cos(n-1)\phi + B_n\sin n\phi\right] \qquad \text{(B.6)}$$

Using (B.4) through (B.6) the integral equation (B.3) can be evaluated numerically by selecting N field points on the surface of the prism. Finally, the expansion for the scattering pattern $F_{v(IEF)}$ is obtained from (B.1) viz.,

$$F_{v(IEF)} = 60\pi k\left|\int_0^{2\pi}\left[\sum_{n=1}^{N}\left(A_n\cos(n-1)\phi' + B_n\sin n\phi\right)\right]\times e^{jkr'\cos(\phi-\phi')}\,d\phi'\right| \qquad \text{(B.7)}$$

A conformal transformation of the modified prism shown in Fig. 5.1(b) is not known. Here (B.2) and (B.3) are combined in form

$$E_z'(\vec{r}_o) = 30\pi k \left\{ \int_{\mathcal{C}_1} H_o^{(2)}\left(k\,|\vec{r}_o - \vec{r}'|\right) K_z \, d\ell_1' \right.$$

$$\left. + \int_{\phi_1}^{\phi_2} H_o^{(2)}\left(k\,|\vec{r}_o - \vec{r}'|\right) I_z \, d\phi' \right\} \qquad \text{(B.8)}$$

where $\mathcal{C}_1$ is the circular cylindrical sector and $\mathcal{C}_2$ the remaining contour. Note that K_z can be found accurately by direct application of moment methods, since the surface current is regular on $\mathcal{C}_1$. The magnitude of the scattering pattern then becomes,

$$F_{V(IEF)} = 60\pi k \left| \sum_{m=1}^{M} D_m K_{z_m} e^{jk(x_m \cos\phi + y_m \sin\phi)} \right.$$

$$\left. + \int_{\phi_1}^{\phi_2} \left[\sum_{n=1}^{N} \left(A_n \cos(n-1)\phi' + B_n \sin n\phi' \right) \right] e^{jkr'\cos(\phi - \phi')} \, d\phi \right| \qquad \text{(B.9)}$$

Equations (B.7) and (B.9) were programmed for an IBM 360/65 digital computer to generate the accurate monostatic and bistatic scattering data presented in Tables 5.1 and 5.2.

REFERENCES

1. Logan, N.A., "Summary of Some Early Studies of the Scattering of Plane Waves by a Sphere," Proc. IEEE, 53, 1965, pp. 773-785.

2. Bouwkamp, C.J., "Diffraction Theory," Reports on Progress in Physics, XVII, 1954, pp. 35-100.

3. Corriher, H.A., Jr., and Pyron, B.O., "A Biography of Articles on Radar Reflectivity and Related Subjects: 1957-1964," Proc. IEEE,53, 1965, pp. 1025-1064.

4. Kline, M. and Kay, I.W., Electromagnetic Theory and Geometrical Optics, New York, Interscience, 1965.

5. Keller, J.B., "Geometrical Theory of Diffraction," J. Opt. Soc. Am., 52, 1962, pp. 116-130.

6. Sinclair, G., "Modification of the Radar Range Equation for Arbitrary Targets and Arbitrary Polarization," Ohio State Univ. Res. Found., Report No. 302-19, September 1948.

7. Ross, R.A., "Investigation of Scattering Matrix Measurements and Suspension Target Supports," Cornell Aeronautical Laboratory, Inc., Report No. UB-1806-P-1, January 1964.

8. Alongi, A.V., Kell, R.E., and Newton, D.J., "A High Resolution X-Band FM/CW Radar for RCS Measurements," Proc. IEEE, 53, 1965, pp. 1072-1076.

9. Alongi, A.V., "The Delta Radar System - A Wide Bandwidth FM/CW X-Band Radar for the Fine Range Resolution Measurement of Radar Cross Section," Cornell Aeronautical Laboratory, Inc., Report No. UB-1571-P-1, July 1962.

10. Ross, R.A., "Radar Cross Section of Rectangular Flat Plates," Trans. IEEE, AP-14, 1966, pp. 329-335.

11. Ross, R.A., "Radar Cross Section of Rectangular Flat Plates," MS Thesis, State University of New York at Buffalo, February 1966.

12. Ross, R.A., "Application of Geometrical Diffraction Theory to Reflex Scattering Centers," IEEE International Antennas and Propagation Symposium, September 9-11, 1968, Conference Publication 68 C 29 AP.

13. Ross, R.A., "Small-Angle Scattering by a Finite Cone," IEEE Trans., AP-17, pp. 103-106, 1969.

14. Ross, R.A., Witt, H.R., and Graham, J.R., Jr., "Radar Cross Section of a Finite Rectangular Cylinder," Electronic Letters (London), July 1967, 3, No. 7, pp. 336-337.

15. Ross, R.A., "Scattering by a Finite Cylinder," Proc. IEEE (London), July 1967, pp. 864-868.

16. Ross, R.A., Freeny, C.C., and Cleary, J.C., "Bistatic Scattering Matrix for a Finite Right-Circular Cylinder," Electronics Letters (London), 4, 19 April 1968.

17. Ross, R.A. and Price, E.L., "Radar Cross Section of Finite, Right-Circular Cylinders," Cornell Aeronautical Laboratory, Inc., Report No. ER/RIS-12, October 1966.

18. Ross, R.A., "Bistatic Scattering Matrix for a Frustrum," IEEE Trans., AP-17, 1969, pp. 103-106.

19. Keller, J.B., "Backscattering from a Finite Cone-Comparison of Theory and Experiment," IRE Trans., AP-9, July 1961, pp. 411-412.

20. Bechtel, M.E., "Application of Geometrical Diffraction Theory to Scattering from Cones and Disks," Proc. IEEE, 53, August 1965, pp. 877-882.

21. Bechtel, M.E., "Vertically Polarized Radar Backscattering from the Rear of a Cone or Cylinder," IEEE Trans., AP-17, 1969, pp. 244-246.

22. Yu, J.S. and Rudduck, R.C., "On Higher-Order Diffraction Concepts Applied to a Conducting Strip," IEEE Trans., AP-15, September 1967, pp. 662-668.

23. Yu, J.S., "Radar Cross Section of a Thin Plate Near Grazing Incidence," IEEE Trans., AP-17, September 1970, pp. 711-713.

24. Ryan, C.E., Jr. and Peters, L., Jr., "Evaluation of Edge-Diffracted Fields Including Equivalent Currents for the Caustic Regions," IEEE Trans., AP-17, May 1969, pp. 292-299.

25. Senior, T.B.A. and Uslenghi, P.L.E., "High-Frequency Backscattering from a Finite Cone," Radio Science, 6, March 1971, pp. 393-406.

26. Keller, J.B., "Diffraction by an Aperture I," New York Univ., Res. Report No. EM-92, June 1956.

27. Helstrom, C.W., "Backscattering of Radar Waves," Westinghouse Electric Corp., Res. Report No. 412-F8573-R1, 1960.

28. Ross, R.A., "Investigation of Scattering Center Theory," Air Force Avionics Laboratory Technical Report No. 67-343, December 1967.

29. Ross, R.A., "Investigation of Scattering Principles, Vol. III, Analytical Investigation," General Dynamics Report FZE-793, July 1968.

30. Ryan, E.E., "A Geometrical Theory of Diffraction Analysis of the Radar Cross Section of a Sectionally Continuous Second-Degree Surface of Revolution," Ohio State Univ., Res. Report No. TR-2430, March 1968.

31. Bechtel, M.E., and Ross, R.A., "Radar Scattering Analysis," Cornell Aeronautical Laboratory, Inc., Report No. ER/RIS-10, August 1966

32. Ruck, G.T., Barrick, D.E., Stuart, W.D., and Kirchbaum, C.K., Radar Cross Section Handbook, New York, Plenum Press, 1970.

33. Kell, R.E. and Ross, R.A., "Radar Cross Section of Targets," Chapter 27, Radar Handbook, edited by M.I. Skolnik, McGraw Hill, 1970.

34. Kell, R.E., "On the Derivation of Bistatic RCS from Monostatic Measurements," Proc. IEEE, 53, August 1965.

35. Crispin, J.W., Jr., Goodrich, R.F., and Siegel, K.M., "A Theoretical Method for the Calculation of the Radar Cross Sections of Aircraft and Missiles," University of Michigan Radiation Laboratory, Report No. 2591-1-H, July 1959.

36. Ross, R.A. and Bechtel, M.E., "Scattering-Center Theory and Radar Glint Analysis," Trans. IEEE, AES-4, 5, 1968, pp. 756-762.

37. Kell, R.E. and Ross, R.A., "Direct and Inverse Scattering Relations for Bistatic Radar Targets," Proc. of First GISAT Symposium, Boston, December 1965.

38. Kraus, L., "Diffraction by a Plane Angular Sector," Ph.D. Dissertation, New York University, 1955.

39. Satterwhite, R.S. and Kouyoumjian, R.G., "Electromagnetic Diffraction by a Perfectly Conducting Plane Angular Section," Ohio State Univ., Electro Science Laboratory, Tech. Report No. 2183-2, March 1970.

40. Keller, J.B., Lewis, R.M., and Seckler, B.D., "Diffraction by an Aperture, II," New York University Research Report No. EM-96, August 1956.

41. Felsen, L.B., "Asymptotic Expansion of the Diffracted Wave for a Semi-Infinite Cone," Trans. IRE., AP-5, 1957, pp. 402-404.

42. Siegel, K.M., Crispin, J.W., Jr., and Schensted, C.E., "Electromagnetic and Acoustical Scattering from a Semi-Infinite Cone," J. Appl. Phys., 26, 1955, pp. 309-313.

43. Hong, S. and Weston, V.H., "A Modified Fock Function for the Distribution of Currents in the Penumbra Region with Discontinuity in Curvature," Rad. Sci., 1, September 1966, pp. 1045-1053.

44. Stone, S.E. and Sleator, F.B., "Forward Scattering by Cone-Spherical Bodies," Inter. URSI Symposium Digest, September 1970, p. 57.

45. Weston, V.H., "Effect of a Discontinuity of Curvature in High-Frequency Scattering. Part II," Trans. IEEE, AP-13, 1965, pp. 611-613.

46. Hunter, J.D., "Aspects of Electromagnetic Scattering," Ph.D. Dissertation, University of Canterbury, New Zealand, 1970.

47. Karp, S.N., "Diffraction by a Tipped Wedge with Application to Blunt Edges," New York University, Report No. EM-52, May 1953.

48. Weiner, S.D. and Borison, S.L., "Radar Scattering from Blunted Cone Tips," Trans. IEEE, AP-17, 1966, pp. 774-781.

49. Harrington, R.F., Time-Harmonic Electromagnetic Fields, New York, McGraw Hill, 1961.

50. Watson, G.N., A Treatise on the Theory of Bessel Function, Cambridge, Cambridge University Press, 1966.

51. Abramowitz, M. and Stegun, I.A., Handbook of Mathematical Functions, New York, Dover Publications, 1965.

52. Pauli, W., "On Asymptotic Series for Functions in the Theory of Diffraction of Light," Phys. Rev., 54, 1938, pp. 924-931.

53. Imai, I., "Die Beugung Elektromagnetischer Wellen an Einem Kreiszylinder," Z. Fur Phys., 137, 1954, pp. 31-48.

54. Kouyoumjian, R.G. and Burnside, W.D., "The Diffraction by a Cylinder-Tipped Half-Plane," IEEE Trans., AP-18, May 1970, pp. 424-426.

55. Kouyoumjian, R.G., "Asymptotic High-Frequency Methods," Proc. IEEE., 53, 1965, pp. 864-876.

56. Siegel, K.M. and Alperin, H.A., et al., "Bistatic Radar Cross Sections of Surfaces of Revolution," Jour. Appl. Phys., 26, 1955, pp. 297-305.

57. Olte, A. and Silver S., "New Results in Backscattering from Cones and Spheroids," Trans. IRE, AP-7, 1959, pp. 561-567.

58. Knott, E.F. and Senior, T.B.A., "The Effect of Fins on the Nose-On Cross Section of a Cone-Sphere," Trans. IEEE (C), AP-11, 1963, pp. 504-505.

59. Crispin, J.W., Jr. and Siegel, K.M., (Editors), Methods of Radar Cross-Section Analysis, New York, Academic Press, 1968.

60. Kerr, D., Propagation of Short Radio Waves, 13, MIT Radiation Laboratory Series, McGraw-Hill, 1951.

61. Geller, L., "A Method for Rapidly Calculating Radar Cross-Section at High Frequencies," Cornell Aeronautical Laboratory, Inc., Internal Memorandum, 10 November 1954.

62. Bechtel, M.E., "The Asymptotic Physical Optics Method of Radar Cross-Section Calculation," Cornell Aeronautical Laboratory, Inc., Internal Memorandum, 30 November 1961.

63. Erdelyi, A., Asymptotic Expansions, Dover, 1956, pp. 46-48.

64. Ross, R.A., "Modification of Geometrical Diffraction Theory for Specular Scattering," Inter. IEEE/G-AP Symposium Digest, October 1967.

65. Stratton, J.A., Electromagnetic Theory, New York, McGraw-Hill, 1941, pp. 413-414.

66. Mohsen, A. and Hamid, M.A.K., "Higher Order Asymptotic Terms of the Two-Dimensional Diffraction by a Small Aperture," Radio Science, 3, November 1968, pp. 1105-1108.

67. Karp, S.N. and Keller, J.B., "Multiple Diffraction by an Aperture in a Hard Screen," New York University Research Report No. EM-143, November 1959.

68. Harrington, R.F., Field Computation by Moment Methods, New York, MacMillan, 1968.

69. Shafai, L., "An Improved Integral Equation for the Numerical Solution of Two-Dimensional Diffraction Problems," Can. J. Phys., 48, 1970, pp. 954-963.